The Astrophysical Journal, 951:105 (33pp), 2023 July 10 https://doi.org/10.3847/1538-4357/accbbf

Extending the Dynamic Range of Galaxy Outflow Scaling Relations: Massive Compact Galaxies with Extreme Outflows

Julie D. Davis[1], Christy A. Tremonti[1], Cameren N. Swiggum[1,2], John Moustakas[3], Aleksandar M. Diamond-Stanic[4], Alison L. Coil[5], James E. Geach[6], Ryan C. Hickox[7], Serena Perrotta[5], Grayson C. Petter[7], Gregory H. Rudnick[8], David S. N. Rupke[9], Paul H. Sell[10], and Kelly E. Whalen[7]

[1] University of Wisconsin-Madison, 475 N. Charter St. Madison, WI 53706, USA; jdavis@astro.wisc.edu
[2] Department of Astrophysics, University of Vienna, Trkenschanzstrasse 17, A-1180 Wien, Austria
[3] Department of Physics and Astronomy, Siena College, Loudonville, NY 12211, USA
[4] Department of Physics and Astronomy, Bates College, Lewiston, ME 04240, USA
[5] Department of Astronomy, University of California, San Diego, CA 92092, USA
[6] Centre for Astrophysics Research, University of Hertfordshire, Hatfield, Hertfordshire AL10 9AB, UK
[7] Department of Physics and Astronomy, Dartmouth College, Hanover, NH 03755, USA
[8] Department of Physics and Astronomy, University of Kansas, Lawrence, KS 66045, USA
[9] Department of Physics, Rhodes College, Memphis, TN 38112, USA
[10] Department of Astronomy, University of Florida, Gainesville, FL 32611 USA

Received 2022 July 29; revised 2023 March 30; accepted 2023 April 9; published 2023 July 6

Abstract

We investigate galactic winds in the HizEA galaxies, a collection of 46 late-stage galaxy mergers at $z = 0.4$–0.8, with stellar masses of $\log(M_*/M_\odot) = 10.4$–11.5, star formation rates (SFRs) of 20–500 $M_\odot$ yr^{-1}, and ultra-compact (a few 100 pc) central star-forming regions. We measure their gas kinematics using the Mg II $\lambda\lambda$ 2796,2803 absorption lines in optical spectra from MMT, Magellan, and Keck. We find evidence of outflows in 90% of targets, with maximum outflow velocities of 550–3200 km s^{-1}. We combine these data with ten samples from the literature to construct scaling relations for outflow velocity versus SFR, star formation surface density ($\Sigma_{\rm SFR}$), M_*, and SFR/M_*. The HizEA galaxies extend the dynamic range of the scaling relations by a factor of ~2–4 in outflow velocity and an order of magnitude in SFR and $\Sigma_{\rm SFR}$. The ensemble scaling relations exhibit strong correlations between outflow velocity, SFR, SFR/R, and $\Sigma_{\rm SFR}$, and weaker correlations with M_* and SFR/M_*. The HizEA galaxies are mild outliers on the SFR and M_* scaling relations, but they connect smoothly with more typical star-forming galaxies on plots of outflow velocity versus SFR/R and $\Sigma_{\rm SFR}$. These results provide further evidence that the HizEA galaxies' exceptional outflow velocities are a consequence of their extreme star formation conditions rather than hidden black hole activity, and they strengthen previous claims that $\Sigma_{\rm SFR}$ is one of the most important properties governing the velocities of galactic winds.

Unified Astronomy Thesaurus concepts: Compact galaxies (285); Galaxy evolution (594); Starburst galaxies (1570); Scaling relations (2031)

1. Introduction

Measurements of the cosmic baryon density (e.g., Hinshaw et al. 2013; Planck Collaboration et al. 2016; Cooke et al. 2018) and the galaxy stellar mass function (e.g., Bell et al. 2003; Moster et al. 2010; Moustakas et al. 2013) have shown that only ~4% of baryonic matter is contained in stars at the present time. This surprisingly small fraction of the total baryonic content of the universe implies a cosmic inefficiency of star formation, seen across a wide range of both galaxy and dark matter halo masses. To explain this inefficiency, it is now thought that feedback processes are crucial, injecting energy and momentum into interstellar and circumgalactic gas that would otherwise cool and collapse to form stars (e.g., Somerville & Davé 2015). Observations now support this hypothesis, with large-scale outflows seen in star-forming galaxies and from active galactic nuclei (AGNs). These outflows likely drive the acceleration, heating, and eventual removal of a galaxy's cold gas reservoir, regulating or even halting star formation (e.g., Veilleux et al. 2005; Fabian 2012; Veilleux et al. 2020).

Virtually all modern day galaxy evolution simulations incorporate star formation feedback. However, no simulations include all the relevant physical processes and resolve the scales necessary to properly model the generation of a galactic wind. Because of this, most numerical simulations utilize a subgrid prescription to model feedback and generate galactic winds (for detailed review, see Naab & Ostriker 2017). These subgrid prescriptions are tuned to reproduce key galaxy observables such as the stellar mass function, the stellar mass–halo mass relation, or the mass–metallicity relation. However, these observables are also sensitive to a myriad of other processes, such as the star formation efficiency (see Agertz & Kravtsov 2015). A much more direct way to test the various feedback prescriptions implemented in simulations is to compare simulated galactic winds with those measured observationally. This important work is beginning to be undertaken (see Nelson et al. 2019), but is limited by the inhomogeneous nature of the observations and by their limited dynamic range in galaxy properties.

Most outflow observations are carried out using resonance lines, viewing outflowing material in absorption against continuum emission from the starburst (e.g., Veilleux et al.

2005; Heckman & Thompson 2017). With proper viewing geometry, absorption lines are a powerful tool for characterizing the kinematics in the outflow and allowing for a controlled comparison of the different phases of the wind. Calculating properties such as the outflow rates of mass, momentum, and kinetic energy is more complicated. These quantities require accurate ionic column densities, ionization correction factors, metallicities, and assumptions about the wind's global covering factor and radial distribution (see Rupke et al. 2005). For this reason, we focus primarily on galactic wind outflow velocities and their scaling relations with galaxy properties in the present work.

Numerous authors have studied scaling relations, investigating how the main properties of outflows scale with the basic properties of the launching starbursts and their galaxy hosts (Heckman et al. 2000; Martin 2005; Rupke et al. 2005; Weiner et al. 2009; Chen et al. 2010; Erb et al. 2012; Kornei et al. 2012; Martin et al. 2012; Bordoloi et al. 2014; Rubin et al. 2014; Chisholm et al. 2015, 2016; Heckman et al. 2015; Cicone et al. 2016; Heckman & Borthakur 2016; Prusinski et al. 2021; Xu et al. 2022, excluding AGN-focused studies). These studies have significant variation in target redshifts, galaxy properties, and ionization energies of the selected ionic species. (See Rupke 2018 for a recent review.) Correlations have been found between outflow velocity and stellar mass (M_*), star formation rate (SFR), specific star formation rate (sSFR: SFR/M_*), or SFR surface density ($\Sigma_{\rm SFR}$). However, at present it is not clear which trend is the most fundamental. Small samples and significant scatter in the correlations make it such that trends between outflow velocity and galaxy properties are not always readily apparent when galaxies from an individual survey are considered on their own (e.g., Kornei et al. 2012; Rubin et al. 2014).

One persistent observational limitation in studying the relation between outflows and their host galaxy properties is the fact that there is a relatively limited range in galaxy SFR at fixed stellar mass in the low-redshift universe (e.g., Brinchmann et al. 2004). At higher redshift, there is somewhat more dispersion, but targeted surveys tend to sample relatively small cosmic volumes and thus miss galaxies at the extremes of parameter space (e.g., very high or low SFRs and M_*). This problem is particularly acute for massive galaxies, which are rare by number but account for ∼50% of the stars in the local universe (Hogg et al. 2002).

Massive galaxies ($\log M_* > 10.8$), in which feedback is less understood, have changed over cosmic time. In the local universe, massive galaxies are generally passive and quite large spatially, but at $z > 1.5$, more than half of massive, passive galaxies are compact (Daddi et al. 2005; Zirm et al. 2007; van Dokkum et al. 2008; van der Wel et al. 2014). These compact massive galaxies are thought to have arisen through either highly dissipative mergers of gas-rich disks, which subsequently quenched rapidly (e.g., Barnes & Hernquist 1996; Bournaud et al. 2011), or so-called "compaction" in which early gas disks become violently unstable (Dekel & Burkert 2014). It is unclear, however, whether the strong feedback required to quench these galaxies arises from stellar or AGN processes. The high redshift and frequent dust obscuration of compact galaxies (Stefanon et al. 2013; van Dokkum et al. 2015; Barro et al. 2014) makes direct observations of outflows difficult.

At intermediate redshift ($z = 0.3$–1), compact massive starburst galaxies are rare, but we have leveraged the immense statistical power of the Sloan Digital Sky Survey (SDSS; York et al. 2000) to select a sample of 46 galaxies for detailed study. We refer to these galaxies as the HizEA[11] sample hereafter. Among the HizEA sample are some of the most extreme starburst galaxies with the fastest outflows (>1000 km s^{-1}) and highest SFR surface densities (∼1000 $M_\odot$ yr^{-1} kpc^{-2}) yet seen.

Tremonti et al. (2007) initially identified 14 HizEA galaxies on the basis of their SDSS spectra and demonstrated that they have extraordinary gas outflow velocities ($v_{\rm out} \sim 500$–2000 km s^{-1}) using their Mg II 2796,2804 interstellar medium (ISM) absorption lines. In a number of subsequent works, we have expanded the sample and explored the galaxies' multiwavelength properties. Hubble Space Telescope (HST) imaging revealed that the HizEA galaxies have extremely compact cores and tidal features indicative of late-stage mergers, suggesting that they arise from the dissipative collapse of very gas-rich progenitor merging disks (Sell et al. 2014). These ultra-compact (R_e ∼few 100 pc) galaxies have SFR surface densities comparable to the Eddington limit from radiation pressure on dust grains (Diamond-Stanic et al. 2012, 2021), suggesting that the galaxies represent maximal starbursts (see Meurer et al. 1997; Murray et al. 2005). X-ray, mid-infrared (MIR), radio, and rest-frame optical emission line data (Sell et al. 2014; Petter et al. 2020; Perrotta et al. 2021) indicate that the majority of the HizEA galaxies do not host AGN, and that, when present, AGN likely account for a small fraction (<10%) of the total bolometric luminosity. Therefore, the extreme outflows are likely powered by the compact starbursts. Geach et al. (2013, 2014, 2018) confirm the sample's unique nature with submillimeter observations, discovering nuclear bursts of star formation that are ejecting a large fraction of the cold molecular gas. Keck/HIRES spectra of unsaturated rest-frame near-ultraviolet (NUV) ISM absorption lines in two HizEA galaxies yield mass outflow rates of 600–900 $M_\odot$ yr^{-1} (Perrotta et al. 2023). Integral field spectroscopy of one galaxy (Rupke et al. 2019) shows that the outflowing gas can extend far from the host galaxy, up to ∼50 kpc into the surrounding circumgalactic medium. The extreme nature of these starbursts and outflows represents a likely mechanism for the shut down of star formation through rapid consumption and expulsion of the gas supply.

With the HizEA sample of galaxies, we gain insight into the feedback processes occurring in compact massive starburst galaxies at earlier cosmic times while greatly increasing the dynamic range in M_*, SFR, $\Sigma_{\rm SFR}$, and outflow velocity. Only the work of Heckman & Borthakur (2016) has probed scaling relations for a similar regime, and with our larger sample, we gain a more robust statistical determination of the important trends. The outline of the paper is as follows: In Section 2, we discuss the HizEA sample selection and the properties of our 46 galaxies. In Section 3, we briefly describe the observations and reduction of our optical spectra. In Section 4, we discuss our measurements of stellar masses, SFRs, ages, our method of fitting the Mg II absorption lines, and our outflow velocity measurements. In Section 5, we describe the curation of a comparison sample from outflow data in the literature. In

---

[11] HizEA was originally coined as shorthand for High-z E+A, meaning high-redshift post-starburst. However, subsequent work has shown that many of the galaxies host ongoing starbursts (see Section 2.2).

Section 6, we combine data from the HizEA sample and the literature to investigate outflow scaling relations with M_*, SFR, sSFR, and $\Sigma_{\rm SFR}$. In Section 7, we compare our ensemble scaling relations to four recent theoretical models and discuss the implications of our findings. We summarize and conclude in Section 8. For this work, we adopt a Chabrier initial mass function (IMF; Chabrier 2003) for all stellar masses and SFRs and WMAP9 cosmological values (Hinshaw et al. 2013).

2. The HizEA Sample

The selection of the HizEA galaxies is described fully in C. Tremonti et al. (2023, in preparation). Below we provide a brief overview of our selection criteria (Section 2.1), which were designed to identify young post-starburst galaxies at intermediate redshift. In Section 2.2, we summarize the properties of the sample based on various follow-up studies that we have undertaken, emphasizing the fact that—in spite of our selection criteria—many of the HizEA galaxies host ongoing starbursts that are at or near their peak. We also comment on the incidence of AGN in the sample (Section 2.3). A summary of the sample properties and measurements made in this paper can be found in Table A1.

2.1. Selection Criteria

The initial aim of our work was to study the role of galactic winds in the quenching process in intermediate redshift galaxies. The parent sample was selected from the SDSS-I (York et al. 2000) Data Release 8 (data release, hereafter DR; Aihara et al. 2011). We selected galaxies that were initially targeted for spectroscopy as quasars (Richards et al. 2002) because they probe fainter magnitudes and higher redshifts than the main galaxy sample (Strauss et al. 2002). From the quasar targets, we selected all objects classified by the SDSS spectroscopic pipeline as galaxies (i.e., these objects are contaminants in the quasar targeting algorithm). We limited the study to $z > 0.35$ to ensure that the Mg II λλ2796,2804 ISM line—a widely used probe of galactic winds—was shifted to wavelengths easily accessible to optical spectrographs (>3780 Å). We fit the SDSS spectra with a combination of simple stellar population (SSP) models, similar to Tremonti et al. (2004), but we also include a Type I quasar template. We measure nebular emission lines and several stellar absorption line indices following Kauffmann et al. (2003). We use the emission and absorption lines to select SDSS galaxies with a recent (<1 Gyr) burst of star formation, but little ongoing star formation or AGN activity. We required the following:

1. redshifts of $z = 0.35$–1;
2. $g < 20$ mag or $i < 19$ mag;
3. $f_{\rm qso} < 0.25$, where $f_{\rm qso}$ is the fraction of quasar light at 5000 Å in our stellar population fit;
4. (Lick Hδ_A + Lick Hγ_A)/2 > 3.5 Å or $D_n(4000) < 1.2$;
5. EW [O II] λλ3726, 3729 < 15 Å.

These criteria select galaxies with either strong stellar Balmer absorption (Hγ_A, Hδ_A) or a weak 4000 Å break, indicative of a starburst in the last 1 Gyr, combined with moderately weak nebular emission, indicative of a lower SFR in the past 10 Myr. Our [O II] emission line cut is more permissive than that used in typical post-starburst selections (French 2021) in order to select objects just beginning the quenching process. These cuts select a fairly heterogeneous parent sample of 121 galaxies that are mixture of classic post-starburst galaxies, blue galaxies with anomalously weak emission lines, some Type II AGNs, and a few post-starburst quasars.

From this parent sample, we followed up 50 objects at $z = 0.4$–0.8 to obtain deeper observed frame optical spectroscopy (see Section 3). In practice, our target selection was applied to the most recent SDSS DR available just prior to each of our observing runs, which spanned 2004–2012 (DR4–DR8). As a consequence of changes in the SDSS data processing pipeline, 13 galaxies where selected and subsequently observed, which are not in the DR8 parent sample described above. In selecting galaxies for follow-up, we prioritized those with the largest g-band fluxes and the youngest stellar populations, but we included galaxies with older bursts for comparison. Notably, we did not prioritize galaxies with Mg II absorption. In all but the brightest galaxies, the SDSS spectra were too noisy to enable robust detection of the interstellar Mg II lines, and we wished to remain unbiased in order to evaluate the incidence of Mg II absorption in our sample with follow-up spectroscopy.

It is worth keeping in mind that most studies of galaxy scaling relations aim to target typical star-forming galaxies at a given redshift, whereas the HizEA sample was selected to study comparatively rare galaxies caught in an early stage of the quenching process. However, as we discuss in subsequent sections, many of the HizEA galaxies have surprisingly high SFRs (and extreme values of $\Sigma_{\rm SFR}$) despite the imposed limit on their [O II] EW. In Section 7.4, we address the question of whether the HizEA galaxies should be used to study outflow scaling relations, and we conclude that these extreme galaxies are a useful addition to other studies that probe more typical star-forming galaxies.

2.2. HizEA Sample Properties

In order for the HizEA galaxies to be targeted by SDSS-I (i.e., to meet the quasar target selection apparent magnitude cut), they needed to be extraordinarily luminous ($M_g^{0.1} \sim -22.5$), much more luminous than a typical star-forming galaxy at $z \sim 0.6$ (Whalen et al. 2022). Such large luminosities require very massive galaxies that have recently experienced an extreme starburst. In Section 4.1.1, we show that the galaxies have stellar masses of 10^{10}–$10^{11.5}$ $M_\odot$. HST follow-up of 29 HizEA galaxies (Section 4.1.2) revealed strong evidence for late-stage, highly dissipational mergers (Diamond-Stanic et al. 2012; Sell et al. 2014), which likely triggered powerful central starbursts where ~30% of the galaxies stellar mass was formed (Diamond-Stanic et al. 2021). The space densities of these extreme galaxies are low at $z \sim 0.5$ ($\sim 10^{-6}$ Mpc^{-3}), but they appear to be consistent with the observed redshift evolution of compact star-forming galaxies (Whalen et al. 2022).

Because of our [O II] EW <15 Å cut and the fact that Hβ emission is usually only marginally detected, we expected the current SFRs of the HizEA galaxies to be low. However, most of the galaxies were detected in the MIR by the Wide-field Infrared Survey Explorer (WISE; Wright et al. 2010), suggesting the presence of dust-obscured star formation (Diamond-Stanic et al. 2012; Petter et al. 2020). Our modeling of their ultraviolet (UV) through MIR spectral energy distributions (SEDs) implies SFRs = 20–500 $M_\odot$ yr^{-1} (Section 4.1.1). Roughly 1/3 of the galaxies show blue stellar continua and modestly obscured ($A_V \sim 0.5$) young ionizing populations (see Geach et al. 2018). The weak emission lines in

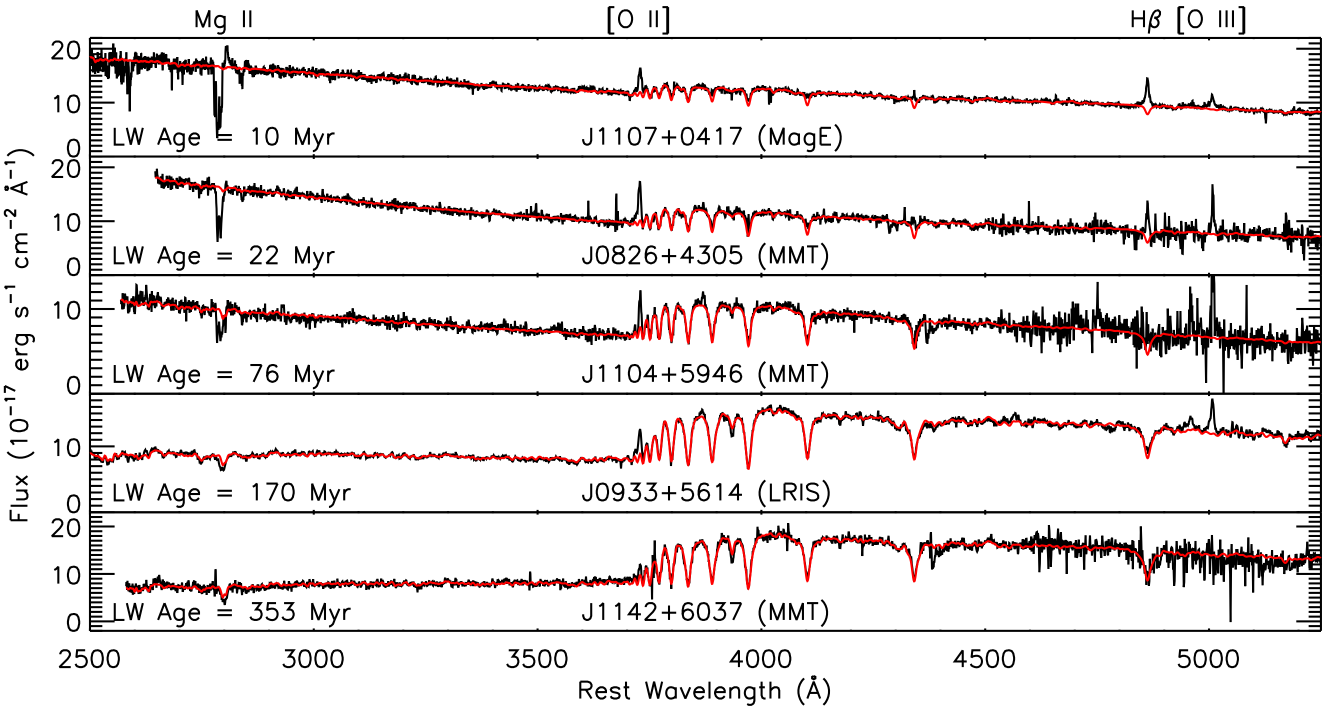

Figure 1. Example spectra of five HizEA galaxies (black) spanning a range of mean stellar ages. The spectrograph used (Section 3) is labeled in parenthesis after the galaxy name. The ages (labeled in the lower left of each panel) are the light-weighted age of the stellar populations younger than 1 Gry computed from our SED modeling (Section 4.1.1) with Prospector (Leja et al. 2019; Johnson et al. 2021). Models of the stellar continuum computed using the pPXF software (Cappellari & Emsellem 2004; Cappellari 2017) and the C3K stellar libraries (C. Conroy et al. 2023, in preparation) are shown in red (Section 4.2.1). Note the very blue OB-star dominated spectra at young ages, but the weak emission lines. These galaxies may be Lyman continuum leakers (see Section 2.2).

galaxies with ample ongoing star formation may be a consequence of Lyman continuum leakage, an idea we explore more fully in Perrotta et al. (2021). In some cases, part of the missing nebular emission may lie outside of the SDSS 3″ fiber aperture. For example, in the HizEA galaxy Makani (J2118+0017), the SDSS fiber encompasses only ∼25% of the total [O II] emission, with the remainder coming from the extended ionized outflow (Rupke 2018). The HizEA sample includes galaxies with mean stellar ages (Section 4.1.1) ranging from 10–400 Myr; roughly half of the sample has ages less than 100 Myr. Figure 1 shows spectra of 5 HizEA galaxies spanning a wide range of mean stellar ages.

In summary, the HizEA galaxies are massive late-stage galaxy merger remnants that host compact central starbursts. They are a mix of starbursts that peaked a few 10 s or 100 s of Myr ago that have comparatively small ionizing populations today and ongoing starbursts with weak optical emission lines due to Lyman continuum leakage or absorption. The galaxies are much more luminous than typical star-forming galaxies at these redshifts (see Rubin et al. 2014) and much bluer than galaxies with comparable SFRs (see Banerji et al. 2011). By selecting bright blue galaxies at $z > 0.4$ in the large volume of SDSS-I, we may have preferentially selected extreme starbursts capable of removing much of their ISM via powerful feedback events.

2.3. AGN Activity

HizEA galaxies are massive, $M_* \sim 10^{10}$–$10^{11.5}\ M_\odot$, and it is likely that they harbor supermassive black holes. It is therefore incumbent on us to consider whether black hole activity contributes to the feedback process in these galaxies. Below we summarize our multiwavelength investigations into AGN activity in this sample.

Of the 50 HizEA galaxies, two objects were intentionally selected to be post-starburst quasars based on strong broad Mg II emission lines in their SDSS spectra. One additional object that had a very noisy SDSS spectrum was revealed by follow-up spectroscopy to be an unusual post-starburst quasar. A fourth object lacked broad emission lines but showed strong spectral variability; it is likely a blazar. We eliminate these 4 Type I AGN from the present analysis, and focus on the remaining 46 galaxies, listed in Table A1. We retain one Type-I AGN in our sample, J2140+1209. This galaxy has a very weak Mg II broad emission line (Figure A5) on top of a primarily host galaxy-dominated continuum.

In Sell et al. (2014), we analyze Chandra X-ray observations of the 12 HizEA galaxies with the most AGN-like optical spectra (those with broad emission lines, [Ne V] emission, or a high [O III] 5007 luminosity). Of these 12 galaxies, only 2 were detected with >4 X-ray counts, and these were the galaxies with broad Mg II emission lines that have been eliminated from our present sample. For the other 10 objects, the small number of X-ray photons detected are consistent with arising from the high-mass X-ray binaries found in young stellar populations. Notably, the merged X-ray spectrum of the sources (while noisy) is relatively soft, disfavoring Compton-thick AGN.

In Petter et al. (2020), we analyze 1.5 GHz radio continuum observations from the JVLA of 19 HizEA galaxies. J0827+2954 is luminous at 1.5 GHz, and its image shows evidence of jet structure, leading us to classify it as a radio AGN. In the other 18 galaxies studied, the radio luminosities are consistent with arising from star formation. One additional galaxy, J0933+5614, is detected in the Very Large Array Faint Images of the

Radio Sky at Twenty cm survey (Becker et al. 1995) and is classified as a radio AGN.

In Perrotta et al. (2021), we analyze near-infrared spectra covering Hα and [N II] for 14 HizEA galaxies. Using an [O III] $\lambda5007/\mathrm{H}\beta$ versus [N II]$\lambda6583/\mathrm{H}\alpha$ (N2-BPT) diagram (Baldwin et al. 1981), we find that J1713+2817 falls in the AGN region of the diagram while the other galaxies lie in or near the "composite" region. Galaxies in the composite region are often interpreted as having contributions to their line ratios from both star formation and AGN; however, these intermediate line ratios are also found in galaxies experiencing shocks due to starbursts, mergers, and outflows (Rich et al. 2011; Soto et al. 2012; Kewley et al. 2013; Rich et al. 2014, 2015). Since the HizEA galaxies are known to be late-stage mergers with powerful starbursts and outflows, we consider shocks to be the most likely explanation for their line ratios.

All 46 of our galaxies are detected in the WISE (Wright et al. 2010) W1 and W2 bands. Based on the color criterion outlined by Stern et al. (2012, W1–W2 > 0.8), none of the galaxies are classified as AGN. However, this criterion only selects AGN that contribute least 30%–50% of the total bolometric luminosity (Blecha et al. 2018). Using the more conservative color selection criteria of Blecha et al. (2018, W1–W2 > 0.5), which were calibrated from simulations of galaxy mergers, 6 of our galaxies are classified as candidate AGN (including J2140+1209, our weak broadline source). The upcoming observations of 5 sources with the Mid-Infrared Instrument for the James Webb Space Telescope (MIRI; Rieke et al. 2015) will enable a better understanding of whether these galaxies host luminous dust-obscured AGNs.

In summary, of the 46 HizEA galaxies studied in this work, we find there is one Type I AGN with a weak Mg II broadline, one Type II AGN identified by its optical emission line ratios, two radio galaxies, and 5 candidate-obscured AGN with intermediate mid-IR colors. We retain these 9 galaxies in our sample because the AGNs do not dominate their bolometric luminosities. In Section 7.3.1, we consider whether these galaxies drive unusually fast outflows.

3. Observations and Data Reduction

We obtained medium- and low-resolution ($R = 600$–4000) optical spectra of our 46 galaxies from 2004–2012 using three different instruments on 6–10 m class telescopes. The goal was to obtain high signal-to-noise ratio (S/N; ∼15–30 per pixel) spectra of the Mg II $\lambda\lambda2796{,}2804$ ISM absorption lines in the galaxies in order to look for blueshifts of the lines relative to the starlight indicative of gas outflows. Unfortunately, the near-UV contains very few strong stellar or nebular features to aid in measuring the galaxy systemic redshift. Therefore, we required our spectra to extend to at least 4000 Å in the rest frame to cover the [O II] $\lambda\lambda$ 3726,3729 emission line and the low-order Balmer absorption lines.

An additional concern was properly accounting for any *stellar* Mg II absorption. We accomplish this by fitting stellar population synthesis models to the galaxy continuum with regions of possible ISM contamination masked out (see Section 4.2.1). To obtain the best possible stellar population model fit, we require spectrophotometrically calibrated data. Therefore, for all observing runs, we took special care to observe standard stars throughout the night as well as during the morning and evening twilight. The data and the quality of our spectrophotometry are discussed further in C. Tremonti et al. (2023, in preparation).

3.1. MMT/Blue Channel

We used the Blue Channel Spectrograph on the 6.5 m MMT (Angel et al. 1979) to obtain spectra of 32 galaxies. We used the 500 line mm^{-1} grating blazed at 5600 Å, which gave us spectral coverage from 3800 to 7000 Å with a dispersion of 1.19 Å pixel^{-1}. For our $z = 0.4$–0.8 galaxies, this yielded rest-frame coverage from ∼2700 to 3900 Å. Because most of our objects are unresolved in the SDSS imaging, we used a 1″ slit, which yielded an FWHM resolution of 3.6 Å ($\sigma \sim 85$ km s^{-1}) . The spectra were reduced, extracted, and spectrophotometrically calibrated using the ISPEC2D data reduction package (Moustakas & Kennicutt 2006).

The MMT spectra and the SDSS spectra generally agree extremely well, and they have comparable resolutions. To obtain even longer wavelength coverage for the purposes of stellar population modeling, the MMT spectra were joined with the (much noisier) SDSS spectra at around 7000 Å in the observed frame (∼4000–5000 Å in the rest frame).

3.2. Magellan/MagE

We used the Magellan Echellette (MagE) spectrograph (Marshall et al. 2008) on the Magellan Clay telescope to obtain spectra of 7 galaxies. The spectra cover 3200–10,000 Å in 15 orders ($\lambda_{\mathrm{rest}} \sim 2300$–$6000$ Å). We used a 1″ slit, yielding a resolution of $R \sim 4100$ ($\sigma = 31$ km s^{-1}). The data were reduced and calibrated using the MASE pipeline (Bochanski et al. 2009).

3.3. Keck/LRIS

We used the Low Resolution Imaging Spectrometer (LRIS; Oke et al. 1995) on the Keck I telescope to obtain spectra of 7 galaxies. We used a 1″ longslit and the D560 dichroic, with the 400/3400 grism on the blue side ($R \simeq 600$) and the 400/8500 grating on the red side ($R \simeq 1000$). The data were processed with the XIDL LowRedux pipeline.[12] The red and blue spectra were jointed together in the overlap region, providing continuous spectral coverage from $\lambda_{\mathrm{obs}} = 3200$–$8050$ Å ($\lambda_{\mathrm{rest}} \sim 2300$–$4700$ Å).

4. Analysis

4.1. Host Galaxy Properties

In the following sections, we briefly describe how we measure galaxy stellar masses, SFRs, and mean stellar ages from our spectra and archival photometry. Full details can be found in C. Tremonti et al. (2023, in preparation). We also discuss measurements of galaxy half-light radii made from HST data for 27 galaxies in our sample. Full details can be found in Diamond-Stanic et al. (2012), Sell et al. (2014), and Diamond-Stanic et al. (2021).

4.1.1. Stellar Masses, SFRs, and Ages

In order to estimate stellar masses and star formation histories (SFHs), we apply the `Prospector` code (Leja et al. 2019; Johnson et al. 2021) to fit our galaxies' broadband SEDs

---

[12] http://www.ucolick.org/~xavier/LowRedux/

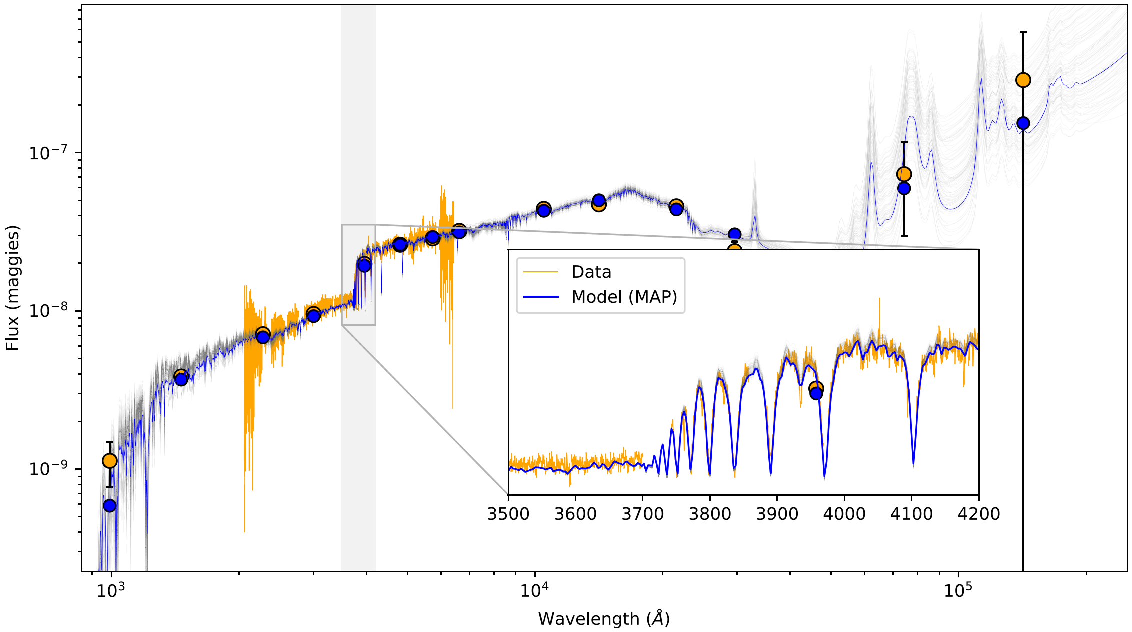

Figure 2. Example SED fit from Prospector (Johnson et al. 2021) for the galaxy J1052+0607 shown in the rest frame. Orange points with error bars indicate the galaxy's GALEX, SDSS, UKIDSS, and WISE photometry; the orange line is the optical spectrum, with the inset plot showing the region included in the fit. The blue line is the maximum a posteriori fit, and the blue points are photometric data synthesized from this model; gray lines are random draws from the probability distribution function. Masked regions around emission lines are not shown.

and spectra. `Prospector` employs gridless, Bayesian parameter estimation with the incorporation of robust posterior sampling algorithms. Our model includes free parameters on total stellar mass formed, stellar metallicity, diffuse and birth-cloud component dust attenuation, and dust emission via energy balance. Each have an associated prior probability distribution. We use a nonparametric SFH and impose a continuity prior (Johnson et al. 2021), which controls the SFR ratios between 14 adjacent, logarithmically spaced time bins.

Stellar population synthesis models were generated using the flexible stellar populations synthesis code (`FSPS`; Conroy et al. 2009) assuming a Kroupa IMF (Kroupa 2001) and adopting the MIST isochrones (Choi et al. 2016) and the C3K stellar libraries (C. Conroy et al. 2023, in preparation), which are fully theoretical. The choice of the C3K libraries is motivated by the fact that the default MILES stellar library lacks coverage of the hottest stars and produces poor fits to the spectra of galaxies dominated by very young (<10 Myr) stellar populations. (See C. Tremonti et al. 2023, in preparation for a more detailed discussion.)

The flexible framework of `Prospector` allows us to fit the rest-frame UV—mid-IR broadband photometry and high-resolution spectra simultaneously. Our photometric data comes from the Galaxy Evolution Explorer (GALEX; Morrissey et al. 2007), SDSS (Gunn et al. 1998; Ahumada et al. 2020), UKIRT Infrared Deep Sky Survey (UKIDSS; Lawrence et al. 2007) or VISTA Hemisphere Survey, and WISE (Lang 2014). While our spectra typically cover 2500–5500 Å, we use the 3500–4200 Å region in our `Prospector` fits because this spectral region contains many age-sensitive features (e.g., D4000, Hδ), and our spectrophotometric calibration is robust here. The posterior distribution is sampled with Markov Chain Monte Carlo (MCMC; Foreman-Mackey et al. 2013) using 10,000 iterations with 200 walkers. The best-fit parameters and their errors are computed from the 16th, 50th, and 84th percentiles of the marginalized probability distribution function.

In Figure 2, we show an example of our `Prospector` fit to the SED of J1052-0607, a fairly typical galaxy in our sample. Both the photometry and the spectra are very well fit by the model; however, the dust emission properties are poorly constrained due to the noisy WISE W3 and W4 photometry and the limited infrared coverage of the SED. This leads to fairly tight constraints on the stellar mass (±0.15 dex) and slightly larger errors on the SFR (±0.20 dex). In Figure 3, we show the inferred SFH for J1052-0607 along with the SFH of two other galaxies. The bursty SFHs shown here are characteristic of this sample (C. Tremonti et al. 2023, in preparation).

In this work, we utilize three quantities from our `Prospector` fits: the stellar mass, the SFR, and the mean stellar age. The surviving stellar mass is a direct output of our `Prospector` fits. Errors are typically ±0.25 dex for the galaxies with very recent starbursts and ±0.1 dex for galaxies dominated by older stellar populations. We compute SFRs from each galaxy's SFH averaging over 10 and 100 Myr timescales. These timescales are the characteristic timescales that Hα (10 Myr) and UV or IR (100 Myr) star formation indicators are sensitive to (Kennicutt & Evans 2012). Since most of our literature comparison sample (Section 5) have SFRs derived from UV and/or IR photometry, we opt to use the 100 Myr SFRs in the present analysis. However, we caution that these two SFR estimates can be very different for our bursty galaxies. To answer the question of which SFR is the most correct one to use to investigate outflow scaling relations, we need to consider the lifetime of outflows. Both observational and theoretical studies suggest that, once launched, outflows persist in galaxy halos for several 100 Myr (Coil et al. 2011; Lochhaas et al. 2018; Maltby et al. 2019; Rupke et al. 2019). Thus, we believe that the 100 Myr averaged SFRs are the most physically appropriate, in addition to being most consistent with the comparison sample, and better constrained by our data.

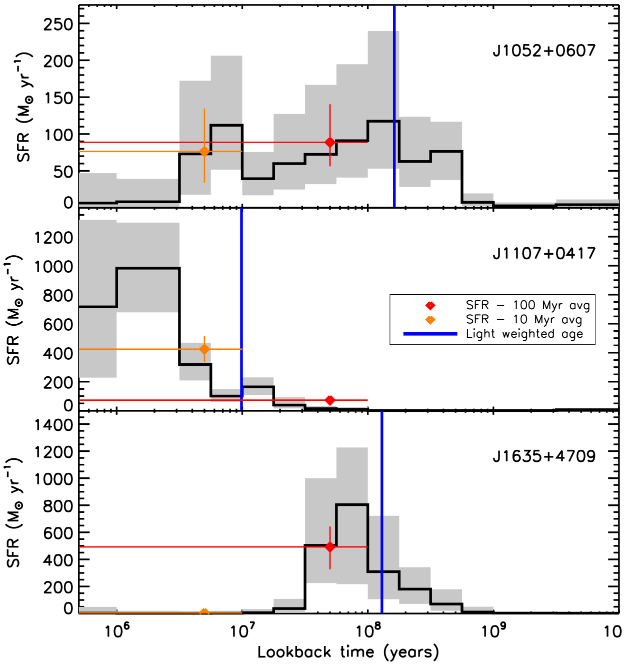

Figure 3. Example star formation histories for 3 galaxies derived with Prospector (Johnson et al. 2021). The gray shaded regions indicate the error on the SFH. The blue vertical lines denote the mean light-weighted age of the stellar populations younger than 1 Gyr. The orange and red symbols denote the present-day SFR averaged over 10 and 100 Myr timescales respectively. Time is shown on a logarithmic scale to highlight the recent SFH. However, this can give a misleading impression of the importance of the galaxy's recent SFH to the total stellar mass assembly. For example, J1107+0417 has formed only 14% of its total stellar mass in the last Gyr.

The mean stellar age of a galaxy can be defined in a number of different ways. Here, our primary aim is to identify the approximate timescale of the galaxy's most recent star-forming event, so we compute the light-weighted age of the stellar populations younger than 1 Gyr, with the light contribution estimated at 5500 Å. These 1 Gyr light-weighted ages are not as physically meaningful as mass-weighted ages, but they do a better job of approximating the timescale of the peak SFR. Light-weighted ages (cyan lines) are shown for 3 example galaxies in Figure 3.

For the Type I AGN, J2140+1209, the quasar continuum contaminates the spectrum and SED, accounting for ∼36% of the light at 5500 Å. We did not enable any of the AGN fitting modules in `Prospector`, and therefore the blue quasar light is fit by a young stellar population. This has a minor impact on the derived M_*, but a large impact on the SFR and light-weighted age. Therefore, for this galaxy, we take the SFR and light-weighted age measurements from our analysis of the UV–optical spectrum with the Penalized Pixel-Fitting (pPXF) software (Cappellari & Emsellem 2004; Cappellari 2017) described in Section 4.2.1. We account for the quasar light by including a Type I quasar template constructed from SDSS spectra in the spectral fitting. More details can be found in C. Tremonti et al. (2023, in preparation).

The stellar masses, SFRs, and mean stellar ages of the HizEA galaxies are reported in Table A1.

4.1.2. Galaxy Sizes and SFR Surface Densities

The sizes and morphologies of the HizEA galaxies are explored in detail in Diamond-Stanic et al. (2012), Sell et al. (2014), and Diamond-Stanic et al. (2021), but we include a brief summary here. A subset of 29 galaxies from the HizEA sample (27 of which are included in the present analysis) was observed with HST's Wide Field Camera 3 (WFC3; Kimble et al. 2008) with the UVIS/F814W filter (programs (12019) and (12272)). For 12 of the galaxies with F814W data, subsequent imaging was obtained in the UVIS/F475W and IR/F160W filters (program (13689)).

A ubiquitous property of the HizEA galaxies observed with HST is the presence of a bright compact core surrounded by fainter tidal features indicative of a recent merger. In roughly half of the galaxies that show no evidence of being Type I AGN, Sell et al. (2014) found that the structure of the HST point-spread function (PSF) is faintly visible, suggesting that the galaxies are nearly unresolved. This is remarkable considering that typical host galaxy half-light radii for $\log M_* > 10\,M_\odot$ SFGs at $z \sim 0.5$ are $0''.4$–$1''.7$ or ∼40–170 times the HST PSF FWHM (van der Wel et al. 2014).

To estimate the half-light radius of each galaxy, we first construct a high-quality model of the PSF from a combination of nearby stars in the image. We then fit the data with a 2D surface brightness profile convolved with the PSF and report the half-light radius of the best-fit model. For the 15 galaxies with only F814W imaging, a single Sérsic component with $n = 4$ was fit with GALFIT (Peng et al. 2002), as described in Sell et al. (2014). For the 12 galaxies with multiband imaging (Diamond-Stanic et al. 2021), Sérsic fits were performed to the F475W and F814W images jointly using the GALFITM software developed by the MegaMorph collaboration (Häußler et al. 2013; Vika et al. 2013). To avoid issues caused by the tidal features, the central region of the galaxy is fit first, and the fit is extrapolated to larger radii to compute the half-light radius. The half-light radii are listed in Table A1. We use values from the multiband fits of Diamond-Stanic et al. (2021; their $r_{e,\mathrm{total}}$) when available. The remaining radii come from the Sell et al. (2014) "Sérsic only" fits to the F814W images (4 galaxies) and from Diamond-Stanic et al. (2012; 12 galaxies). The HizEA galaxies are incredibly compact, spanning Sérsic radii of a hundred to a few thousand parsecs, with the most compact galaxy (J0905+5759) having a radius of $r_e = 0''.013$ or 97 pc.

The half-light radii (r_e) are measured at relatively blue rest-frame wavelengths, (λ_rest(F475W) ≈ 3000 Å, λ_rest(F814W) ≈ 5200 Å), and therefore they are reasonable tracers of the radii containing half of the relatively unobscured star formation. We compute SFR surface densities as follows: $\Sigma_\mathrm{SFR} = 0.5\,SFR/(\pi r_e^2)$. The compact sizes, coupled with large SFRs, create extremely large SFR surface densities (Table A1), up to $\Sigma_\mathrm{SFR} \approx 1800\,M_\odot\ \mathrm{yr}^{-1}\ \mathrm{kpc}^{-2}$, comparable to the most luminous IR-selected starbursts on the Schmidt—Kennicutt relation (Kennicutt & Evans 2012).

4.2. Outflow Properties

4.2.1. Stellar Continuum Modeling

To measure a Mg II outflow velocity, we must accurately constrain the galaxy's systemic velocity and properly normalize the continuum using a model of the stellar population. In order to accomplish both of these tasks, we fit the spectra with a combination of dust-reddened SSP models. We employed the flexible stellar population synthesis code (Conroy et al. 2009; Conroy & Gunn 2010) to generate SSPs with Padova 2008 isochrones (Marigo et al. 2008), a Salpeter (1955) IMF, and the C3K theoretical stellar library (C. Conroy et al. 2023, in preparation), which has a resolution of $R = 10{,}000$. These stellar models are very similar to the models used in our `Prospector` analysis (Section 4.1.1) over the wavelength range where the fitting is carried out ($\lambda_{\rm rest} \sim 2500$–5500 Å). We utilize solar metallicity SSP templates with 43 ages spanning 1 Myr and 8.9 Gyr. We perform the fit with pPXF software (Cappellari & Emsellem 2004; Cappellari 2017). However, we altered the code to use the Salim et al. (2018) reddening law for massive high-z analogs. We mask the region around Mg II and the forbidden emission lines (e.g., [O II], [O III]) during the fit. We do not mask the Balmer lines, rather we include the Balmer emission lines (assuming case (B) recombination line ratios) as an additional template subject to the same dust-reddening as the young stars. The low-order Balmer lines are typically in absorption in our spectra, but emission lines often infill the line core. By fitting emission and absorption simultaneously, we are able to retain these highly age-sensitive features in our fit.

The output of our pPXF fitting is the galaxy redshift, the stellar velocity dispersion, and a model of the stellar continuum. Examples of our fits are shown in Figure 1. The model continuum matches the data well enough that additional adjustments using polynomials or median filtered residuals were deemed unnecessary. We show our stellar population model in the 2750–2850 Å region for each of our spectra in Appendix A Figures A1–A6. For galaxies with young stellar populations (e.g., J0826+4305), the stellar contribution to Mg II is minimal; for galaxies with older populations (e.g., J0933+5614), the stellar Mg II absorption can be greater than the interstellar absorption. We normalize each spectrum by our best-fit pPXF model to properly remove the stellar component. The redshifts and velocity dispersions returned by pPXF are used as input for our `Prospector` models (Section 4.1.1).

4.2.2. Measuring Outflow Velocities and Mg II EWs

After the HizEA spectra are continuum-normalized and shifted into the rest frame, we model their Mg II line profiles. Due to the low-to-moderate resolution of the spectra ($R \sim 600$–4000), the saturated nature of the Mg II lines, and our primary goal of measuring outflow velocities, a Gaussian profile was chosen over a Voigt profile for fitting.

The Mg II ISM lines in galaxy spectra often exhibit a P-Cygni profile, in which resonance emission fills in part of the intrinsic absorption trough near systemic velocity (Martin & Bouché 2009; Weiner et al. 2009; Coil et al. 2011; Rubin et al. 2011; Erb et al. 2012; Zhu et al. 2015). This infilling can be corrected using detailed radiative transfer modeling (Prochaska et al. 2011) or empirical methods that leverage the Fe II λ2374 and λ2587 lines (Zhu et al. 2015). However, the resolution, S/N, and wavelength coverage of our spectra are insufficient to undertake these detailed corrections. We therefore adopt a simpler method of fitting a Gaussian doublet emission model where P-Cygni emission is evident, or the line profile is poorly fit without an emission component. The emission line center is fixed at the galaxy's systemic velocity, while width and amplitude are allowed to vary. However, we limit the amplitude to no more than 1.5X the highest point in the fitting region of the spectrum. This avoids a behavior of the fitting routine in which a physically unfeasible large emission component and large absorption component occur at nearly the same velocity, canceling one another out.

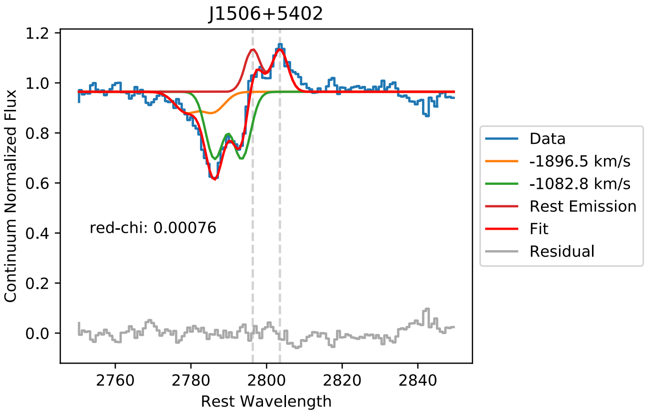

Figure 4. An example of a Mg II outflow profile fit with multiple Gaussian absorption components and a rest-velocity emission component. The rest wavelengths of the Mg II doublet are indicated by the vertical gray dashed lines. The velocities indicated in the legend refer to the individual line component velocities. The outflow velocities computed from the composite line profile are shown in Figure 5.

We perform multicomponent Gaussian fitting of the emission and absorption profiles using Python `lmfit`, a nonlinear least squares minimization and curve-fitting package (Newville et al. 2014). Assuming saturation, the doublet is modeled as two equal-amplitude, equal-width Gaussians at fixed separation. We apply between one and three of these Gaussian doublet models to fit the apparent velocity components of the overall absorption profile. For each velocity component, the parameters fit are the λ2796 line center, the amplitude (which is applied to both lines of the doublet), and width (also applied to both lines of the doublet). These parameters are allowed to vary within user-defined physically feasible bounds. Our fit does not require a zero-velocity absorption component, but zero-velocity absorption is not excluded from the fit.

The fitting routine is fed an initial guess for the parameters determined by eye, then iterates the initial central wavelength in 0.5–1 Å steps until `lmfit` converges, and the reduced-chi squared value is minimized. The sensitivity of the fit to the initial guess was tested by iterating through 10 randomized starting values based on the initial guess (e.g., allowing the line center to vary randomly within ±3 Å from the initial *best* guess). The randomized initial fitting parameter values returned profile velocities that were equal to the *best* initial guess, or else resulted in visibly poor fits. We thus conclude the overall fit is not particularly dependent on the initial parameters. An example of one of our Mg II line profile fits is shown in Figure 4. Line fits for the full sample can be found in Appendix A (Figures A1–A6).

We are not confident that individual velocity components can be robustly identified and deblended in our low-resolution to medium-resolution spectra (R = 600–4000, depending on the instrument). Therefore, we use velocities measured from the fitted composite absorption line profile in our analysis. Since the two lines of the Mg II doublet tend to blend, we take one member of the doublet (i.e., Mg II λ2796) to calculate our outflow velocities and create a composite absorption profile (see Figure 5 and the rightmost panel of Figures A1–A6). A cumulative equivalent width is calculated across this profile, going from positive to negative velocities. Outflows are

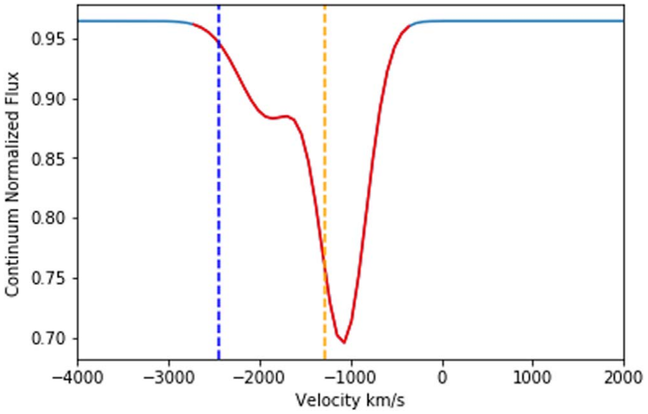

Figure 5. An example of the fitting of average and maximum outflow velocity for the galaxy J1506+5402 from Figure 4. A composite profile using just the blueward (i.e., Mg II λ2796) member of each velocity component doublet is constructed. The area for which cumulative equivalent width is calculated is indicated in red. The average velocity (orange vertical line) is where the cumulative equivalent width reaches 50%; the maximum velocity (blue vertical line) is where the cumulative equivalent width reaches 95% of the total equivalent width.

characterized using two different velocities: one measured at the 50th percentile of the cumulative equivalent width distribution, hereafter V_{avg}, and one at the 95th percentile, hereafter V_{max}. Calculated velocities can be found in Table A1. An example is shown for the galaxy J1506+5402 in Figure 5.

While Python `lmfit` returns errors on all fit parameters, these errors are small (of the order of a few percent). Propagating these errors resulted in velocity measurement errors that were physically unrealistic given the data quality (e.g., 5 km s^{-1} for outflow velocities of >1000 km s^{-1}). We therefore calculate our outflow velocity errors by fitting each spectrum 100 times, in which each iteration modulates the spectrum randomly by its associated pixel errors. The same initial guess is applied to each noise-modulated spectrum, and its V_{avg} and V_{max} are calculated. The standard deviation of these 100 velocity values is then taken as the error on the outflow velocity measurement.

Emission line infilling of the Mg II absorption profile has been shown to bias velocity measurements (especially V_{avg}) to larger negative velocities (Zhu et al. 2015). To check that our correction for infilling is adequate, we compared our fitted Mg II line profiles with the Fe II λ2587 absorption line, which has minimal infilling due to the nonresonant emission channels of Fe II* λ2613, λ2632. For the 7/46 galaxies in our sample with coverage of Fe II λ2587 at adequate S/N, we found that three targets matched well in velocity centroid (ex. J1341-0321), two had bluer Mg II centroids (ex. J0939+4251), and two had bluer Fe II centroids (ex. J1039+4537). The magnitude of the difference in the centroids was on the order of the error in our Mg II measurements (100–300 km s^{-1}). This mixed result is thus not immediately alarming, but it precludes any strong conclusions about the systematic effects of resonant emission on our measured Mg II velocities.

Perrotta et al. (2023) use the high S/N, high-resolution ($R \sim 37{,}000$) Keck/High Resolution Echelle Spectrometer (HIRES) spectra to examine the absorption and emission line kinematics of 14 HizEA galaxies in greater detail. With their high-quality data, they are able to construct detailed multi-component models of the emission and absorption. They conclude that emission line infilling of Mg II is not a significant concern in most galaxies. This is partly due to the fact that the emission is near systemic velocity while most of the absorption is significantly blueshifted. They compare the Mg II and Fe II velocity components and find that the relation between the two is complex (see their Figure 11). Some high-velocity components seen in Mg II appear to be missing in Fe II, even when differences in oscillator strength and covering factor are accounted for. Thus, Mg II appears to be the best transition for probing the full velocity extent of the cool ionized outflow.

5. Data from the Literature

To place the HizEA galaxies and their outflows in context, we assemble a large comparison sample from the literature. While there are now dozens of observational studies of outflows, we limit our comparison to measurements most comparable to our own in technique (near-UV absorption lines) and dominant power type (starburst-driven rather than AGN-driven).

Four of our 46 galaxies host AGN, but the bolometric luminosities across the whole sample are dominated by star formation activity (see Section 2.3), leading us to exclude any AGN-driven outflow studies. Studies using warm ionized gas tracers in emission (e.g., Hα, [O III]) are avoided as discrepancies have been found between emission and absorption line tracers of outflows (see Wood et al. 2015). Molecular tracers are eliminated as they are not tracing the same gas phase. Many well-known outflow studies utilize Na I D $\lambda\lambda$ 5892,5898 absorption lines (see Rupke et al. 2005), but the low ionization potential of Na I (5.1 eV) means that it is primarily associated with cool neutral and/or molecular phases, which may have lower outflow velocities than the warm ionized gas traced by Mg II (Veilleux et al. 2020). We comment on this further in Section 5.1.

We note that one recent and potentially relevant analysis, the CLASSY sample from Xu et al. (2022), met our criteria for non-AGN hosts measured with UV lines tracing warm ionized gas. However, the overlap of this sample with the sample in Chisholm et al. (2015) and the difference in their chosen line measurement technique ultimately led us to exclude this sample; though, we do make reference to some of their results in Section 7.

We have selected 10 comparison samples that primarily consist of galaxies where outflows are measured using the rest-frame ultraviolet absorption lines of Mg II, Fe II, or Si II. We include both measurements made on individual galaxy spectra and those made from stacked composite spectra involving 10–100 s of galaxies. The comparison samples are summarized in Table 1. We elaborate on relevant details of each of our comparison samples in Appendix B and address variations in fitting and velocity measurement techniques below. Following the conventions in Zahid et al. (2012), we scale our values from Prospector and all reference sample SFRs to a common Chabrier IMF. We convert from a Salpeter IMF to a Chabrier IMF by dividing by 1.7. We scale from a Kroupa IMF to a Chabrier IMF by dividing by 1.06.

5.1. Sample Comparison Considerations

When viewing any set of outflow samples together for the purpose of deriving scaling relations, a number of confounding factors emerge. The literature on measuring outflow velocity is extensive, with each study making use of different ion species,

Table 1
Summary of Observational Comparison Sample Properties

Sample	Species	Redshift Range	Composite	$N_{\rm galaxies}$[a]	Velocity Fit	$V_{\max}$ Type	Ancillary Data
HizEA	Mg II	0.40–0.81	No	46	$v_{\rm avg}$,$v_{\max}$	95%	M_*, SFR, sSFR, $\Sigma_{\rm SFR}$
Banerji+ 2011	Mg II	$z\sim1.3$	Yes	22	$v_{\rm avg}$,$v_{\max}$	90%	M_*, SFR, sSFR, $\Sigma_{\rm SFR}$
Bordoloi+ 2014a	Mg II	1.00–1.50	Yes	486[b]	$v_{\rm avg}$	⋯	M_*, SFR, $\Sigma_{\rm SFR}$
Chisholm+ 2015	Si II	0.00–0.26	No	48	$v_{\rm avg}$,$v_{\max}$	90%	M_*, SFR, sSFR
Heckman+ 2015	Si III, C III, N II	0.00–0.23	No	36	$v_{\rm avg}$	⋯	M_*, SFR, sSFR, $\Sigma_{\rm SFR}$
Kornei+ 2012	Mg II, Fe II	0.25–1.34	Yes	72[c]	$v_{\max}$	Cont-1σ	SFR, sSFR, $\Sigma_{\rm SFR}$
Martin+ 2012	Mg II, Fe II	0.64–1.29	No	29	$v_{\max}$	Cont-1σ	M_*, SFR, sSFR
Prusinski+ 2021	Mg II, Fe II	1.00–1.50	No	73	$v_{\rm avg}$,$v_{\max}$	100%[d]	M_*, SFR, sSFR, $\Sigma_{\rm SFR}$
Rubin+ 2014	Mg II, Fe II	0.00–1.38	No	64	$v_{\rm avg}$,$v_{\max}$	75%[e]	M_*, SFR, sSFR, $\Sigma_{\rm SFR}$
Sugahara+ 2017	Mg II	$z\sim1.4$	Yes	662[b]	$v_{\rm avg}$	⋯	SFR
Weiner+ 2009	Mg II	$z\sim1.4$	Yes	1406[b]	$v_{\rm avg}$	⋯	M_*, SFR

Notes.

[a] Number of galaxies included in this paper's scaling relation plots.

[b] Bordoloi et al. (2014) have a sample of 486 galaxies, but composite spectra are constructed from subsets of 103 to 237 galaxies, depending on the property measured and bin definition (e.g., low SFR, medium SFR, high SFR). Weiner et al. (2009) have a sample of 1406 galaxies, with 339 to 678 galaxies per property and/or bin. Sugahara et al. (2017) has 3 Mg II bins with 662, 394, and 277 galaxies.

[c] Kornei et al. (2012) composite points are "binary splits" of the data along galaxy property, putting half of the sample in each property bin (e.g., low SFR or high SFR).

[d] Prusinski et al. (2021) define the maximum velocity as the velocity corresponding to the wavelength at which the absorption profile first meets the normalized continuum (i.e., has a value of 1) on the blue side of the line, determined from an average of 5000 Monte Carlo iterations.

[e] Rubin et al. (2014) fit two components (systemic and outflowing) and obtain their maximum velocity from the velocity center of the outflowing (flow) component through the following relation: $\lambda_{0,\max}=\lambda_{0,\rm flow}\times(1-\frac{b_D}{\sqrt{2}c})$. We correct this value to a 95% velocity as described in Appendix B.

different redshift ranges, different measurement methods, different resolution data, and different velocity definitions. Some studies present results from individual spectra, while others only measure velocities from composite stacks of tens to hundreds of galaxy spectra. Acquiring and applying a uniform spectroscopic analysis to all relevant samples is not feasible, so we briefly note below the factors that should be taken into account when interpreting the analysis in this paper. An extended description of these considerations can be found in Appendix C

Variations in spectral fitting are a first possible contribution to the scatter in our scaling relations. Not all of the reference samples normalize the data by a stellar continuum model, so stellar Mg II contamination may be present. Each study also varies in how it treats emission in-filling in the Mg II line. Some samples remove the systemic component before fitting outflow velocity components, but not all. The outflow velocity components that are measured vary in how they are defined, especially for maximum velocities. The next major factor is the different ionic species used. While we tried to use only samples similar to our Mg II transition, the references still span 6 different ions with potentials between 15 and 48 eV. Finally, there is ongoing debate about redshift evolution for galaxy outflows (Sugahara et al. 2017; Calabrò et al. 2022). While we limit our sample to studies of $z<1.5$, this may be an additional contribution to the scatter.

While the concerns listed in this section should be considered when drawing conclusions from the scaling relations, we have taken steps to create a reasonably homogeneous sample from a large and varied literature collection. Beyond selecting for similar targets, redshifts, and ionic species, we have applied corrections to velocity measurements to closer align them with our definitions (noted where applicable in Appendix B), and unified the IMFs to a Chabrier IMF by applying correction factors. Other works comparing a large number of reference samples do not necessarily homogenize their sample in this fashion. In Nelson et al. (2019), they compare a more general collection of 13 reference samples (including some used in this paper). Their scaling relation for outflow velocity versus SFR has a scatter of over ∼1 dex while our sample has a scatter of ∼0.7 dex. Carefully selecting a most-similar sample has reduced the scatter in our scaling relations, minimizing the confounding factors even if they cannot be fully eliminated.

6. Outflow Scaling Relations

The HizEA galaxies have remarkable outflow velocities, with values reaching as high as $V_{\rm avg}\sim2600$ km s^{-1} and $V_{\max}\sim3200$ km s^{-1}. These extreme velocities led to previous speculation that the galaxies harbored heavily obscured AGNs (Tremonti et al. 2007), but subsequent work has found little evidence in support of this (see Section 2.3). Here we consider whether the HizEA galaxies represent a natural extension of the star-forming galaxy sequence by exploring their position on a variety of well-known outflow scaling relations–correlations between outflow velocity and host galaxy physical properties. To make this comparison, we have compiled data from 10 different star-forming galaxy samples in the literature described in detail in Appendix B and summarized in Table 1. We have standardized the M_* and SFR values to a common Chabrier IMF (Chabrier 2003), and we consider velocity measurements similar to our $V_{\rm avg}$ and $V_{\max}$.

While there remain a host of potential systematic issues (described in detail in Appendix C), Figures 6–7 show good agreement among the various literature samples. Outflow scaling relations have historically shown large intrinsic scatter ($\sigma\sim0.2$ dex; Chisholm et al. 2015; Heckman et al. 2015), and therefore a large sample is necessary to accurately characterize trends. Our data set from the literature includes 296 individual galaxies and 5 stacked samples representing another 3319 galaxies. As discussed in Section 5, we find our scatter to be

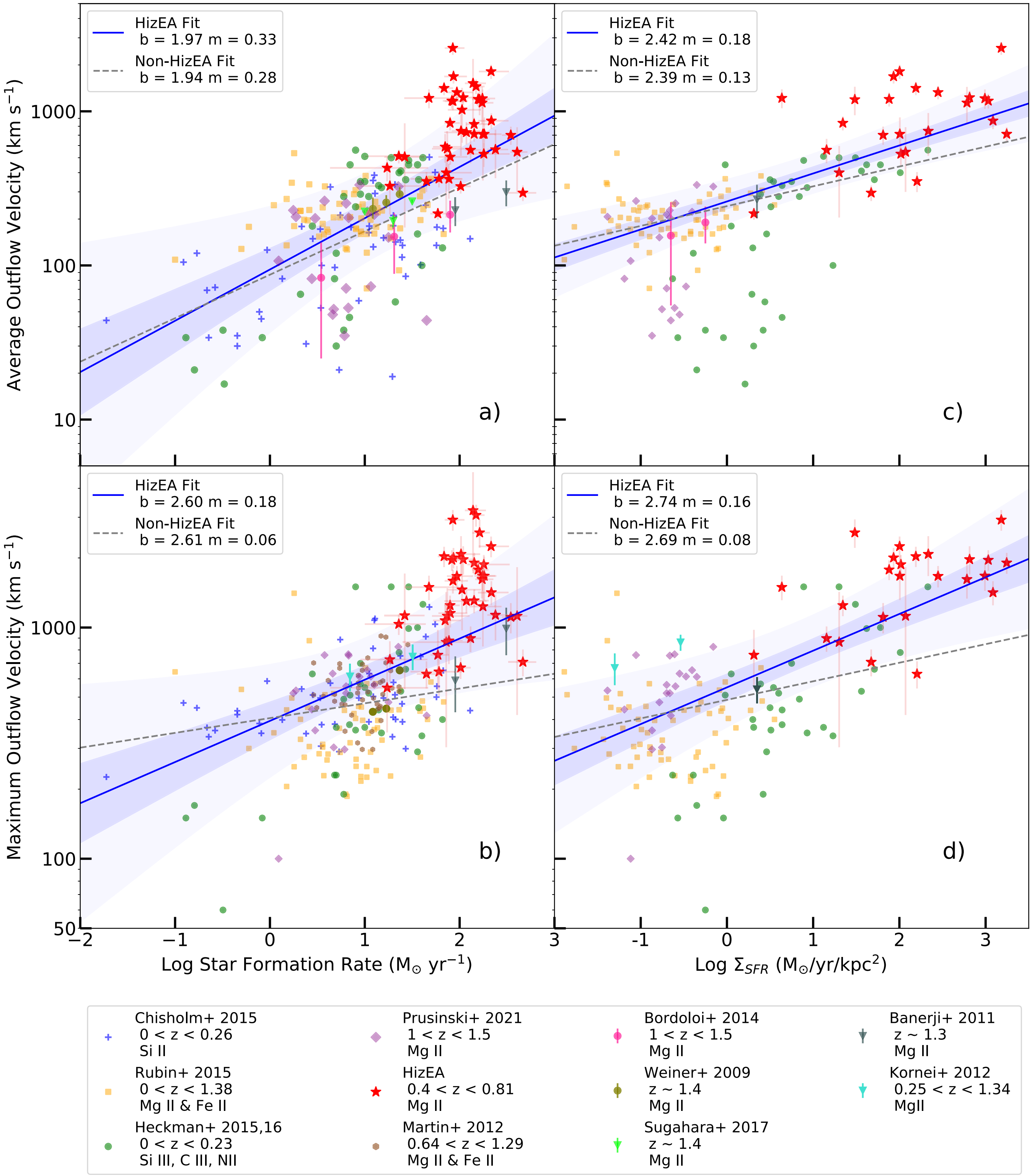

Figure 6. Scaling relations between outflow velocity and star formation rate (a), (b) and $\Sigma_{\rm SFR}$ (c), (d). We show the EW-weighted average velocity ($V_{\rm avg}$) in panels (a) and (c), and the maximum velocity ($V_{\rm max}$) measured at the 95th percentile of the cumulative EW distribution in panels (b) and (d). The HizEA sample is denoted by red stars. Error bars on data points are included only for our sample and reference sample points representing stacked data, for clarity. Fit lines are an MCMC-generated linear fit to the data, binned by 0.5 dex, with 1σ and 3σ error regions shaded in blue. We additionally include a gray dashed line indicating the fit without the HizEA sample included.

half of the previous scaling relation samples, thanks to the careful curation of this collection.

We explore well-known scaling relations between outflow velocity ($V_{\rm avg}$ and $V_{\rm max}$) and M_*, SFR, sSFR, and $\Sigma_{\rm SFR}$. To quantify these relations, we first compute the median of log $V_{\rm avg}$ and log $V_{\rm max}$ in bins of 0.5 dex in the independent variable (e.g., log SFR), then perform a linear fit to the median points (in log–log space). The fitting is carried out with the Python

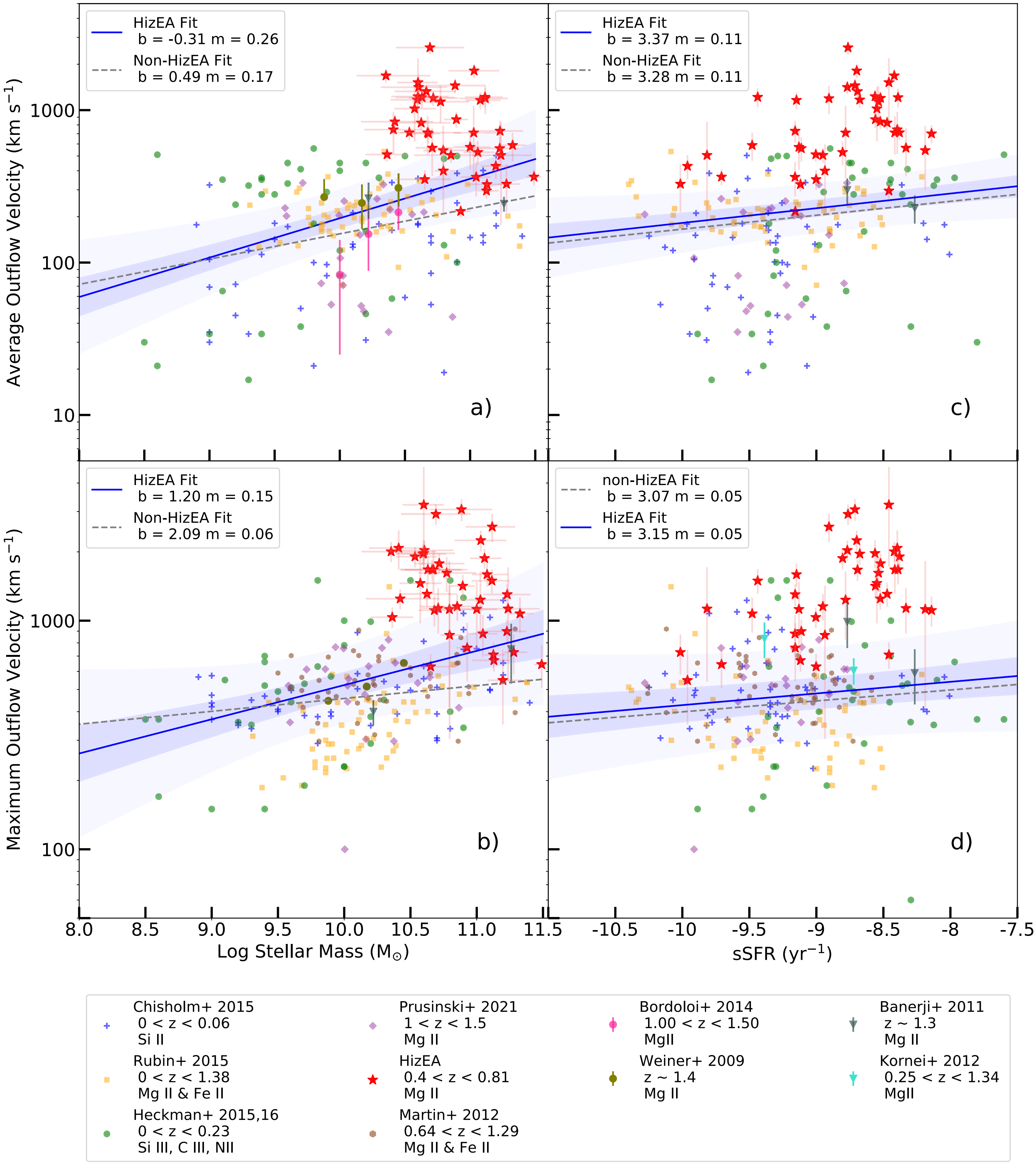

Figure 7. Scaling relations between outflow velocity and stellar mass (a), (b) and specific star formation rate (sSFR $\equiv$SFR$/M_*$) (c), (d). We show the EW-weighted average velocity ($V_{\rm avg}$) in panels (a) and (c), and the maximum velocity ($V_{\rm max}$) measured at the 95th percentile of the cumulative EW distribution in panels (b) and (d). The HizEA galaxies are denoted by red stars. Error bars on data points are included only for our sample and reference sample points representing stacked data, for clarity. Fit lines are an MCMC-generated linear fit to the data, binned to 0.5 dex, with 1σ and 3σ error regions shaded in blue. We additionally include a gray dashed line indicating the fit without the HizEA sample included.

MCMC package `PyMC3`, with which we compute a linear model to obtain the slope, *m*, and intercept, *b*, as well as their uncertainties. The error bars on the fit are the result of the MCMC process, in which random sampling on the priors (the coefficients of the fit) is performed. This implicitly generates uncertainties by assuming randomness in the data, and as such precludes the need to use the errors of the individual data points. We additionally characterize the correlation of the individual data points using the Spearman ρ, which traces monotonicity, and Pearson *R*, which traces true linearity. We

Table 2
Summary of Correlation Coefficients and Fits

Property	$V_{\rm avg}$						$V_{\rm max}$					
	ρ	r	FVU	b	m	$m_{\rm comp}$	ρ	r	FVU	b	m	$m_{\rm comp}$
M_*	0.41	0.21	0.96	-0.33 ± 0.52	0.26 ± 0.05	0.20 ± 0.05	0.51	0.28	0.89	1.18 ± 0.52	0.15 ± 0.05	0.12 ± 0.03
SFR	0.63	0.56	0.72	1.97 ± 0.12	0.33 ± 0.08	0.35 ± 0.06	0.56	0.57	0.67	2.60 ± 0.54	0.18 ± 0.05	0.08–0.32
sSFR	0.39	0.33	1.01	3.38 ± 0.36	0.11 ± 0.04	⋯	0.19	0.25	1.11	3.23 ± 0.29	0.06 ± 0.03	⋯
$\Sigma_{\rm SFR}$	0.58	0.69	0.50	2.42 ± 0.05	0.18 ± 0.03	⋯	0.53	0.72	0.42	2.74 ± 0.06	0.16 ± 0.03	⋯
SFR/R	0.61	0.69	0.38	2.20 ± 0.10	0.25 ± 0.05	⋯	0.59	0.73	0.47	2.50 ± 0.10	0.25 ± 0.05	⋯

Note. Various statistical measurements of the scaling relations and their scatter. ρ is the Spearman rank order correlation coefficient while r is the Pearson linear correlation coefficient. For both ρ and r, 0 implies no correlation, and 1 is perfect correlation. All correlation coefficients had p-values $< < 0.001$. The fraction of variance unexplained (FVU) is (1 - R^2), where R is the sum of squares of the regression over the total sum of squares. This is the scatter in the data not explained by the relationship between the independent and dependent variable. This value is 0 for a perfect fit and 1 for no correlation (or >1 if the model fit is no better than a horizontal line through the data). m and b are the fit parameters from our MCMC linear fit to the scaling relations in log–log space (i.e., $\log V = m \log x + b$, where x is SFR, M_*, sSFR, or $\Sigma_{\rm SFR}$). These fits are shown as blue lines in Figures 6 and 7. $m_{\rm comp}$ is the median power-law slope from a compilation of seven different outflow scaling relations in the literature (Rupke 2018).

also report the fraction of variance unexplained (FVU), which is a measure of the scatter that is not attributed to the relation between the independent and dependent variable. The results are summarized in Table 2. While a comparison of these measured coefficients is informative, we caution that different data sets from the literature contribute to each of the 8 trends that we explore.

6.1. *Outflow Velocity versus SFR*

In Figures 6(a), (b), we explore the scaling relation between outflow velocity ($V_{\rm avg}$ and $V_{\rm max}$) and SFR for star-forming galaxies at $z = 0$–1.5. Because not all surveys measure both $V_{\rm avg}$ and $V_{\rm max}$, the reference samples are different on the two plots. For clarity, we do not include error bars on data points that represent individual galaxies in the reference sample, but we include error bars on data from composite "stacked" spectra (i.e., Weiner et al. 2009; Kornei et al. 2012; Bordoloi et al. 2014; Sugahara et al. 2017). A clear positive correlation between outflow velocity and SFR is evident in both plots, as has been found in numerous surveys (Heckman et al. 2000; Martin 2005; Rupke et al. 2005; Weiner et al. 2009; Martin et al. 2012; Kornei et al. 2012; Bordoloi et al. 2014; Rubin et al. 2014; Chisholm et al. 2015, 2016; Heckman et al. 2015; Heckman & Borthakur 2016; Cicone et al. 2016; Prusinski et al. 2021). We show the best-fit relation defined by the reference sample as a gray dashed line on the plot.

The red stars in Figure 6 indicate the HizEA galaxies. We include 43/46 galaxies where the Mg II absorption EW $>$ 0.85 Å and by-eye inspection of the line fits (Figures A1–A6) found them to be acceptable. The HizEA galaxies have SFRs an order of magnitude higher than those found in the reference sample, but their high SFRs do not fully explain their extreme outflow velocities. Relative to the trend line fit to the comparison sample (gray dashed line), 24/43 HizEA galaxies are more than 3σ outliers toward higher $V_{\rm avg}$, and 25/43 galaxies are 3σ outliers toward higher $V_{\rm max}$. We also perform a two-sample Kolomogorov–Smirnov (KS) test. We take the fit line calculated for only the reference sample and measure the differences for the reference sample and the HizEA sample with respect to that line. These differences are then the two samples for our KS test. We find that the HizEA sample is drawn from a different distribution for SFR ($p < 0.001$). The blue line shows the fit to the data when the HizEA galaxies are included. The linear fit coefficients, as well as the Spearman ρ and Pearson R correlation coefficients, for the combined sample are reported in Table 2.

6.2. *Outflow Velocity versus Star Formation Surface Density*

In Figures 6(c), (d), we explore the relationship between outflow velocity ($V_{\rm avg}$ and $V_{\rm max}$) and star formation surface density ($\Sigma_{\rm SFR}$). $\Sigma_{\rm SFR}$ measurements are only available for the 27 HizEA galaxies with constraints from HST on their sizes (Section 4.1.2). Many of the HizEA galaxies have high SFRs ($>100\,M_\odot$ yr^{-1}) and remarkably compact sizes ($r_e < 500$ pc; Sell et al. 2014; Diamond-Stanic et al. 2021), resulting in extraordinary $\Sigma_{\rm SFR}$ values, up to $1755\,M_\odot$ yr^{-1} kpc^{-2}, approaching the theoretical limit for radiation pressure feedback (Murray et al. 2005).

A correlation between $V_{\rm out}$ and $\Sigma_{\rm SFR}$ has been noted by several authors, but typically the dynamic range of the samples in $\Sigma_{\rm SFR}$ has been small ($\sim$2 orders of magnitude) making firm conclusions difficult (Chen et al. 2010; Kornei et al. 2012; Rubin et al. 2014; Prusinski et al. 2021). The studies of Heckman et al. (2015), Heckman & Borthakur (2016), which include a sample of low-redshift "Lyman Break Analogs" (LBAs) explicitly selected for their compactness (Heckman et al. 2005), probe galaxies spanning more than 4 orders of magnitude in $\Sigma_{\rm SFR}$, and they find that $\Sigma_{\rm SFR}$ is the parameter most tightly correlated with outflow velocity. Where the samples overlap in $\Sigma_{\rm SFR}$, the HizEA galaxies show marginally higher outflow velocities than those from LBAs. However, for the most part, the HizEA sample smoothly extends the trends defined by the reference sample. We perform a two-sample KS test on the differences between the reference sample and the HizEA sample from the reference-only fit line, and find that the HizEA sample is drawn from the same distribution ($p = 0.041$).

Heckman & Borthakur (2016) posit a flattening in the $V_{\rm max}$–$\Sigma_{\rm SFR}$ relation at $\Sigma_{\rm SFR} > 100\,M_\odot$ yr^{-1} kpc^{-2} such that velocities asymptote to $V_{\rm max} \sim 2000$ km s^{-1}. While such a flattening is consistent with our data, additional data is needed before such higher-order correlations can be evaluated. Notably, below $\Sigma_{\rm SFR} = 3\,M_\odot$ yr^{-1} kpc^{-2}, the $V_{\rm avg}$–$\Sigma_{\rm SFR}$ correlation becomes much noisier, with a strong tail to low outflow velocities. This may reflect the importance of secondary parameters such as inclination (see Chen et al. 2010; Rubin et al. 2014; Bordoloi et al. 2014) or stellar mass at low values of $\Sigma_{\rm SFR}$.

6.3. Outflow Velocity versus Stellar Mass

In Figure 7, we show the outflow scaling relations involving stellar mass. Stellar mass has previously been found to have some correlation with outflow velocity (e.g., Martin 2005; Rupke et al. 2005; Rubin et al. 2014; Chisholm et al. 2015; Heckman & Borthakur 2016). In most of these works, however, there was not enough dynamic range in SFR at fixed mass to disentangle which is the primary driver—stellar mass or SFR—since stellar mass is correlated with SFR (the SFR main sequence; Noeske et al. 2007; Kouroumpatzakis et al. 2021). With our combined sample, we can see that the V–M_* relations have 1.3 times more scatter that the $V-$ SFR relations (Table 2). The HizEA galaxies have similar stellar masses compared to some of the galaxies in the reference sample ($\log M_* = 10.5$–11.5) but much higher SFRs and $\Sigma_{\rm SFR}$; nearly all lie above the fitted trend for the reference sample in the V–M_* plot. It is increasingly evident that stellar mass is not fundamentally correlated with outflow velocity. This finding is important for future simulation projects, as many wind simulation subgrid prescriptions scale the outflow velocities to mass (typically halo mass or virial velocity; Somerville & Davé 2015).

6.4. Outflow Velocity versus Specific SFR

In the lower panel of Figure 7, we explore the correlation between outflow velocity and sSFR (sSFR $\equiv$SFR$/M_*$). The HizEA galaxies overlap the reference sample in sSFR but typically have higher velocities. Their inclusion in the sample marginally increases the scatter (∼10%). Intuition suggests the outflow velocity should be tightly correlated with sSFR since the momentum injection rate scales with the SFR, and the gravitational potential that the wind must overcome scales with M_*. However, this is the least well-correlated parameter of those we explore. The absence of a strong trend with sSFR was also noted by Chen et al. (2010), Martin et al. (2012), and Heckman & Borthakur (2016). The lack of correlation between outflow velocity and sSFR is interesting, because it implies that outflows are not self-similar: a small galaxy and a large galaxy that have the same SFR$/M_*$ will not drive similar outflows. The reasons for this may have to do with the details of how cold gas persists in hot outflows, a topic we touch on briefly in Section 7.2.

7. Discussion

7.1. Incidence of Detection

Of the 46 non-AGN HizEA galaxies, we detect Mg II absorption from outflows in 42 (44 when counting marginal cases such as J1506+6131 with low S/N or large velocity measurement errors), yielding a wind incidence rate of at least 91%. In our reference sample, where stated, outflows are detected in 40% (Kornei et al. 2012), 67.5% (Martin et al. 2012), 66% (Rubin et al. 2014), and 92% (Heckman et al. 2015) of galaxies. Therefore, with the notable exception of the UV-selected Heckman et al. (2015) sample, the comparison sample exhibits a much lower outflow detection rate than that of the HizEA galaxies. A wind detection rate of 90% is also reported for the CLASSY galaxies (Xu et al. 2022), a sample of local UV-bright starbursts observed with HST/Cosmic Origins Spectrograph (COS; see Section 5.1 for notes on why this sample was not included in the scaling relations). One possibility is that samples selected for their rest-frame UV brightness may favor galaxies with outflows that have cleared out some of the dusty ISM. Another possibility is that starburst samples preferentially select mergers. Rubin et al. (2014) noted that galaxies with disturbed morphologies have a higher wind detection rate (83% versus 66% for the full sample). Rupke et al. (2005) also finds high incidence in mergers, showing that winds can be found in a large fraction of infrared-luminous galaxies and especially in ultraluminous infrared galaxies (ULIRGs; up to 80%).

As examined in several outflow works (Heckman et al. 2000; Rupke et al. 2005; Chen et al. 2010; Martin et al. 2012; Rubin et al. 2014), the detection rate of winds is strongly dependent on the host galaxy orientation and on the wind geometry. In Rubin et al. (2014), they detect winds in ∼89% of face-on galaxies, but only ∼45% of edge-on galaxies, with little variation in detection rate based on intrinsic galaxy properties. They conclude that biconical outflows are ubiquitous on the star-forming sequence at $z\sim0.5$. In mergers, though, the assumption of biconical outflows becomes less clear among messy tidal interactions. Rupke et al. (2005) posits a spherical, viewing-angle agnostic outflow geometry to explain their high detection rate, which could be the case for the HizEA sample as well. With such compact galaxies, we largely lack information about the viewing angle to test this idea.

We have spatial information on the ionized gas outflow in a single galaxy–J2118+0017, nicknamed Makani (*wind* in Hawaiian). In its nuclear spectrum, Makani shows Mg II purely in emission, but Fe II λ2586 in absorption, with $V_{\rm max}\sim1000$ km s^{-1}. It is otherwise a very typical galaxy in our sample. Makani was observed with the Keck Cosmic Web Imager (KCWI; Morrissey et al. 2018), and found to exhibit impressive outflow shells in [O II] emission, spanning 100 kpc (Rupke et al. 2019). Makani has two distinct outflows: one young and fast, one older and slower, flowing along orthogonal axes from one another. This implies that winds are emerging from different regions of the galaxy at different times during the merger process. While Makani has material outflowing in multiple directions, it is uncertain whether this is true for all of our targets; additional KCWI observations are underway.

In the absence of galaxy selection effects, the detection rate should be equal to the global covering factor of the wind, implying near-spherical outflows for the HizEA galaxies. However, the high occurrence of outflows in the sample may suffer from some selection bias. The targets were not intentionally selected from the SDSS for their Mg II absorption because we wished to study its incidence. (In addition, the SDSS spectra used for target selection were generally too noisy in the blue region to reliably measure Mg II.) However, there may have been some unintended photometric selection biases. Galaxies with comparable masses and SFRs to the HizEA sample are typically highly dust obscured, and consequently not blue or bright enough to satisfy the HizEA photometric target selection criteria (ours as well as that of SDSS quasar target selection—see Section 2.1). Therefore, our magnitude and color cuts may have favored galaxies where a massive outflow had blown a hole in the ISM, causing the galaxy to appear brighter and bluer. Large samples at $z\sim0.5$ selected from far-IR or submillimeter data will be needed to explore this question further.

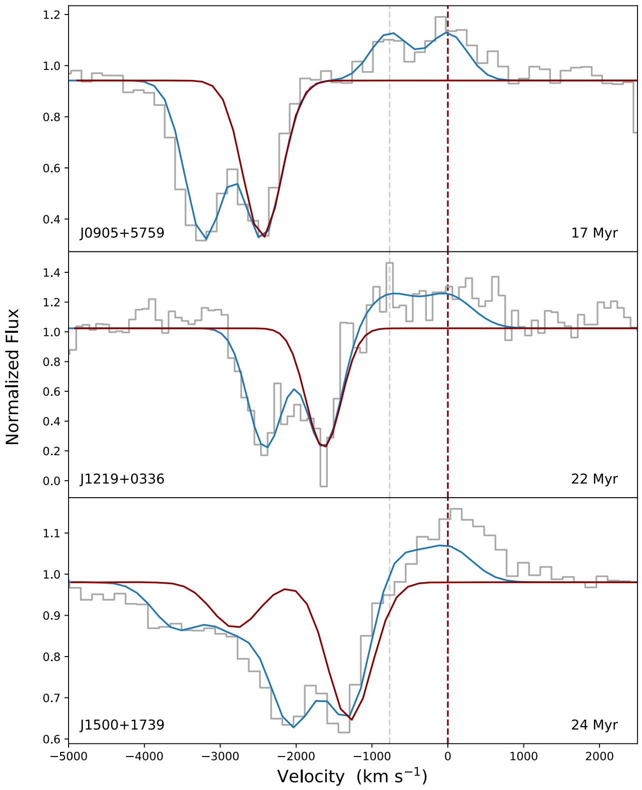

Figure 8. Examples of Mg II absorption profiles with no apparent zero-velocity absorption. The data is shown in gray, and the fit is in blue. The velocity shown on the *x*-axis is calculated using the 2803 Å component of the doublet. Zero velocity of the 2803 Å component is indicated with the red dotted line, while zero velocity of the 2796 Å component is indicated with a gray dotted line. We use the 2803 Å line (shown in red) to better demonstrate the lack of zero-velocity gas, given that blending often occurs for doublets. The light-weighted stellar age is indicated in the bottom right corner of each panel.

7.2. Formation and Evolution of Outflowing Cold Gas

One interesting feature in this sample (first noted in Perrotta et al. 2021) is the lack of absorption at the systemic velocity of several of our targets. For some of our most extreme targets, the Mg II absorption is so significantly blueward of the systemic velocity defined by the starlight that there appears to be no zero-velocity absorption. Three examples of this phenomenon are shown in Figure 8. Note while there is Mg II *emission* near near zero velocity, this could be due to high-velocity gas moving perpendicular to the line of sight. Gas seen in absorption is less subject to projection effects because absorption only probes gas directly between the observer and the starburst. Roughly 6 of our 46 targets show this pronounced lack of absorption near zero velocity. These galaxies have light-weighted ages between 10 and 50 Myr, placing them among the youngest third of the sample. This phenomena could plausibly be explained by cold gas condensing directly out of the fast-moving hot wind rather than being entrained and gradually accelerated.

Much debate exists over the origin and formation of cold gas in galaxy halos and outflows (e.g., Veilleux et al. 2005; Scannapieco & Brüggen 2015; Zhang et al. 2015). However, some analytical models and simulations have found that supernova feedback and radiative cooling are critical to producing cool gas in the galaxy halo that can be traced by low-ionization absorption lines (Hopkins et al. 2012; Suarez et al. 2016; Biernacki & Teyssier 2018; Turner et al. 2017; Lochhaas et al. 2018; Qiu et al. 2021). Suarez et al. (2016) find that, for many cases with radiative-cooling, they were able to form rapidly outflowing cool gas from in situ cooling of the hot flow. They show that the amount of cool gas formed depends strongly on the “burstiness” of energy injection; sharper, stronger bursts typically lead to a larger fraction of cool gas forming in the outflow. Our targets exhibit this type of “bursty” behavior—visible in the SFHs, the multiple velocity components of the Mg II absorption profiles, and in the aforementioned shells of [O II] emission observed in Makani (Rupke et al. 2019). Given that our targets’ outflows likely formed through highly impulsive bursts, the formation of cold gas at extreme velocities is consistent with the phenomenon seen in simulations.

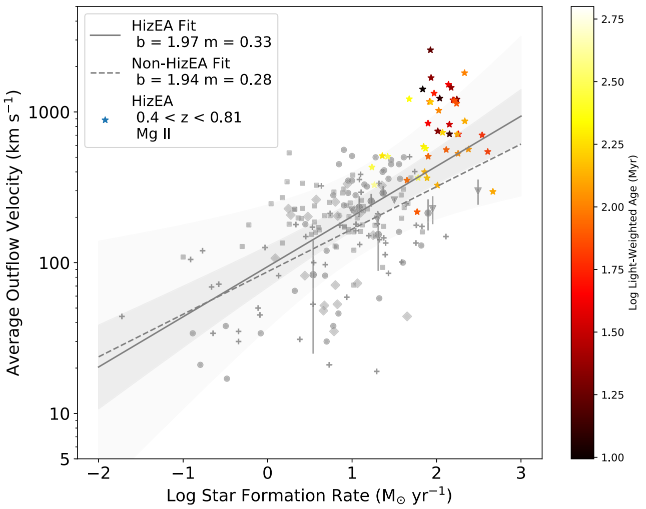

Figure 9. Average outflow velocity vs. SFR with the HizEA galaxies color-coded according to the light-weighted age of their stellar populations younger than 1 Gyr (Section 4.1.1). The galaxies with the youngest stellar ages (the ongoing starbursts) have some of the highest velocities and are some of the largest outliers from the reference sample drawn from the literature (gray points). Thus, limiting the HizEA sample to only those galaxies at or near their burst peak would not minimize the scatter in the scaling relations.

The burst-like nature of our sample may also be a key to understanding how outflows evolve over time. Whether outflows speed up over time due to additional momentum injection or slow down as they plow through the circumgalactic medium is another matter still under debate. When examining the light-weighted stellar ages in this sample, it is apparent that outflow velocity may have a correlation with age. As seen in Figure 9, the most extreme outflow velocities tend to be some of the youngest bursts, implying that these outflows are slowing down over time. This will be examined further in J. Davis et al. (2023, in preparation).

7.3. The Extreme Outflow Velocities of the HizEA Galaxies

The outflow velocities of many of the HizEA galaxies are unprecedented for star-forming galaxies. In our reference sample of 296 individual galaxies (Section 5), the largest $V_{\rm avg}$ value is 560 km s^{-1} (Heckman et al. 2015), and the largest $V_{\rm max}$ value is 1500 km s^{-1} (Heckman & Borthakur 2016).[13] In our HizEA sample, 28/43 galaxies with measured outflows (65%) have $V_{\rm avg} > 560$ km s^{-1}, and 18/43 (42%) have

---

[13] Heckman & Borthakur (2016) include 9 HizEA galaxies from our previous works in their sample. We have not included those in our comparison.

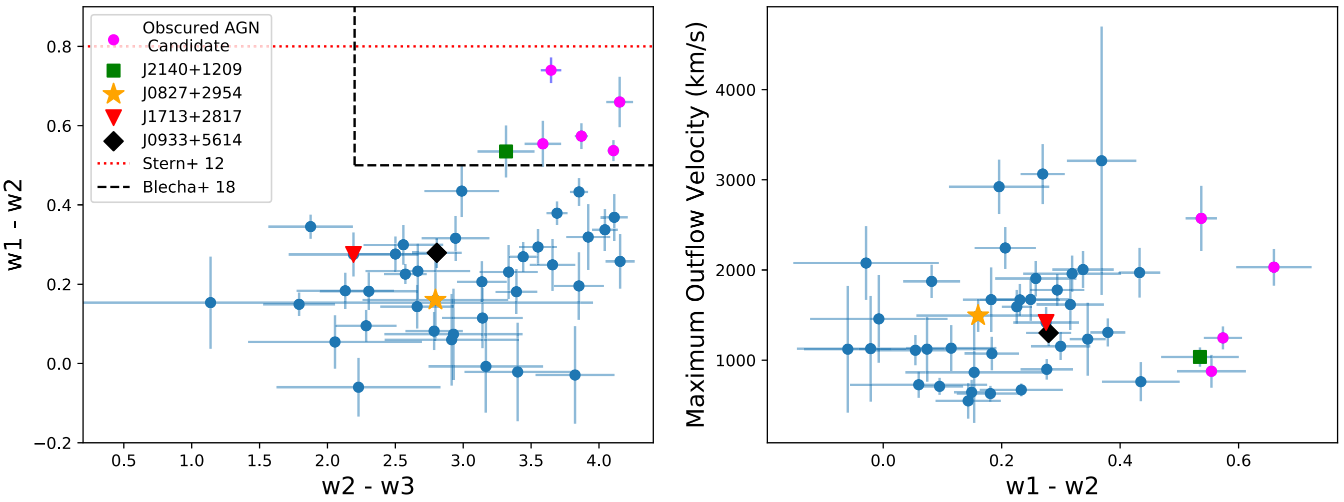

Figure 10. AGN mid-IR indicators using WISE photometry bands W1, W2, and W3. The left panel shows a color–color plot for the HizEA sample, along with the Stern et al. (2012) mid-IR cutoff (red dotted line, where AGN are those with W1–W2 values > 0.8) and the Blecha et al. (2018) criteria (black dashed line, where objects inside the bounding box are AGN-like). The right panel displays maximum outflow velocity vs. W1–W2. Galaxies hosting AGN (Section 2.3) are listed in the left panel legend. J2140+1209 is a Type I AGN; J0827+2954 and J0933+5614 are radio galaxies; and J1713+2817 is a BPT-identified Type II AGN. Notably, the AGN do not have exceptional outflow velocities.

$V_{\max} > 1500$ km s^{-1}. Below we consider the potential origin of these high velocities.

7.3.1. Are AGN the Cause of the Fast Outflows?

The HizEA galaxies are massive ($\log M_*/M_\odot = 10.3$–11.5), and it is likely that that they harbor supermassive black holes, which may have been fueled during the merger event. Therefore, it is important to consider whether AGN feedback may play a role in driving these fast outflows. In Section 2.3, we summarized the available X-ray, optical, infrared, and radio evidence for AGN activity. We identified one Type I AGN, one Type II AGN, two radio galaxies, and 5 candidate-obscured AGN in our sample of 45 galaxies. In Figure 10, we show the position of the HizEA galaxies in a WISE color–color diagram used to select AGN. None of the galaxies fall in the AGN region defined by Stern et al. (2012), but 5 galaxies (as well as the Type I AGN J2140+1209) fall in the AGN region defined by Blecha et al. (2018) based on galaxy merger simulations. The objects above the Blecha AGN line but below the Stern line are thought to have <50% of their bolometric luminosity associated with AGNs (Blecha et al. 2018).

Using W1–W2 color as a proxy for an increasing contribution from AGN activity, we examine whether outflow velocity correlates with AGN activity in Figure 10. The most AGN-like galaxies (those with the reddest W1–W2 colors) do not show the highest outflow velocities in the sample. The 4 confirmed AGNs have velocities at or below the sample mean; the 4 candidate-obscured AGNs with W1–W2 = 0.5–0.8 have a wide range of velocities. (The fifth does not show Mg II absorption.) We conclude that ongoing AGN activity is unlikely to be responsible for the large outflow velocities observed in the HizEA sample.

7.3.2. Are Galaxy Mergers the Cause of the Fast Outflows?

The HizEA galaxies observed with HST are all late-stage mergers with compact central starbursts (Diamond-Stanic et al. 2012; Sell et al. 2014; Diamond-Stanic et al. 2021). However, the reference sample also includes a large number of mergers and disturbed galaxies. The Heckman et al. (2015), Heckman & Borthakur (2016) samples contain a large number of local "Lyman Break Analogs," which have been shown to be mergers (Overzier et al. 2008). In Chisholm et al. (2015), nearly all the galaxies with SFR > 10 $M_\odot$ yr^{-1} are mergers or compact galaxies. They find marginal evidence that mergers have 0.12 dex higher outflow velocities, but their sample lacks a sufficient number of normal spirals to carry out this comparison robustly. In Rubin et al. (2014), galaxies classed as "disturbed" have similar outflow velocities to those classed as spirals.

Therefore, the most fundamental and direct cause for the high velocities in the the HizEA galaxies does not seem to be galaxy mergers. More relevant is the fact that the mergers in the HizEA galaxies induced extremely compact central starbursts. Notably, the galaxies with the highest velocity outflows in the reference sample are the LBAs, which were explicitly selected to have compact UV morphologies (Heckman et al. 2005).

7.4. Do the HizEA Galaxies Belong on the Outflow Scaling Relations?

The HizEA galaxies complement our sample drawn from the literature by enabling us to explore outflow scaling relations over a broader dynamic range of galaxy physical properties (e.g., higher SFR, $\Sigma_{\rm SFR}$, and sSFR). However, the HizEA galaxies are outliers on many of the scaling relations (Figure 6, 7), and therefore it is worth considering if it is indeed appropriate to include them when measuring the correlation coefficients and the slopes of the relations (Table 2).

One salient way in which the HizEA sample differs from the reference sample is that many of the galaxies are a few 10's to 100's of Myr post-burst. However, as we show in Figure 9 (and explore in J. Davis et al. 2023, in preparation), the galaxies with the youngest stellar ages (the ongoing starbursts) have the some of the highest velocities and are some of the largest outliers from the literature sample. Thus, limiting the HizEA sample to only those galaxies at or near their burst peak would not minimize the scatter in the relations.

A related question is whether galaxies with comparably high SFRs but lower outflow velocities than the HizEA sample are missing from the scaling relations. Most galaxies with SFR $>100\ M_\odot\ \mathrm{yr}^{-1}$ are highly dust-obscured (Bothwell et al. 2011; Rujopakarn et al. 2010), and would not have been selected by SDSS quasar target selection. The fainter rest-frame near-UV fluxes of dusty galaxies would also make them less favorable candidates for follow-up spectroscopy in most surveys. Dusty galaxies could potentially represent an earlier evolutionary phase, before strong outflows have developed, or they could represent disk galaxies viewed closer to edge-on where the projection effects might reduce the observed outflow velocities.

Banerji et al. (2011) measured Mg II outflows in composite spectra made from submillimeter galaxies (SMGs) and submillimeter-faint radio galaxies at $z\sim1.3$. These dusty galaxies show similar SFRs (60–440 $M_\odot\ \mathrm{yr}^{-1}$) to the HizEA galaxies, but have outflows velocities 2.5 times smaller on average. When plotted on the Σ_{SFR} relations however, we find that, despite high SFRs, the larger size of these galaxies places them in an unremarkable location among the rest of our reference sample at lower values of Σ_{SFR} (see Figures 6(c), (d)). This provides anecdotal support for the primacy of Σ_{SFR} as the most important scaling relation for predicting outflow velocities; however, further follow-up of the obscured population is needed to obtain a complete picture of outflow scaling relations.

In summary, we see no compelling reasons to exclude the HizEA galaxies from the outflow scaling relations. The parameters of our linear fits to the relations combining the HizEA sample and 10 samples drawn from the literature are reported in Table 2. Rupke (2018) surveyed the recent literature on outflow scaling relations and recorded the median slope and 1σ spread of seven different samples (five of which are not included in our reference sample). We record the Rupke (2018) median slopes (m_{comp}) in Table 2 for comparison. In general, our measured slopes agree with those reported by Rupke (2018) for V_{avg} and V_{max}.

7.5. The Origin of Outflow Scaling Relations: Comparisons with Analytic Models

With the statistical power and dynamic range of our combined sample of ∼350 galaxies, we find significant correlation of both average and maximum velocity with SFR and Σ_{SFR}. The correlations for M_* and sSFR are weaker, with ρ, $R \lesssim 0.5$ and FVU $\gtrsim$0.9. These trends are very similar to those found by Heckman et al. (2015), Heckman & Borthakur (2016) with a sample of ∼40 galaxies. In our combined sample, V_{avg} and V_{max} appear equally well correlated with galaxy physical properties; however, we caution that there are substantial differences in the reference samples because only a few surveys report both V_{max} and V_{avg}. Thus, it is premature to draw a firm conclusion.

Since outflow scaling relations were first discovered (Martin 2005; Rupke et al. 2005), their origin has been a matter of debate. There are many different physical processes that contribute to driving cool gaseous outflows: cool clouds may be accelerated by the ram pressure of supernova ejecta and shocked stellar winds, by radiation pressure acting on dust grains, or by cosmic rays interacting with the outflow's magnetic field (see Heckman & Thompson 2017; Zhang 2018). Indeed, different processes are likely to become important in different galactic conditions (Hopkins et al. 2012).

In the classical picture of a starburst-driven superwind (Chevalier & Clegg 1985), hot (10^7–10^8 K) overpressured supernova ejecta in the central starburst expands, sweeps up, and entrains the cool ambient ISM. The velocity of this hot wind fluid as it leaves the starburst region is expected to be $V_{\mathrm{hot}} = (2\dot{E}/\dot{M})^{1/2}$, where $\dot{E}$ is the energy injection rate, and $\dot{M}$ is the mass outflow rate. Both $\dot{E}$ and $\dot{M}$ are proportional to the SFR, and therefore it cancels out of the expression for the outflow velocity, yielding $V_{\mathrm{hot}} \sim 1000\ \mathrm{km\ s^{-1}}\ (\alpha/\beta)^{1/2}$ where α is the supernova thermalization efficiency factor (e.g., the fraction of supernova energy that goes into heating the gas and driving the wind), and β is the mass-loading factor (the ratio of the mass in the wind to the mass of pure supernova ejecta). The key point is that the velocity of the hot wind, at least initially, does not explicitly depend on the host galaxy properties (see Tanner et al. 2017). The hot wind velocity represents the terminal velocity that cool clouds could be accelerated to via ram pressure. So why do outflows traced by the *cool* ionized gas depend on SFR and Σ_{SFR}? We outline a few ideas from the literature below.

One idea is that V_{hot} is independent of SFR, but only the galaxies with the highest SFRs have *cool* outflows that reach the terminal velocity of the hot wind. Notably, the *acceleration* of cold clouds via ram pressure does not depend on the hot wind's velocity, but rather it is momentum flux, which scales as $\dot{P} = \dot{M}V_{\mathrm{hot}} \simeq (2\dot{E}\dot{M})^{1/2} \propto \mathrm{SFR}$ (Tanner et al. 2017). A denser hot wind that delivers more momentum per unit area will be able to accelerate a cool cloud to the hot wind's velocity more quickly. A higher radiation flux or cosmic ray flux per unit area will have a similar effect. Heckman et al. (2015) used a simple analytical model to explore the combined effect of the outward force imparted by the starburst's momentum and the inward force of gravity on an idealized cool cloud. Because the momentum flux falls off more quickly with distance than the gravitational force (due to the extended dark halo), clouds reach a maximum velocity at the radius where the two forces are balanced. The galaxies with lower values of SFR accelerate their cold clouds more slowly and reach maximum velocities that are well below the terminal velocity of the hot wind, resulting in a relation $V_{\mathrm{max}} \propto (\mathrm{SFR}/R_*)^{0.5}$, which is somewhat steeper than we observe ($V_{\mathrm{max}} \propto (\mathrm{SFR}/R_*)^{0.25\pm0.05}$; Table 2).

Alternatively, it may be that the mass-loading factor of the hot wind, β_{hot}, has a built-in dependence on the SFR. (Recall $V_{\mathrm{hot}} \propto \beta^{-1/2}$.) In this case, either the cool clouds could be accelerated to V_{hot} or the hot gas could undergo fast radiative cooling on large scales, producing a population of cool clouds moving at V_{hot} (Wang 1995; Martin et al. 2012). Thompson et al. (2016) developed a simple analytic model that predicts the radius and velocity of a shell-like cool outflow that forms from bulk cooling of the mass-loaded hot wind. They showed that there is a minimum β required for cool outflows to form at large radius, and this value depends upon SFR/R_*, where R_* is the radius of the starburst region. This yields a maximum wind velocity that scales as $V_{\mathrm{max}} = 665\ (\mathrm{SFR}/R)^{0.180}\ \mathrm{km\ s^{-1}}$, adopting their fiducial parameters. In addition to a maximum velocity, they also calculate the outflow velocity expected if fast radiative cooling of the hot wind occurs immediately outside of the star-forming region: $V_{\mathrm{crit}} = 449\ (\mathrm{SFR}/R)^{0.135}\ \mathrm{km\ s^{-1}}$. This defines the minimum velocity that the cool gas could have if it formed from the hot wind fluid via radiative cooling. We compare Thompson's V_{crit} to our measured V_{avg} as a function of SFR/R in Figure 11(a). The model sits above most of the literature data, but below a substantial fraction of the HizEA galaxies. In Figure 11(b), we compare Thompson's predicted V_{max}–SFR/R

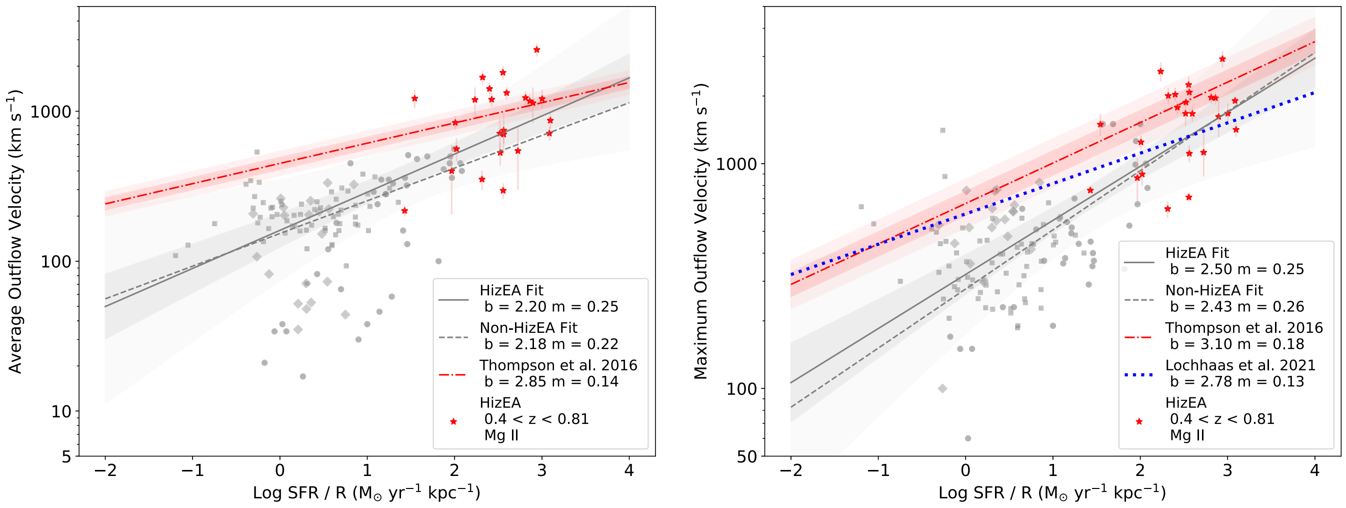

(a) (b)

Figure 11. Scaling relations for outflow velocity vs. star formation rate divided by the galaxy radius. Several theoretical works suggest that outflow velocity should be proportional to SFR/R (Section 7.5). The HizEA galaxies are shown in red, and the comparison sample is shown in gray scale. The plot symbol shapes are the same as those shown in Figures 6 and 7. We compare the data to the analytic models of Thompson et al. (2016) for an initially adiabatic hot outflow that has undergone bulk radiative cooling. The dashed line represents a model with $\alpha = 1$, a hot wind metallicity equal to the solar value, and an outflow that subtends 4π steradians (see Thompson's Equations (13) and (14)). The darker red shaded region illustrates the effect of varying one of these parameters by a factor of 2, and the lighter red region a factor of 4. In panel (a), we show Thompson's critical (minimum) outflow velocity compared with $V_{\rm avg}$. In panel (b), we show Thompson's maximum outflow velocity compared with the measured $V_{\rm max}$. The blue dotted line shows the expected relation from the analytical models of Lochhaas et al. (2021) adopting their fiducial parameters ($\alpha = 0.9$, a fully ionized gas) and assuming that the wind reaches its maximum momentum ($\beta = \beta_{\rm crit}$). The Lochhaas and Thompson models provide a reasonably good fit the HizEA galaxies, but they predict velocities that are too fast for the majority of the comparison sample. This implies that the cool gas in the HizEA galaxies may be condensing directly from the hot wind (as predicted by these models), while this process is less common in galaxies with lower SFR/R. See Section 7.5.

relation to the observations. The model lies along the upper envelope of the data, consistent with the notion that it defines the maximum velocity that the winds can have if they undergo bulk radiative cooling. Similar results were found by Xu et al. (2022) using the CLASSY sample of local UV-bright galaxies. Overall, the data-model comparison suggests that galaxies with SFR/R $\lesssim 100\, M_{\rm Sun}\, {\rm kpc}^{-1}$ have cool outflows moving at velocities that are too low to be explained by gas cooling from the hot wind fluid. Many of the HizEA galaxies, on the other hand, have velocities that are bracketed by the minimum and maximum values predicted by the Thompson et al. (2016) model. Thus, bulk cooling of the hot wind may be a viable method of producing cool gas in ultra-compact starbursts like the HizEA galaxies. This is supported by the lack of absorption near the systemic velocity for some HizEA galaxies (Section 7.2), which suggests the cool gas is born fast, rather than being entrained in the disk and gradually accelerated.

Lochhaas et al. (2021) expand upon the Thompson et al. (2016) models and suggest that there is a maximum value of $\beta_{\rm hot}$ that a wind can attain before it becomes so dense that radiative cooling takes place within the wind driving region (i.e., at the center of the starburst). This cooling sets a maximum on the total outflow momentum for hot energy-driven winds, which also applies to the cool ionized outflows they accelerate. The predicted scaling of $\beta_{\rm crit}$ with SFR/R results in a minimum predicted outflow velocity of $V_{\rm min} = 598\,({\rm SFR}/R_{*})^{0.135}$ km s^{-1} where R_* is the radius of the star-forming region. (We have assumed their fiducial values of a fully ionized wind with $\alpha = 0.9$.) They posit a maximum outflow velocity very similar to that of Thompson et al. (2016). Therefore, the expectation is that the data in Figure 11(b) should lie above the blue dotted line from Lochhaas et al. (2021) and below the dashed red line of Thompson et al. (2016). Most of our collected sample from the literature sits below the Lochhaas et al. (2021) relation (blue line), suggesting that these models may not be applicable to most galaxies. Notably, a large fraction of the HizEA sample sits in between the blue and red lines. A possible interpretation is that these intense starbursts are clustered near the maximum allowable momentum for thermally driven winds, perhaps more so than the other samples from the literature at lower SFR/R. The HizEA targets may be probing the edge of a self-regulation mechanism: if the winds were any more powerful, the interior of the starburst would start cooling, which would inhibit the wind and dampen its power.

It is unlikely that the idealized scenarios described above capture all the relevant physics. High-resolution simulations of individual cool clouds embedded in a hot wind show that hydrodynamical instabilities at the wind–cloud interface can cause the cloud to be rapidly destroyed (see Zhang et al. 2017). Alternatively, under the right conditions, cold clouds can grow due to rapid cooling in their turbulent radiative mixing layers (see Gronke & Oh 2018). Fielding & Bryan (2022) note that cooling is more effective at high density, and therefore galaxies with a higher hot wind density (higher $\Sigma_{\rm SFR}$) will tend to grow their cool clouds and more rapidly accelerate them to velocities comparable to the hot wind. Conversely, galaxies with low density hot winds (low $\Sigma_{\rm SFR}$) will oblate their cool clouds before they can be significantly accelerated.

Clearly, the origin of the outflow scaling relations is complicated, and it is likely that many of the different physical processes mentioned above come into play. Nonetheless, SFR/R stands out as a key parameter from theoretical works. This is broadly supported by our observational data. The Spearman rank order correlation coefficients for the V–SFR, V–SFR/R, and V–$\Sigma_{\rm SFR}$ relations are very similar. However, the Pearson

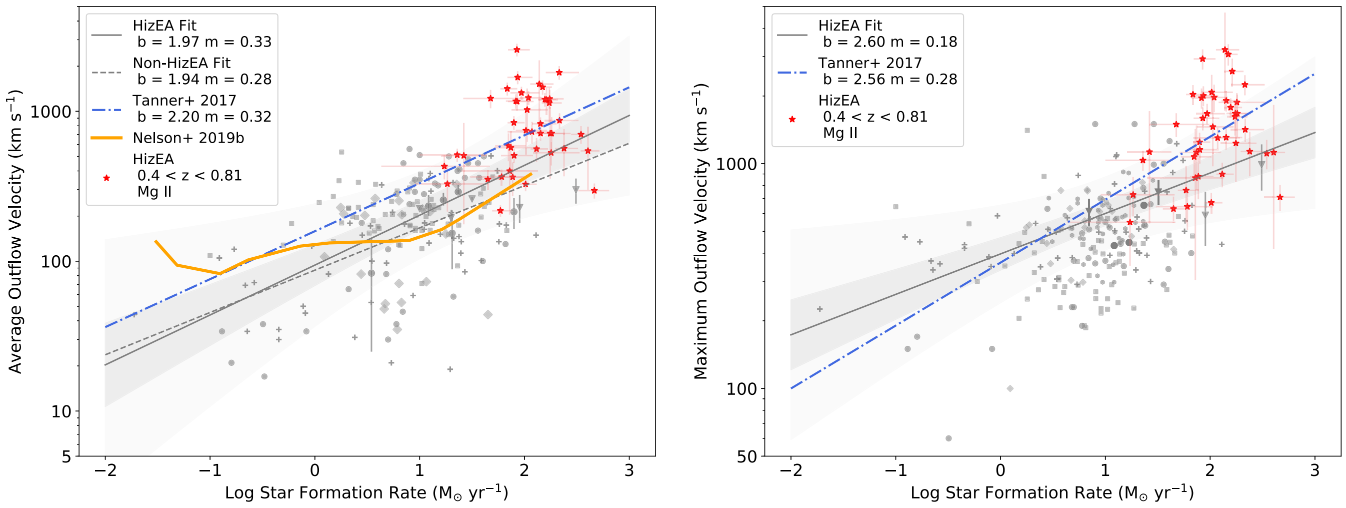

(a) (b)

Figure 12. Comparison of observational scaling relations to those found in theoretical models. Left: average outflow velocity vs. SFR, with the theoretical relation found by Tanner et al. (2017) for Si II using hydrodynamical simulations of M82-like starbursts (dashed–dotted blue line) and the relation found by Nelson et al. (2019) for the TNG50 cosmological simulations (solid orange line). Right: maximum outflow velocity vs. SFR, with the relation from Tanner et al. (2017; dashed–dotted blue line). The red stars represent the HizEA galaxies while the gray points are data from the literature. The gray lines denote the fit to the observational data.

linear correlation coefficient is higher, and the scatter (FVU) is smaller for the V–SFR$/R$ and V–$\Sigma_{\rm SFR}$ trends (see Table 2). The outflow scaling relations with M_* and sSFR may be secondary trends, resulting from SFR–M_* and M_*–R correlations. As observational samples improve in quantity, uniformity, and parameter space coverage, we anticipate that the primacy of scaling relations involving both SFR and radius will become more evident.

7.6. Comparison with Numerical Models

Scaling relations provide a crucial benchmark against which simulations may measure the accuracy of their subgrid models. By increasing the dynamic range of the empirical outflow scaling relations, our work enables simulations to test their feedback prescriptions across a wider distribution of galaxy masses, sizes, and SFRs. However, with our low-resolution spectral data, we cannot comment on mass-loading and momentum flux implications for simulations as some previous works have done (e.g., Rubin et al. 2014; Heckman et al. 2015; Chisholm et al. 2017; Xu et al. 2022). We note that simulations often consider 3D outflows, while we are limited to line-of-sight velocities. This likely increases the scatter in the observational data and may produce some of the vertical offsets between observed and simulated trend lines.

We first compare our $V_{\rm avg}$ versus SFR relation to the hydrodynamical simulations of Tanner et al. (2017), Nelson et al. (2019) in Figure 12(a). In Tanner et al. (2017), the authors use a static mesh refinement version of the Athena code (Stone et al. 2008). They simulate a nuclear starburst inside a box 1000 pc on a side, with the stellar gravitational potential and associated parameters set to correspond to an M82-sized galaxy with models run for 1.5 Myr. The free parameters of their model are the SFR and the mass-loading parameter, β, which sets the maximum hot wind velocity, and the size of the spheroidal starburst region where they inject thermal energy. To measure the outflow velocity in a manner comparable to observations, they generate synthetic absorption line profiles for various silicon ions assuming that collisional ionization equilibrium governs the ionization fraction in each cell. From the synthetic profiles, they produce $V_{\rm cen}$, the velocity at half of the FWHM, and V_{90}, the velocity on the blueward side of the line where the absorption profile returns to 90% of full intensity. This approach is a close analog to our Mg II measurements. Tanner et al. (2017) fit power laws to the scaling relation for each silicon ion. In Figure 12, we compare to their relation for Si II as it is closest in ionization energy to Mg II. For the $V_{\rm avg}$ versus SFR relation, their fit (blue dashed–dotted line) has a nearly identical slope to the observational sample, but is offset higher by 0.23 dex. This could be due to their assumption of collisional ionization. Chisholm et al. (2016) demonstrate that photoionization is likely the dominant process governing the observed line ratios in outflows. It is also worth noting that these are isolated galaxy simulations in a small (1 kpc) box, so a large-scale complex circumgalactic medium (CGM) is absent.

In Nelson et al. (2019), they use TNG50, the latest simulation from the IllustrisTNG project (Nelson et al. 2019), to explore outflow scaling relations. TNG50 is the smallest IllustrisTNG volume, focused on high numerical resolution that enables study of the connection between small-scale (i.e., few hundred parsecs) feedback and large-scale (i.e., few hundred kiloparsecs) outflows. The simulation includes both star formation and AGN feedback. The TNG galactic-scale outflows generated by stellar feedback are modeled using a kinetic wind approach. This uses available supernova energy to stochastically eject star-forming gas cells from galaxies at an injection velocity proportional to the local dark matter velocity dispersion. To measure outflow velocities from TNG50, they reduce the complex distribution of outflow velocities around a galaxy down to a single $V_{\rm out}$. This is accomplished by taking mass-outflow-rate-weighted percentiles of 3D radial velocities. In particular, they define the quantity $V_{{\rm out},N}$ as the radial velocity above which (1–N) percent of the outflow is moving. For example, $V_{\rm out,90} = 500\,{\rm km\,s^{-1}}$ implies that 10% of the outflowing mass flux is moving $500\,{\rm km\,s^{-1}}$ or faster. This velocity measurement is not strictly analogous to our line profile method, but the comparison is still instructive. In Figure 12(a), we compare the Nelson et al. (2019) $V_{\rm out,50}$–SFR

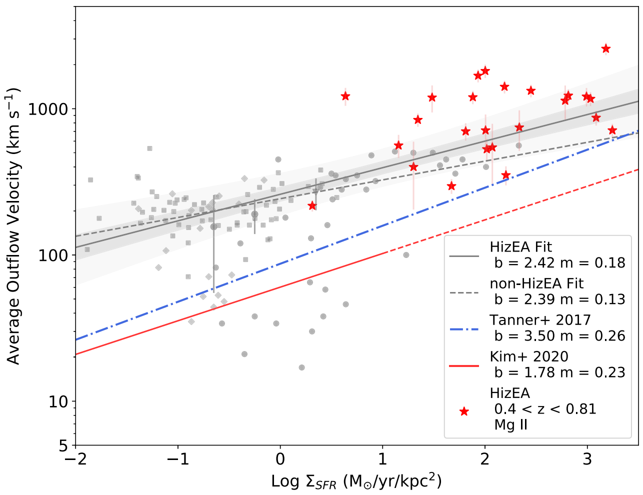

Figure 13. Comparison of the relation between average outflow velocity and $\Sigma_{\rm SFR}$ in observations and numerical simulations. The relation found in the Tanner et al. (2017) isolated galaxy hydrodynamical simulations is overplotted as a dashed–dotted blue line. The scaling relation found in the SMAUG high-resolution ISM patch simulations (Kim et al. 2020) is shown in red with the solid line denoting the $\Sigma_{\rm SFR}$ range covered by the simulations and the dashed line indicating an extrapolation of the fit. The red stars represent the HizEA galaxies while the gray points are data from the literature. The gray lines denote the fit to the observational data.

relation against the observed $V_{\rm avg}$–SFR relation. The fit to the TNG data (orange solid line) falls within the envelope of the observational data but is above the median of the data at SFR $\lesssim 3\ M_\odot\ {\rm yr}^{-1}$ and below it at higher SFR. The simulation does not reach the high velocities of the HizEA galaxies (even though it includes AGN feedback), in part, because it lacks sufficient volume to probe rare galaxies with SFR $>100\ M_\odot\ {\rm yr}^{-1}$.

In panel (b) of Figure 12, we compare our maximum outflow velocity versus SFR relation to the aforementioned Tanner et al. (2017) models. The Tanner et al. (2017) V_{90} fit has a steeper slope than that of the observational $V_{\rm max}$ fit, but falls within the error bars.

One of our most compelling scaling relationships is between $V_{\rm avg}$ and $\Sigma_{\rm SFR}$. We compare our empirical fit to the fits derived by Tanner et al. (2017), Kim et al. (2020). The Tanner et al. (2017) trend line, obtained from the same simulation described above, is slightly steeper and with a lower intercept. Tanner et al. (2017) note that their method of determining $\Sigma_{\rm SFR}$ differs from observational approaches in that their value pertains only to the central starburst, while observers typically calculate $\Sigma_{\rm SFR}$ from the entire galaxy. They also find that the mix of galaxy types in an observational sample can have notable effects on the slope of the scaling relation. Samples with a mix of galaxies with different hot wind velocities had shallower slopes than those samples with uniform hot wind velocities (which corresponds to the situation probed in their $\Sigma_{\rm SFR}$ simulations).

Kim et al. (2020) present theoretical scaling relations of galactic outflows as part of the Simulating Multiscale Astrophysics to Understand Galaxies (SMAUG) project. They utilize a suite of parsec-resolution local galactic disk ("ISM patch") simulations run using the TIGRESS framework, which self-consistently models the ISM, star formation, radiative heating, and supernova feedback to drive outflows. They measure outflow velocity as a time-averaged value obtained by dividing the kinetic component of the momentum flux by the mass flux in vertical slices of their simulation. In Figure 13, we show their outflow velocity versus $\Sigma_{\rm SFR}$ relation as a solid red line (dashed line where the fit has been extrapolated). Of note is the relatively good agreement in the slope ($m_{\rm obs} = 0.18 \pm 0.03$; $m_{\rm SMAUG} = 0.23$). The SMAUG scaling relation falls 0.64 dex below our $V_{\rm avg}$ observations; however, the SMAUG velocities are not measured from synthetic line profiles. Additionally, the SMAUG simulations deal with galactic disks, against which it is difficult to compare our compact merger remnants.

Our sample and the resulting scaling relations highlight the need to probe higher SFR and $\Sigma_{\rm SFR}$ regimes in future simulations. Additionally, there is a strong need for more directly comparable theoretical quantities in the form of simulated absorption line profiles (see de la Cruz et al. 2020).

8. Summary and Conclusions

In this work, we explore the galactic winds in the HizEA galaxies, a sample of 46 massive, late-stage galaxy merger remnants that host compact central starbursts at redshifts of 0.4–0.8. The galaxies were selected from SDSS-I using emission and stellar absorption line criteria designed to select galaxies at an early stage of the star formation quenching process. We obtained high S/N spectra of the HizEA galaxies with MMT/Blue Channel, Magellan/MagE, and Keck/LRIS covering rest-frame ∼2500–5500 Å. With these spectra, we characterize their stellar populations and measure outflow velocities using the Mg II $\lambda\lambda$2796,2803 doublet.

We measure stellar masses and SFRs using `Prospector` to fit the galaxies' broadband SEDs and spectra, and we obtain $\Sigma_{\rm SFR}$ using HST/WFC imaging-derived half-light radii. The galaxies are massive ($\log M_* \sim 10.4$–11.5) and compact ($r_e \sim$ 100–1300 pc), with SFRs of 20–500 $M_\odot\ {\rm yr}^{-1}$ and $\Sigma_{\rm SFR}$ up to 1800 $M_\odot\ {\rm kpc}^2\ {\rm yr}^{-1}$. The galaxy SFHs are characterized by impulsive bursts of star formation, with bust ages ranging from 10–400 Myr.

After normalizing each spectrum by a model of the stellar continuum, we fit the Mg II lines with multiple Gaussian absorption components. We calculate an equivalent-width-weighted average ($V_{\rm avg}$) and maximum velocity ($V_{\rm max}$) corresponding to the 50th and 95th percentile of the λ2796 absorption line profile. We compare this extreme sample to a set of ten starburst-driven outflow samples in the literature, carefully curated to match our sample in redshift, ionization potential of the absorber, and measurement technique. We construct scaling relations for an outflow velocity with various galaxy properties from the combination of our sample and the literature samples. Our findings are summarized below:

1. Outflows are detected in ∼90% of the HizEA sample—a rate slightly higher than that of other mergers in the literature. This implies large global covering factors for these outflows and near-spherical geometries rather than biconical geometries, but the possible selection effects prevent us from drawing a firm conclusion.
2. Several of the galaxies with recent bursts of star formation (light-weighted age <50 Myr) do not have any gas absorption from $V = 0$ to $-1000\ {\rm km\ s}^{-1}$. This may be evidence for cold gas condensing directly from the fast-moving hot wind rather than being entrained from the ISM and gradually accelerated.
3. The outflows measured for the HizEA sample are very fast, with $V_{\rm avg}$ between 220 and 2600 km s^{-1}, and $V_{\rm max}$ between 550 and 3200 km s^{-1}. In our entire collected non-AGN-dominated comparison sample from the literature, the highest $V_{\rm max}$ is 1500 km s^{-1}.

4. A multiwavelength analysis of the 46 HizEA galaxies demonstrates that 4 host AGN and an additional 5 are candidate AGN based on their mid-IR colors. These 9 galaxies do not drive unusually fast outflows when compared with the rest of the HizEA sample, and we conclude that the extreme outflow velocities of the HizEA galaxies are likely related to very compact starbursts induced by mergers.
5. We find a comparatively weak correlation between outflow velocity and stellar mass and an even weaker correlation with sSFR (SFR/M_*). In the latter case, the slope of the correlation is close to zero, and the scatter is above 1 dex (Table 2), strongly rejecting any significant relation between outflow velocity and sSFR.
6. Outflow velocity is most strongly correlated with SFR, SFR/R, and Σ_{SFR}. The Spearman rank order correlation coefficients are very similar for all three, but the Pearson linear correlation coefficients and the scatter about the best-fit relation suggest that SFR/R and Σ_{SFR} are the most significant trends (Table 2). This is in broad agreement with a variety of analytic outflow models (Section 7.5).
7. HizEA galaxies are outliers on plots of velocity versus SFR and M_*, but connect smoothly with the literature sample on V_{out}–Σ_{SFR} relations. This provides further evidence that the HizEA galaxies' exceptional outflow velocities are a consequence of their extreme star formation conditions rather than hidden black hole activity. It also highlights the important role Σ_{SFR} plays in determining the velocities of cool gas in galactic winds. More data at intermediate and high values of Σ_{SFR} are needed to further establish the strength of this relationship.
8. Recent simulations show broad agreement with the velocity scaling relations presented in this paper, but, in detail, there are some differences in the slopes of the relations and, in some cases, large (∼0.5 dex) zero-point offsets. To enable more accurate comparisons, future simulations should both explore higher SFR and Σ_{SFR} values and generate synthetic absorption line profiles to enable outflow velocities to be measured in a manner consistent with the observations.

The HizEA sample represents an extreme in the parameter space of starburst-driven galaxy outflows, allowing us to probe previously unexplored realms of outflow scaling relations. However, there is still much to understand with this sample. In J. Davis et al. (2023, in preparation), we explore the temporal evolution of outflows, taking advantage of the wide range of post-burst ages in the sample. To better understand outflow geometries, we are observing our sample with the KCWI. With this spatially resolved data, we can further disentangle the relationship between stellar age, outflow velocity, and outflow radius. This sample presents a unique opportunity to better understand the connection between galaxy outflows and the CGM.

Acknowledgments

We thank the referee, Tim Heckman, for his helpful comments. We acknowledge support from the National Science Foundation (NSF) under a collaborative grant (AST-1813299, 1813365, 1814233, 1813702, and 1814159). C.T. acknowledges support from the H.I. Romnes Faculty Fellowship. S.P. and A.L.C. acknowledge support from the Heising-Simons Foundation grant 2019-1659 and the Ingrid and Joseph W. Hibben endowed chair at University of California, San Diego.

Funding for the SDSS and SDSS-II has been provided by the Alfred P. Sloan Foundation, the Participating Institutions, the National Science Foundation, the U.S. Department of Energy, the National Aeronautics and Space Administration, the Japanese Monbukagakusho, the Max Planck Society, and the Higher Education Funding Council for England. The SDSS website is http://www.sdss.org/.

The SDSS is managed by the Astrophysical Research Consortium for the Participating Institutions. The Participating Institutions are the American Museum of Natural History, Astrophysical Institute Potsdam, University of Basel, University of Cambridge, Case Western Reserve University, University of Chicago, Drexel University, Fermilab, the Institute for Advanced Study, the Japan Participation Group, Johns Hopkins University, the Joint Institute for Nuclear Astrophysics, the Kavli Institute for Particle Astrophysics and Cosmology, the Korean Scientist Group, the Chinese Academy of Sciences (LAMOST), Los Alamos National Laboratory, the Max-Planck-Institute for Astronomy (MPIA), the Max-Planck-Institute for Astrophysics (MPA), New Mexico State University, Ohio State University, University of Pittsburgh, University of Portsmouth, Princeton University, the United States Naval Observatory, and the University of Washington.

Observations reported here were obtained at the MMT Observatory, a joint facility of the University of Arizona and the Smithsonian Institution.

Portions of the reference samples and some of our sample made use of W.M. Keck Observatory, which is operated as a scientific partnership among the California Institute of Technology, the University of California, and the National Aeronautics and Space Administration. The observatory was made possible by the generous financial support of the W.M. Keck Foundation.

J.D.D. would like to acknowledge the support and Python-related assistance of D. Gonzalez Casanova.

The authors additionally wish to recognize and acknowledge the cultural significance and traditional stewardship of the lands housing the observatories used in this work: SDSS at Apache Point Observatory on the traditional lands of the Mescalero Apache tribe; MMT at Mt. Hopkins on the traditional lands of the Tohono O'odham people; and the summit of Maunakea, sacred to the Kānaka 'Ōiwi indigenous Hawaiian community. We are most fortunate to have the opportunity to conduct observations from these mountains.

Facilities: Sloan, MMT (Blue Channel Spectrograph), Keck I (LRIS), Magellan Clay (MagE spectrograph).

Software: Astropy (Astropy Collaboration et al. 2013), Matplotlib (Hunter 2007), Goddard IDL Astronomy Users Library (Landsman 1993), pPXF (Cappellari & Emsellem 2004; Cappellari 2017), Prospector (Leja et al. 2019; Johnson et al. 2021), ISPEC2D (Moustakas & Kennicutt 2006), MASE (Bochanski et al. 2009), xIDL LowRedux at http:www.ucolick.org/~xavier/LowRedux/, lmfit (Newville et al. 2014).

Appendix A
HizEA Outflow Measurements

This appendix contains, in Figures A1–A6, plots of the unnormalized MMT/MaGE/LRIS spectra with continuum fits, the continuum-normalized spectra with the Mg II doublet

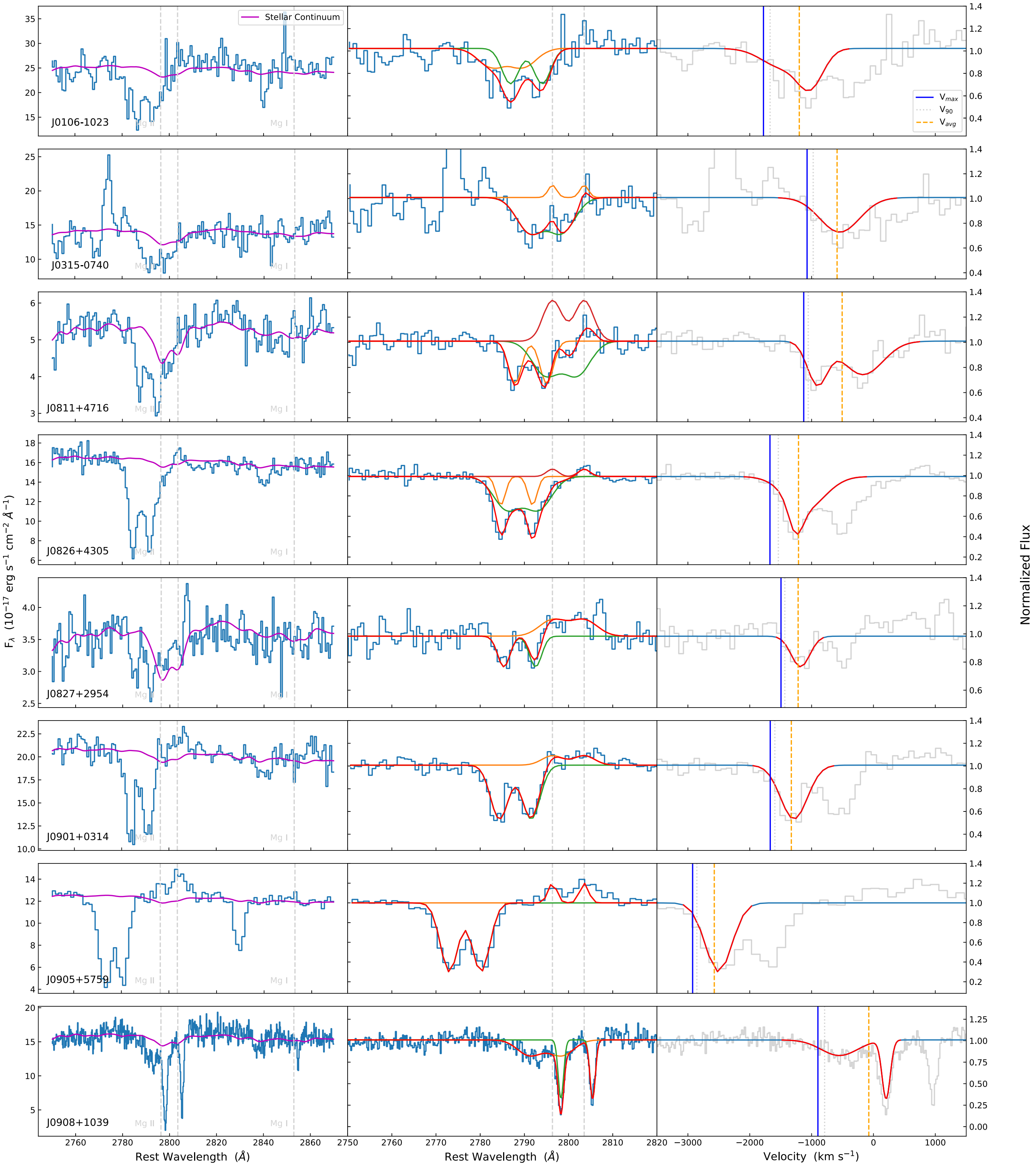

Figure A1. Left: unnormalized MMT/MaGE/LRIS spectra (blue) with continuum fit (magenta line). Rest positions of Mg I and Mg II doublet indicated with gray dotted lines. Center: continuum-normalized spectra with component (green, orange, purple) and composite profile (red) fits. Right: normalized spectra with composite spectra of only the 2796 Å component of the Mg II doublet (red) used to calculate equivalent widths and velocities. $V_{\rm avg}$ and $V_{\rm max}$ are indicated by the vertical orange and blue lines, respectively.

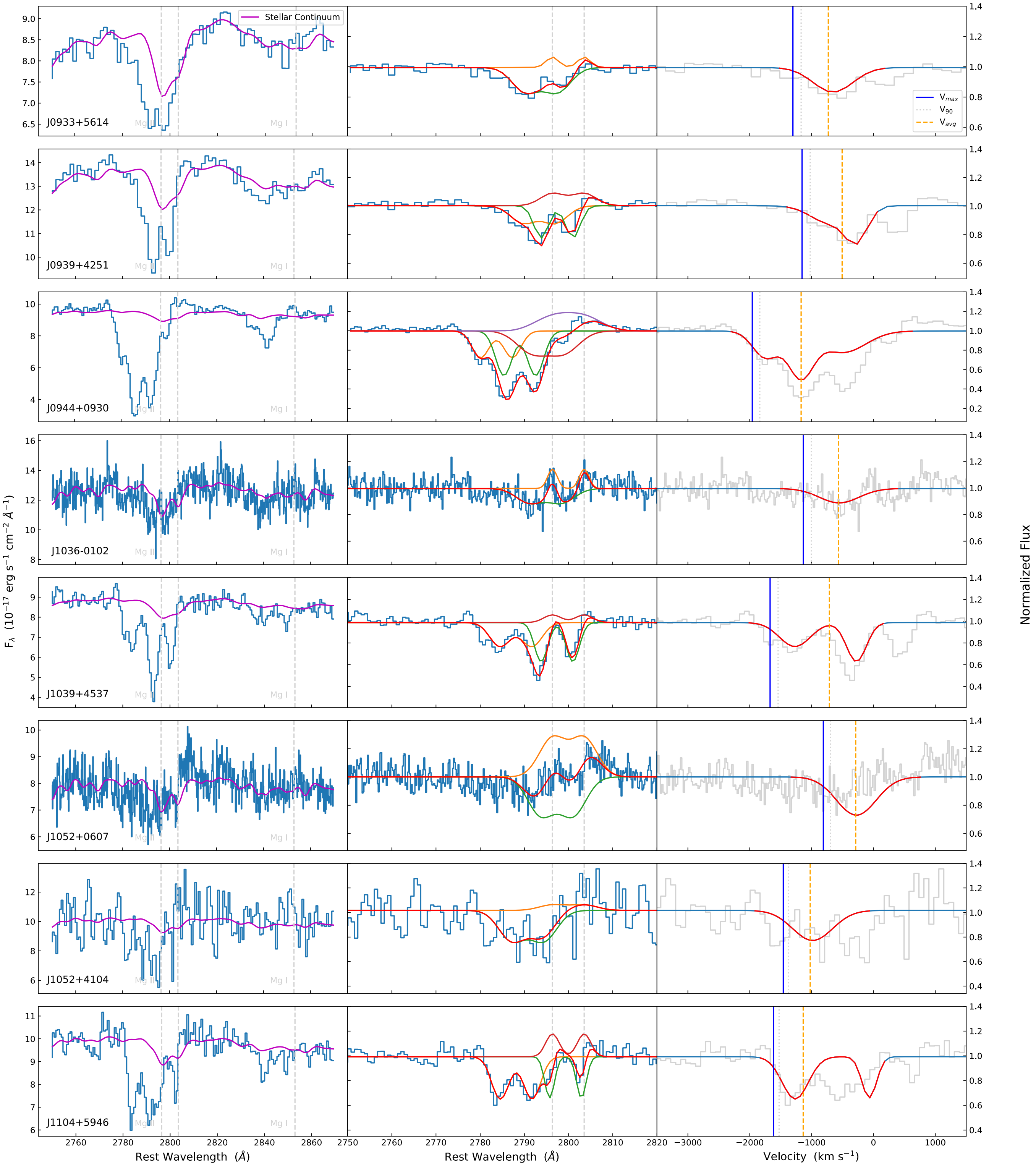

Figure A2. Left: unnormalized MMT/MaGE/LRIS spectra (blue) with the continuum fit (magenta line). Rest positions of Mg I and the Mg II doublet are indicated with gray dotted lines. Center: continuum-normalized spectra with component (green, orange, purple) and composite profile (red) fits. Right: normalized spectra with composite spectra of only the 2796 Å component of the Mg II doublet (red) used to calculate equivalent widths and velocities. V_{avg} and $V_{\max}$ are indicated by the vertical orange and blue lines, respectively.

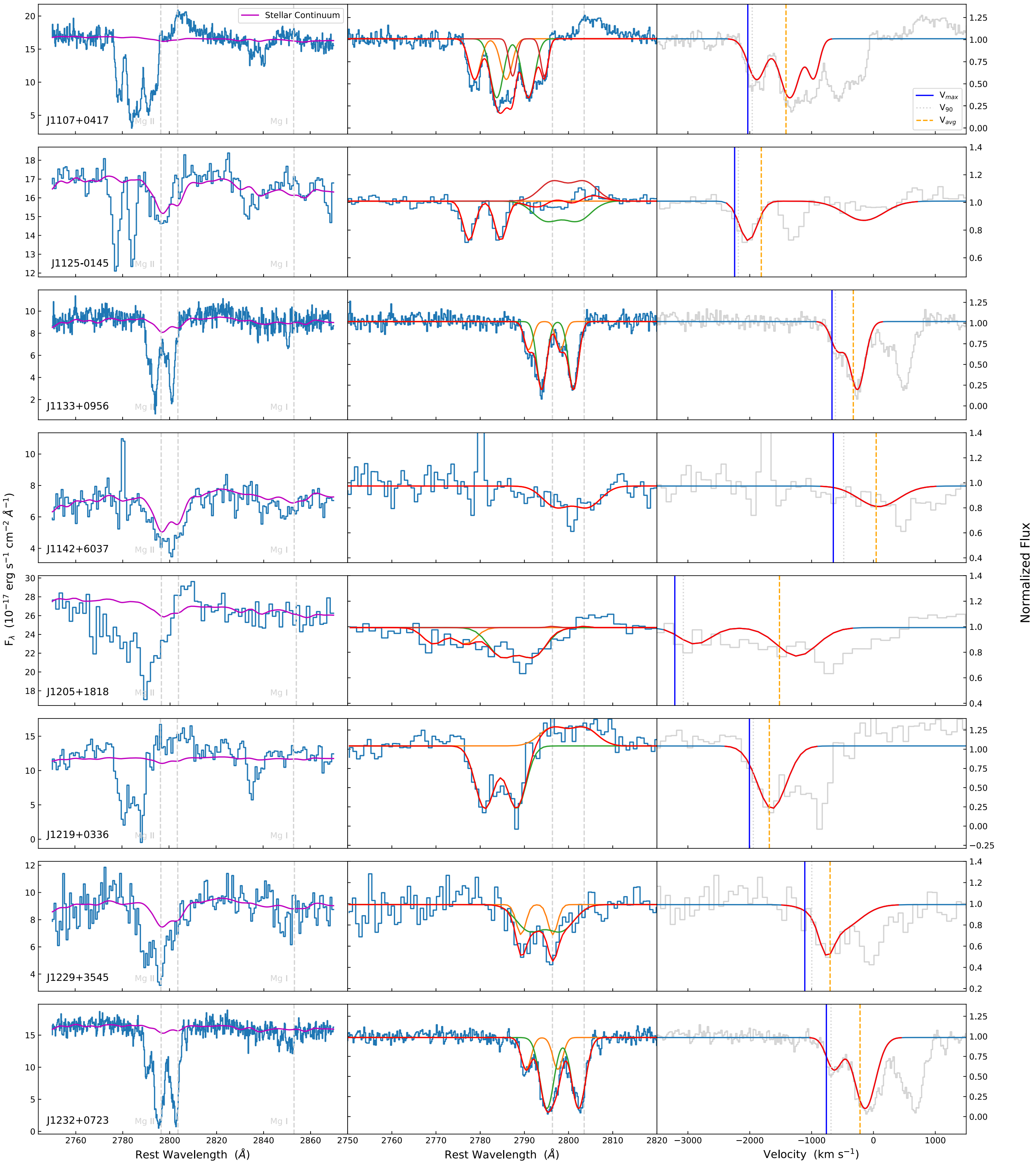

Figure A3. Left: unnormalized MMT/MaGE/LRIS spectra (blue) with the continuum fit (magenta line). Rest positions of Mg I and the Mg II doublet are indicated with gray dotted lines. Center: continuum-normalized spectra with component (green, orange, purple) and composite profile (red) fits. Right: normalized spectra with composite spectra of only the 2796 Å component of the Mg II doublet (red) used to calculate equivalent widths and velocities. $V_{\rm avg}$ and $V_{\rm max}$ are indicated by the vertical orange and blue lines, respectively.

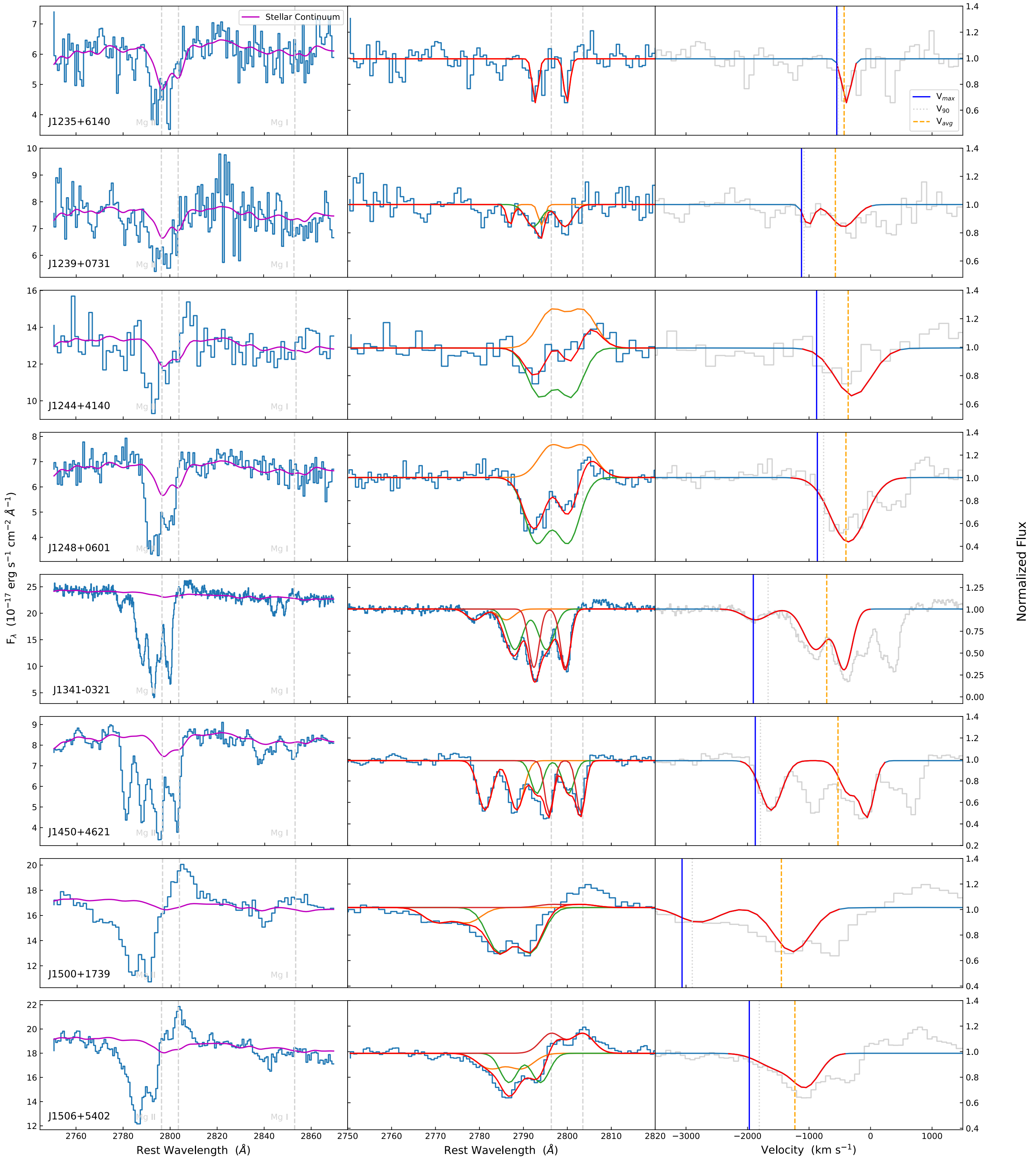

Figure A4. Left: unnormalized MMT/MaGE/LRIS spectra (blue) with the continuum fit (magenta line). Rest positions of Mg I and the Mg II doublet are indicated with gray dotted lines. Center: continuum-normalized spectra with component (green, orange, purple) and composite profile (red) fits. Right: normalized spectra with composite spectra of only the 2796 Å component of the Mg II doublet (red) used to calculate equivalent widths and velocities. V_{avg} and V_{max} are indicated by the vertical orange and blue lines, respectively.

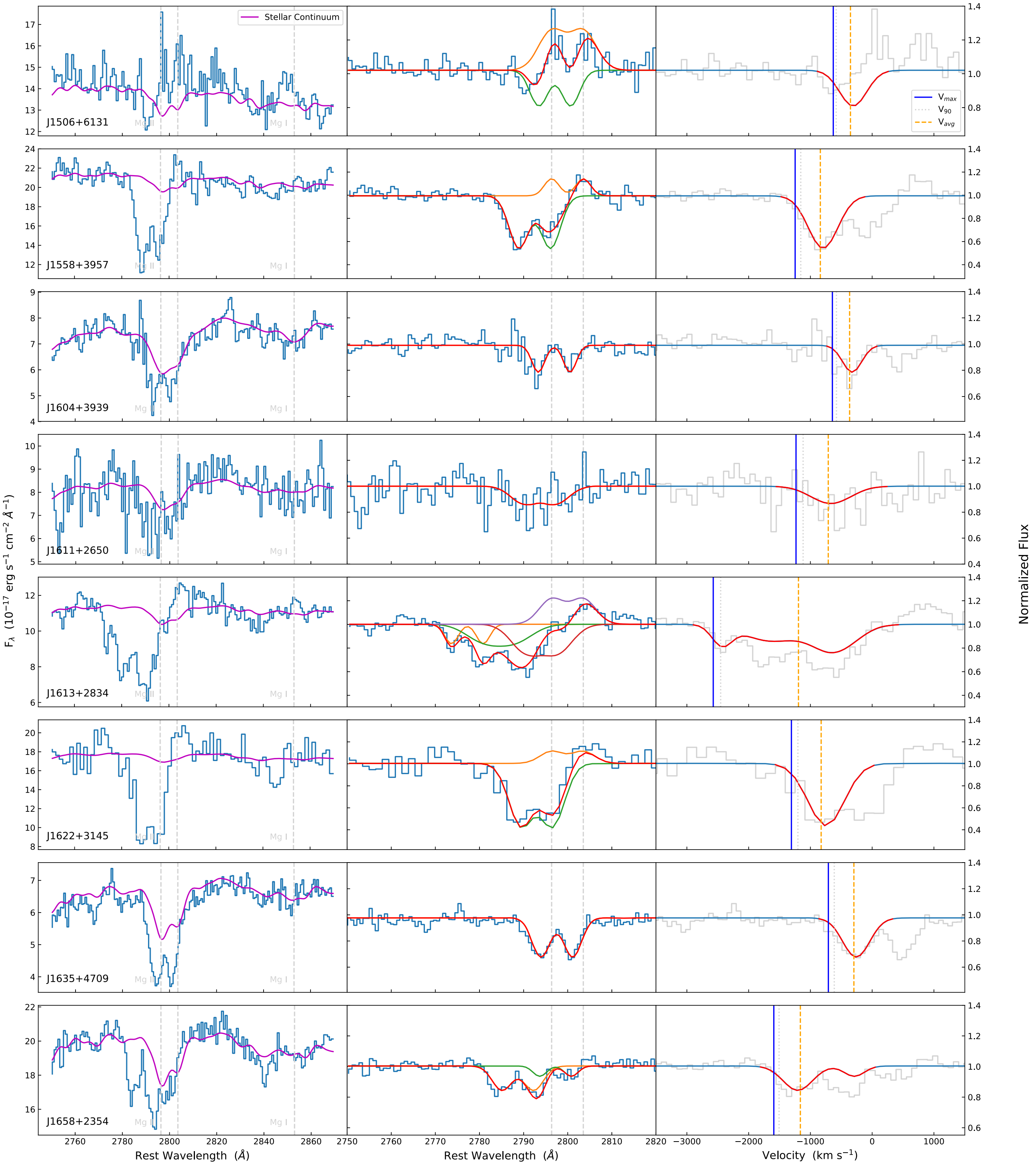

Figure A5. Left: unnormalized MMT/MaGE/LRIS spectra (blue) with the continuum fit (magenta line). Rest positions of Mg I and the Mg II doublet are indicated with gray dotted lines. Center: continuum-normalized spectra with component (green, orange, purple) and composite profile (red) fits. Right: normalized spectra with composite spectra of only the 2796 Å component of the Mg II doublet (red) used to calculate equivalent widths and velocities. $V_{\rm avg}$ and $V_{\rm max}$ are indicated by the vertical orange and blue lines, respectively.

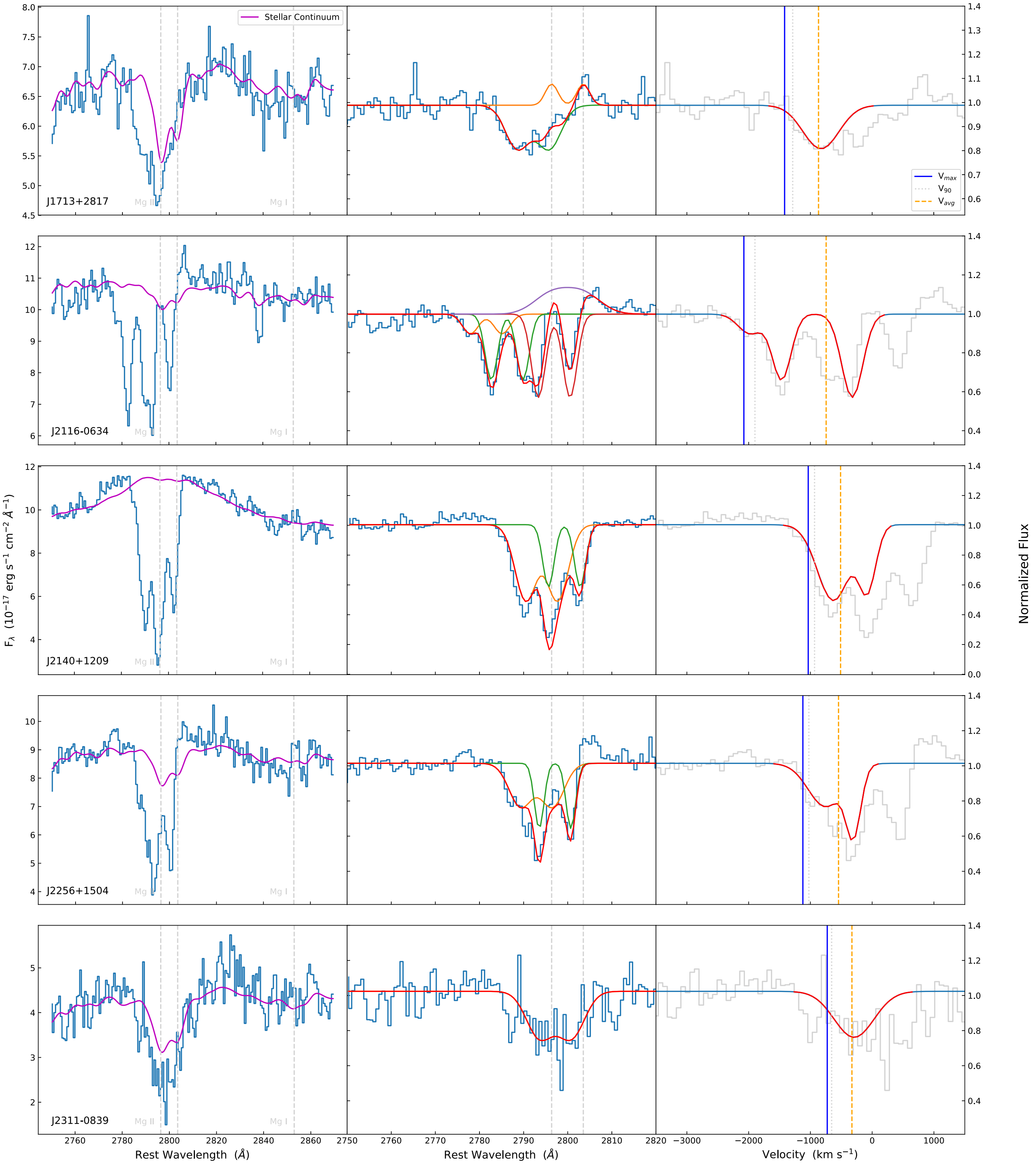

Figure A6. Left: unnormalized MMT/MaGE/LRIS spectra (blue) with the continuum fit (magenta line). Rest positions of Mg I and the Mg II doublet are indicated with gray dotted lines. Center: continuum-normalized spectra with component (green, orange, purple) and composite profile (red) fits. Right: normalized spectra with composite spectra of only the 2796 Å component of the Mg II doublet (red) used to calculate equivalent widths and velocities. $V_{\rm avg}$ and $V_{\rm max}$ are indicated by the vertical orange and blue lines, respectively.

absorption line component and composite profile fits, and continuum-normalized spectra with composite spectra of only the 2796 Å component of the Mg II doublet used to calculate equivalent widths and velocities. The appendix additionally contains, in Table A1, all of the measured properties of the HizEA sample.

Table A1
HizEA Sample Properties

Name	z	Log M_* ($M_\odot$)	Radius (kpc)	LW Age (Myr)	SFR ($M_\odot$ yr^{-1})	$\Sigma_{\rm SFR}$ ($M_\odot$ yr^{-1} kpc^{-2})	Mg II EW (Å)	$V_{\rm avg}$ (km s^{-1})	$V_{\rm max}$ (km s^{-1})
J0106-1023	0.45	$10.7^{+0.2}_{-0.2}$	0.59	30^{+12}_{-7}	166^{+35}_{-31}	76.04	2.09 ± 0.27	-1199 ± 125	-1778 ± 175
J0315-0740	0.46	$11.3^{+0.1}_{-0.1}$	⋯	202^{+37}_{-35}	75^{+29}_{-22}	⋯	1.95 ± 0.44	-588 ± 124	-1073 ± 186
J0811+4716	0.52	$11.2^{+0.2}_{-0.2}$	⋯	298^{+69}_{-75}	28^{+15}_{-12}	⋯	3.02 ± 0.64	-506 ± 330	-1127 ± 585
J0826+4305	0.60	$10.6^{+0.2}_{-0.2}$	$0.17^{+0.05}_{-0.01}$	22^{+11}_{-5}	184^{+53}_{-41}	980.70	3.36 ± 0.44	-1211 ± 175	-1673 ± 233
J0827+2954[b]	0.68	$11.1^{+0.1}_{-0.2}$	1.36	226^{+45}_{-43}	50^{+48}_{-24}	4.33	0.88 ± 0.44	-1218 ± 171	-1495 ± 182
J0901+0314	0.46	$10.7^{+0.2}_{-0.2}$	$0.24^{+0.09}_{-0.14}$	54^{+22}_{-13}	99^{+39}_{-26}	280.91	2.3 ± 0.44	-1328 ± 131	-1668 ± 177
J0905+5759	0.71	$10.7^{+0.3}_{-0.3}$	$0.10^{+0.03}_{-0.04}$	17^{+11}_{-4}	90^{+23}_{-20}	1518.84	3.5 ± 0.44	-2573 ± 250	-2923 ± 301
J0908+1039	0.50	$11.2^{+0.1}_{-0.2}$	1.24	81^{+47}_{-36}	138^{+30}_{-24}	14.31	2.1 ± 0.22	-561 ± 102	-898 ± 113
J0933+5614[b]	0.50	$11.2^{+0.2}_{-0.2}$	⋯	170^{+30}_{-29}	125^{+68}_{-56}	⋯	1.31 ± 0.44	-730 ± 121	-1302 ± 143
J0939+4251	0.41	$10.9^{+0.2}_{-0.3}$	⋯	83^{+27}_{-22}	84^{+36}_{-25}	⋯	1.72 ± 0.25	-506 ± 56	-1154 ± 153
J0944+0930	0.51	$10.6^{+0.2}_{-0.2}$	$0.11^{+0.05}_{-0.07}$	88^{+48}_{-44}	88^{+26}_{-21}	1074.02	5.5 ± 0.49	-1169 ± 129	-1959 ± 201
J1036-0102	0.49	$10.7^{+0.2}_{-0.1}$	⋯	115^{+48}_{-37}	253^{+72}_{-58}	⋯	0.88 ± 0.44	-565 ± 197	-1133 ± 254
J1039+4537	0.63	$10.7^{+0.3}_{-0.2}$	0.55	45^{+22}_{-14}	192^{+52}_{-39}	101.24	2.92 ± 0.44	-712 ± 202	-1671 ± 357
J1052+4104	0.58	$10.6^{+0.2}_{-0.2}$	⋯	105^{+46}_{-31}	112^{+55}_{-37}	⋯	1.53 ± 0.44	-1022 ± 397	-1458 ± 485
J1052+0607	0.56	$10.9^{+0.1}_{-0.2}$	⋯	163^{+33}_{-35}	89^{+52}_{-33}	⋯	0.0	⋯ ± ⋯	⋯ ± ⋯
J1104+5946	0.57	$10.8^{+0.2}_{-0.2}$	0.22	76^{+18}_{-18}	183^{+44}_{-37}	607.30	2.75 ± 1.18	-1136 ± 305	-1617 ± 283
J1107+0417[a]	0.47	$10.6^{+0.2}_{-0.3}$	$0.27^{+0.12}_{-0.19}$	10^{+4}_{-2}	73^{+13}_{-14}	155.17	4.64 ± 0.5	-1414 ± 141	-2031 ± 204
J1125-0145	0.52	$11.0^{+0.2}_{-0.2}$	0.60	102^{+27}_{-25}	227^{+104}_{-68}	100.58	1.77 ± 0.22	-1813 ± 190	-2244 ± 231
J1133+0956	0.48	$11.1^{+0.1}_{-0.2}$	⋯	136^{+34}_{-31}	109^{+22}_{-20}	⋯	2.91 ± 0.3	-326 ± 33	-670 ± 71
J1142+6037	0.57	$11.3^{+0.1}_{-0.1}$	⋯	353^{+32}_{-35}	51^{+33}_{-22}	⋯	0.0	⋯ ± ⋯	⋯ ± ⋯
J1205+1818	0.53	$10.6^{+0.2}_{-0.2}$	⋯	41^{+14}_{-10}	147^{+43}_{-33}	⋯	2.6 ± 0.5	-1519 ± 669	-3211 ± 1488
J1219+0336	0.45	$10.4^{+0.3}_{-0.2}$	$0.41^{+0.12}_{-0.19}$	22^{+14}_{-5}	91^{+28}_{-23}	85.61	3.8 ± 0.44	-1683 ± 169	-2005 ± 204
J1229+3545	0.61	$10.7^{+0.1}_{-0.1}$	0.95	59^{+9}_{-13}	367^{+64}_{-89}	64.74	2.77 ± 0.47	-701 ± 95	-1110 ± 167
J1232+0723	0.40	$10.9^{+0.1}_{-0.1}$	2.20	79^{+30}_{-27}	62^{+16}_{-13}	2.05	4.87 ± 0.47	-217 ± 19	-761 ± 217
J1235+6140	0.60	$11.2^{+0.1}_{-0.1}$	⋯	292^{+47}_{-48}	18^{+28}_{-14}	⋯	0.59 ± 0.33	-429 ± 78	-549 ± 197
J1239+0731	0.54	$11.0^{+0.2}_{-0.1}$	⋯	222^{+42}_{-53}	79^{+49}_{-27}	⋯	0.95 ± 0.21	-572 ± 166	-1122 ± 357
J1244+4140[a]	0.46	$11.0^{+0.1}_{-0.1}$	⋯	156^{+60}_{-57}	82^{+26}_{-18}	⋯	2.4 ± 0.44	-364 ± 93	-877 ± 182
J1248+0601	0.63	$10.8^{+0.1}_{-0.1}$	0.78	141^{+19}_{-16}	77^{+58}_{-52}	20.03	3.72 ± 0.76	-400 ± 195	-865 ± 561
J1341-0321	0.66	$10.5^{+0.2}_{-0.1}$	$0.12^{+0.03}_{-0.04}$	14^{+6}_{-3}	151^{+34}_{-23}	1755.15	4.49 ± 0.5	-712 ± 76	-1906 ± 199
J1450+4621	0.78	$11.1^{+0.1}_{-0.1}$	0.54	107^{+21}_{-13}	191^{+146}_{-70}	104.05	4.42 ± 0.46	-529 ± 95	-1874 ± 186
J1500+1739	0.58	$10.9^{+0.2}_{-0.2}$	⋯	24^{+8}_{-6}	158^{+25}_{-22}	⋯	2.77 ± 0.42	-1450 ± 159	-3064 ± 333
J1506+5402	0.61	$10.6^{+0.2}_{-0.2}$	$0.17^{+0.05}_{-0.08}$	13^{+6}_{-2}	116^{+32}_{-25}	651.86	2.33 ± 0.33	-1230 ± 130	-1971 ± 276
J1506+6131	0.44	$10.7^{+0.2}_{-0.2}$	0.22	88^{+33}_{-24}	47^{+17}_{-12}	160.14	0.84 ± 0.44	-351 ± 52	-630 ± 85
J1558+3957[a]	0.40	$10.4^{+0.3}_{-0.3}$	$0.78^{+0.24}_{-0.38}$	44^{+14}_{-10}	84^{+16}_{-15}	22.10	2.6 ± 0.44	-839 ± 88	-1247 ± 127
J1604+3939	0.56	$11.5^{+0.1}_{-0.1}$	⋯	321^{+46}_{-49}	64^{+42}_{-34}	⋯	0.82 ± 0.23	-365 ± 44	-644 ± 138
J1611+2650	0.48	$11.0^{+0.2}_{-0.2}$	⋯	134^{+37}_{-31}	187^{+90}_{-60}	⋯	1.0 ± 0.25	-711 ± 355	-1233 ± 405
J1613+2834[a]	0.45	$11.1^{+0.2}_{-0.2}$	$0.95^{+0.21}_{-0.27}$	72^{+33}_{-26}	172^{+36}_{-36}	30.42	3.92 ± 0.91	-1193 ± 250	-2573 ± 362
J1622+3145	0.44	$10.6^{+0.2}_{-0.2}$	⋯	34^{+17}_{-9}	151^{+52}_{-33}	⋯	3.83 ± 0.44	-826 ± 86	-1307 ± 156
J1635+4709	0.70	$11.1^{+0.1}_{-0.1}$	1.29	129^{+37}_{-22}	492^{+151}_{-166}	47.09	1.8 ± 0.25	-296 ± 34	-709 ± 94
J1658+2354	0.50	$11.1^{+0.2}_{-0.1}$	⋯	157^{+28}_{-29}	90^{+32}_{-21}	⋯	1.07 ± 0.14	-1163 ± 147	-1592 ± 187
J1713+2817[b]	0.58	$10.9^{+0.1}_{-0.1}$	0.17	134^{+34}_{-24}	229^{+99}_{-72}	1217.81	1.42 ± 0.44	-868 ± 102	-1418 ± 170
J2116-0634	0.73	$10.4^{+0.2}_{-0.2}$	$0.28^{+0.09}_{-0.13}$	21^{+14}_{-4}	110^{+55}_{-27}	216.39	3.4 ± 0.66	-745 ± 230	-2077 ± 407
J2118+0017	0.46	$10.9^{+0.1}_{-0.1}$	2.24	95^{+37}_{-27}	230^{+93}_{-76}	7.30	0.0	⋯ ± ⋯	⋯ ± ⋯
J2140+1209[b]	0.75	$10.4^{+0.2}_{-0.2}$	⋯	192	24^{+20}_{-14}	⋯	4.34 ± 0.45	-511 ± 52	-1035 ± 106
J2256+1504	0.73	$10.8^{+0.2}_{-0.2}$	0.76	65^{+13}_{-11}	428^{+92}_{-85}	117.91	2.31 ± 0.48	-544 ± 245	-1122 ± 703
J2311-0839	0.72	$11.3^{+0.1}_{-0.1}$	⋯	412^{+29}_{-44}	19^{+26}_{-10}	⋯	1.53 ± 0.34	-328 ± 114	-727 ± 145

Notes. Redshifts (z) are derived from the spectra as described in Section 4.2.1. Stellar masses (M_*), star formation rates (SFR), and light-weighted ages of the stellar populations younger than 1 Gyr (LW Age) are derived from Prospector fits to the SEDs (Section 4.1.1). The SFR and M_* values assume a Kroupa IMF (Kroupa 2001). The half-light radius is measured from HST images, when available, and used to calculate the star formation surface density ($\Sigma_{\rm SFR}$) as described in Section 4.1.2. The Mg II EW refers to the 2796 Å line, and is measured from our deblended line profile fits (Section 4.2.2). The measurement of average and maximum outflow velocities ($V_{\rm avg}$, $V_{\rm max}$) is described in Section 4.2.2. $V_{\rm max}$ refers to the velocity measured at blue edge of the line profile, where the cumulative EW distribution reaches 95% of the total.

[a] Obscured AGN candidate.

[b] Identified AGN: Type I AGN (J2140+1209), Type II AGN (J1713+2817), radio galaxy (J0827+2954, J0933+5614). While these targets have confirmed AGN, their bolometric luminosity is not AGN-dominated; see Section 2.3. For the Type I AGN, J2140+1209, the SFR and LW age have been measured in a different manner than those for the other galaxies; see Section 4.1.1 for details.

Appendix B
Data from the Literature: Notes on Individual Samples

B.1. Rubin et al. (2014)

Rubin et al. (2014) analyze Mg II $\lambda\lambda$ 2796,2803 and Fe II $\lambda\lambda$ 2586,2600 absorption line profiles for 105 galaxies at $0.3 < z < 1.4$, drawn from redshift surveys of the GOODS fields and the Extended Groth Strip. A Chabrier IMF is assumed for the SFR calculation, which is carried out through the SED fitting code MAGPHYS (da Cunha & Charlot 2011). An SFR density is then calculated using these SFRs and the galaxy radius measured in the bluest HST/Advanced Camera for Surveys passband. The Mg II and Fe II lines are fit using two different models—a one-component model and a two-component model. The one-component model fits a Voigt profile with λ_0, b_D, C_f, and N as free parameters, while the two-component model fixes an additional component at the galaxy's systemic velocity (with the free component deemed $v_{\rm flow}$). Unlike the present work, Rubin et al. (2014) address P-Cygni emission by masking the affected pixels and setting them to the stellar continuum level. They additionally do not model the stellar continuum. As such, some of the zero-velocity component incorporates stellar Mg II absorption. For this reason, we use their values of $v_{\rm flow}$, the second component of the two-component model, in our paper. Rubin et al. (2014) calculate this value using custom Bayesian statistical software to identify the line center $v_{\rm flow}$ and a maximum velocity extent of the flow absorption component blueward of the systemic velocity, $\Delta v_{\rm max}$. The $\Delta v_{\rm max}$ values of Rubin et al. (2014) are calculated as $\Delta v_{\rm max} = v_{\rm flow} - b_D/\sqrt{2}$, which results in a velocity measured around the FWHM of the feature, roughly between $v_{\rm avg}$ and $v_{\rm max}$ as calculated in this paper. To account for this difference, we reconstructed the Rubin et al. (2014) Mg II absorption line profiles from the parameters in their tables to calculate a correction factor (on average, a multiplier of $\sim$1.25).

B.2. Chisholm et al. (2015)

Chisholm et al. (2015) analyze 51 nearby ($z \leqslant 0.26$), star-forming galaxies observed with the COS on the HST. The sample spans a wide range in galaxy types, from dwarf star-forming galaxies to heavily dust-obscured ultra-luminous infrared galaxies (ULIRGS). The stellar continuum is modeled using stellar population models generated with Starburst99 (Leitherer et al. 1999). The gas outflow velocities are obtained by a single velocity component fitting of four Si II (λ1190, 1193, 1260, and 1304) resonant transitions with a Voigt profile. The line profiles are parameterized with a centroid velocity ($v_{\rm cen}$), Doppler b-parameter (b), optical depth (τ), and covering fraction (C_f). Maximum outflow velocity is defined as 90% of the continuum of the best-fit model (v_{90}). Since this paper uses 95% of the continuum to define $v_{\rm max}$, we apply a correction factor of 1.08 to the Chisholm et al. (2015) values, calculated from the average difference between our measured $v_{\rm max}$ and v_{90} for our sample. Stellar masses are calculated using IR photometry (WISE bands WI and W2; Wright et al. 2010), while SFR is calculated from a combination of IR (WISE W4) and UV (GALEX; Morrissey et al. 2007) observations. One caveat for this sample is consideration of the COS aperture. The aperture is 2$''$5, and for some of the most nearby galaxies, this only includes a single large star cluster. Nonetheless, their velocity scaling relations appear comparable to those of other samples (Rupke 2018). Chisholm et al. (2015) calculate star formation surface densities within the COS aperture. However, we do not include these $\Sigma_{\rm SFR}$ measurements because they are likely higher than the true global values for these nearby galaxies.

B.3. Heckman et al. (2015), Heckman & Borthakur (2016)

Heckman et al. (2015) use two samples of low-redshift ($z < 0.2$) starburst galaxies: 19 galaxies observed with the Far-Ultraviolet Spectroscopic Explorer (FUSE) and 21 LBAs observed with the COS. Outflow velocities were measured with Si III λ1206 for COS galaxies and an unweighted mean of C III λ977 (47.9 eV) and N II λ1084 for FUSE galaxies. For both samples, the spectroscopic aperture encompasses most of the galaxy light. Comparable to our $V_{\rm avg}$, the velocities were obtained through nonparametric methods based on the flux-weighted line centroids defined relative to the systemic velocity of the galaxy. The SFR was calculated using UV and IR photometry and a standard Kroupa/Chabrier IMF. The total galaxy stellar mass is derived from near-IR and/or multiband optical photometry, and they use the starburst half-light radius to calculate SFR surface density (i.e., $\Sigma_{\rm SFR} = {\rm SFR}/2\pi r_*^2$).

In Heckman & Borthakur (2016), the authors reanalyze the COS and FUSE spectra described in the previous paper, measuring a maximum outflow velocity at the point where the line EW distribution reaches 98% of the total. They use the Si II λ1260 and C II λ1334 lines (COS) and the C II λ1036 line (FUSE). The same stellar mass, SFR, and $\Sigma_{\rm SFR}$ values from the previous paper are used.

B.4. Kornei et al. (2012)

Kornei et al. (2012) measure 72 star-forming galaxies between $0.25 < z < 1.34$ in the Extended Groth Strip (Davis et al. 2003). Galaxies were selected from the Deep Extragalactic Evolutionary Probe 2 (Newman et al. 2013, DEEP2) survey with follow-up Keck/LRIS (Oke et al. 1995) spectroscopy. A stellar continuum is not fit to the spectra. Average velocities were calculated for both individual targets and composite spectra by the simultaneous fitting of the velocity centroids for five Fe II lines (Fe II λ2344, Fe II $\lambda\lambda$ 2374/2382, Fe II $\lambda\lambda$ 2587/2600). Maximum outflow velocities were calculated only for composite stacks using the profiles of the Fe II and Mg II lines. We do not include the Kornei et al. (2012) average velocities measured with Fe II, as the values were close to systemic velocity for most targets and composite spectra. The composite spectra Mg II maximum velocities were determined by identifying the wavelength at which the blue part of the line profile is 1σ less than the continuum, perturbing the spectrum by a value drawn from a Gaussian distribution of width σ, and repeating the same procedure a total of 1000 times. This is comparable to our 95th percentile velocities. Stellar masses were calculated from SED modeling with *BRIK* photometry. Galaxy sizes are from Petrosian radii. SFRs were calculated from the rest-frame UV luminosity and converted from a Salpeter IMF to a Chabrier IMF.

B.5. Weiner et al. (2009)

Weiner et al. (2009) use a sample of 1406 galaxy spectra at $z \sim 1.3$–1.5 from the DEEP2 redshift survey (Davis et al. 2003), focusing on star-forming galaxies over a range of stellar masses and star formation rates. These spectra are stacked into composite spectra and split into bins (each containing a few hundred galaxies) for different galaxy properties. No stellar continuum is fit. The systemic and outflowing velocity components are separated by measuring the red side of the redder (2803 Å) Mg II line (absorption at systemic velocities) and the blue side of the bluer (2796 Å) line (absorption in the outflow). A Gaussian line profile is fit to the positive velocity data (fitting parameters of continuum, intensity, and dispersion, with the central velocity held fixed at 0). Assuming equal line intensity, a duplicate Gaussian is applied to the bluer Mg II line to obtain the asymmetric, outflowing component. The stellar masses and SFRs were calibrated from K band and from the Spitzer/MIPS (Rieke et al. 2004) IR fluxes. The SFRs use a Kroupa IMF while the stellar masses are normalized to a Chabrier IMF.

B.6. Bordoloi et al. (2014)

Bordoloi et al. (2014) measure Mg II absorption lines in the coadded spectra of a sample of 486 zCOSMOS galaxies (Lilly et al. 2007) at $1 < z < 1.5$, across a range of stellar masses and SFRs. They do not fit a stellar continuum. The systemic velocity ISM absorption component from the coadded spectra is removed in order to identify the strength of the outflowing gas in the coadded spectrum. In a method similar to Weiner et al. (2009), they decompose the systemic and outflowing components, with a Gaussian fitted on the red side of the 2803 Å line (within $0\,\mathrm{km\,s^{-1}} < v < 1500\,\mathrm{km\,s^{-1}}$). This profile is divided from both lines of the doublet, and the mean velocity is then measured from the remaining outflowing absorption. Stellar masses and SFRs for these galaxies were estimated by SED fitting at the known spectroscopic redshifts of the galaxies, using the Hyperzmass (Bolzonella et al. 2000) code, which uses a Chabrier IMF.

B.7. Sugahara et al. (2017)

Sugahara et al. (2017) explore the redshift evolution of galaxy outflow velocity through a systematic study of star-forming galaxies at $z \sim 0$–2 taken from SDSS DR7 (Abazajian et al. 2009), DEEP2 DR4 (Newman et al. 2013), and Keck optical spectroscopy (Erb et al. 2006). The spectra are stacked in homogeneous galaxy samples with similar stellar mass distributions at $z \sim 0$, 1, and 2. They assume the absorption profiles consist of three components: the intrinsic stellar absorption, systemic ISM gas, and the outflow component. They model the stellar continuum using SSP models and normalize before performing the multicomponent fitting of absorption lines in the stacked spectra. Although they measure outflow velocity with different ion tracers at different redshifts, we limit our comparison to only their Mg II $\lambda\lambda$ 2796, 2804 measurements at $z \sim 1$. Voigt profiles are fit for the outflowing gas profile (i.e., $\lambda_{0,\mathrm{out}}$, $\tau_{0,\mathrm{out}}$, C_f, and $b_{D,\mathrm{out}}$) and three parameters for the systemic profile (i.e., $\tau_{0,sys}$, C_f, and $b_{D,sys}$), with the central wavelength λ_{sys} fixed to the rest-frame wavelength. A central velocity is measured, along with a maximum velocity defined as 90% of the continuum, which we correct by a factor of 1.08 to match our 95% v_{max}. The stellar masses and SFRs are calculated assuming a Chabrier IMF. SFRs are measured from extinction-corrected Hα and from M_B and $(U - B)$ colors for $z \sim 1$ galaxies.

B.8. Martin et al. (2012)

Martin et al. (2012) investigate a sample of 208 galaxies between $0.64 < z < 1.29$ in the DEEP2 survey (Davis et al. 2003) using Keck/LRIS spectroscopy. From this sample, 35 galaxies were found to have outflows, 29 of which had outflow velocities measured using Fe II and Mg II absorption. Both a single-component Gaussian fit and a two-component systemic and outflowing component fit are applied simultaneously to five resonance Fe II lines at 2250, 2261, 2344, 2374, and 2587 Å and Mg II 2796 Å . The maximum velocity is determined by identifying the wavelength at which the blue edge of the line profile is 1σ less than the continuum. Stellar masses and SFRs were derived from SED fitting using a Chabrier stellar IMF. SFRs were only available for a subset of the data points. We substitute SFRs calculated according to Equation (2) of Sugahara et al. (2017) using the U–B colors and magnitudes provided in Martin et al. (2012).

B.9. Prusinski et al. (2021)

Prusinski et al. (2021) use two independent data sets covering a sample of 22 galaxies between $1 < z < 1.5$ from the CANDELS (Grogin et al. 2011) and COSMOS (Scoville et al. 2007) fields. The intensity and velocity of the outflows are measured using Keck/DEIMOS spectroscopy covering Fe II and Mg II interstellar absorption lines. A stellar continuum is not fit. For each galaxy, velocity centroids (Δv) are measured along with equivalent widths through direct integration rather than a profile fit. Maximum blueshifted velocities (v_{max}) were measured for all of the absorption lines of interest. The maximum blueshifted velocity is defined as the velocity corresponding to the wavelength where the absorption feature first meets the continuum on the blue side of the line. Stellar mass is determined from the SED in the 3D HST catalog (Skelton et al. 2014). Spatial extent of the galaxies and SFR were measured with HST WFC3/G141 grism spectroscopy yielding Hα emission line maps. A Salpeter (1955) IMF is assumed.

B.10. Banerji et al. (2011)

Banerji et al. (2011) investigate 40 luminous starburst galaxies at $z = 0.7$–1.7 (median $z = 1.3$) using Keck II DEIMOS spectra. 19 of these are SMGs, and 21 are submillimeter-faint radio galaxies (SFRGs). SMGs and SFRGs are some of the most extreme star-forming systems at high redshifts, making this sample one of the only data points to occupy the same regime of SFR as our HizEA sample. They create composite stacks of 26 spectra for various galaxy properties, then measure outflow velocity from Mg II. While they do not fit a stellar continuum, they attempt to avoid stellar contamination by only measuring velocities greater than 100 km s^{-1} blueward of the systemic velocity. The velocities and equivalent widths are calculated by measuring the line centroids according to the apparent optical depth (AOD) formalism of Savage & Sembach (1991). SFRs are calculated from the 1.4 GHz radio fluxes, and stellar masses are calculated using the SED-fitting code HYPERZMASS. No size information is provided for the galaxies. Because this is a particularly important sample to compare to the HizEA galaxies, we estimate an average Σ_{SFR} for the sample by using a typical half-light radii for SMGs from the literature (2.8 ± 0.4 kpc in the

H band; Swinbank et al. 2010) and the median SFR of their star-forming-only sample (110 $M_\odot$ yr^{-1}).

Appendix C
Data from the Literature: Comparison Considerations

As discussed in Section 5.1, combining various data sets from the literature can be problematic due to a lack of uniformity in the data and measurement techniques. Below we discuss several concerns specific to outflow studies, and we justify the choices we made to arrive at a suitable comparison sample for the HizEA galaxies.

Across the samples included in this paper, the first challenge is the different measurement methods and velocity definitions employed by the various projects. Before fitting any absorption lines, the HizEA sample is fit with a stellar population model used to normalize the spectrum, thereby removing *stellar* Mg II contamination (Section 4.2.1). However, only a few other studies included here for comparison perform this step (Chisholm et al. 2015; Sugahara et al. 2017), with most instead applying some variation of a polynomial fit to the continuum around the lines of interest. Stellar absorption is, in theory, addressed by fitting a zero-velocity absorption component, but this is not carried out by all of the studies.

When fitting the absorption lines, methods included nonparametric, single-component, or multicomponent fits (some using Gaussian and some using Voigt profiles). For velocity measurements, almost all studies present some form of average (or central) outflow velocity. This measurement is relatively simple to define and less sensitive to the S/N of the data. However, strong absorption at systemic velocities (from either the stellar population or the ambient ISM) can affect this measurement. The average velocity is often simply the velocity centroid of the fitted profile (Kornei et al. 2012; Chisholm et al. 2015; Heckman et al. 2015; Prusinski et al. 2021), but some studies remove a systemic component before measuring (Weiner et al. 2009; Martin et al. 2012; Rubin et al. 2014; Bordoloi et al. 2014) to avoid biasing toward zero velocity. In the HizEA sample, we correct for stellar absorption, and there is very little ISM absorption at systemic velocity, but for some samples, the contribution is more significant. Weiner et al. (2009) briefly discuss the strength of systemic components in their sample, finding that the systemic absorption is strongly dependent on the galaxy properties, with weaker components for low-mass, low-SFR galaxies and stronger components in redder and/or more massive objects.

The maximum velocity definitions and measurements are subject to further variation. While these measurements are less sensitive to systemic velocity gas, they are much more sensitive to the S/N of the data. This paper defines maximum velocity as an equivalent width-weighted 95th percentile of a composite line profile constructed from the Mg II λ2796 component. Chisholm et al. (2015) use the 90th percentile, to which we apply a multiplicative correction factor of 1.08 based on the difference between the 90th and 95th percentile velocities in our own sample. Others define their maximum velocity at the wavelength corresponding to 1σ below to continuum (Kornei et al. 2012; Martin et al. 2012), or at the continuum (Prusinski et al. 2021). Some studies present average velocities for individual targets, but maximum velocities only for composite stacks where the edges of the line profiles are better defined and/or less noisy (Kornei et al. 2012). Without the spectroscopic data in-hand, it is difficult to correct for these differences in any rigorous fashion. Consequently, some of the velocity scatter in the scaling relations may be ascribable to variations in measurement technique.

Further complicating this picture is the presence of resonant emission in the Mg II doublet, which can fill in absorption near the systemic velocity and result in higher measured outflow velocities if not properly accounted for. This effect has been explored in several of the samples included in this study, as well as others in the literature (Rubin et al. 2010; Prochaska et al. 2011; Zhu et al. 2015; Scarlata & Panagia 2015). Resonant Mg II emission is not a major concern in the HizEA sample, where the velocities are large and minimally impacted by including a zero-velocity emission component in the line profile fit. However, some of our comparison samples may suffer more from this effect. The Kornei et al. (2012) sample, for example, finds a ~200 km s^{-1} difference between $v_{\max}$ measured with Mg II versus Fe II in their composite stacks. The near-UV Fe II transitions have nonresonant emission channels and are therefore less impacted by resonant emission infilling than those of Mg II (Zhu et al. 2015). However, they also have lower oscillator strengths than those of Mg II, which can make the weak high-velocity tail of the absorption line profile more difficult to detect. In summary, it is not a simple matter to correct the Mg II velocities for emission infilling, which is expected to vary with dust attenuation and outflow geometry (Prochaska et al. 2011; Scarlata & Panagia 2015). Variations in how (and if) resonant emission is corrected for will add vertical scatter in the scaling relations.

The difference in ionic species used for each project also contributes to uncertainty in sample comparisons. Conflicting findings exist for the effects of ionization energy on outflow velocity measurements. The ions with higher ionization energies may trace higher-velocity clouds. This is seen in the theoretical work of Tanner et al. (2017), where measurements of outflow velocity from synthetic absorption profiles of twelve different silicon ions exhibit (nonuniform) increases with ionization state and differences in absorption profile shape affecting $v_{\max}$. They also find that the velocity versus SFR scaling relationship can vary with ion used. de la Cruz et al. (2020) also use synthetic absorption profiles and find that velocity increases with ionization state, as measured from low-ionization ions (Si II and C II) to high-ionization ions (N V and O VI). Observational studies have noted for some time that different gas phases have different velocities, with cold neutral and/or molecular gas moving at lower velocity than warm ionized gas (Veilleux et al. 2020). For example, the cool molecular gas outflowing from M82 has a maximum deprojected outflow velocity of ~230 km s^{-1} (Shen & Lo 1995; Walter et al. 2002), well below the 525–655 km s^{-1} measured for the warm ionized gas (Shopbell & Bland-Hawthorn 1998). Smaller outflow velocities in the neutral gas relative to the ionized components were initially seen in LIRGs and ULIRGs (Rupke et al. 2005); though, more recent work demonstrates this is not always the case (Rupke & Veilleux 2013; Fluetsch et al. 2021). In a lensed galaxy at $z = 2.9$, Chisholm et al. (2018) find the line profiles of a range of ions to be remarkably similar (from O I to trace neutral gas up to O VI to trace hotter, transitional phase gas).

Given the conflicting answers on the importance of the gas ionization state, we incorporate only samples using species with broadly similar ionization potentials (15–48 eV). We do not include any Na I $\lambda\lambda$ 5890,5896 samples, despite the existence of a number of historically important studies (e.g., Rupke et al. 2005; Martin 2005). When velocity points from the Rupke et al. (2005) paper were added to our velocity versus SFR scaling relation plots, the points fell far below the trend line defined by the rest of our comparison sample (e.g., they clustered around ∼300 km s^{-1} for log SFR ∼ 2, whereas our sample clusters around 1000 km s^{-1} for the same SFR value). In addition to the ionization potential effects noted above, dust may play a role in the line profile differences. At the relatively red wavelength of Na I, observations will probe deeper into the host galaxy than they do in the ultraviolet, potentially causing Na I to have a more prominent systemic velocity component.

Finally, there is ongoing debate about redshift evolution in the outflow scaling relations. Evolution seems probable, given that the star formation and galaxy properties at $z > 1$ differ significantly from local galaxies, with more ongoing accretion, higher gas mass fractions, higher $\Sigma_{\rm SFR}$ and SFR/M_*, and possible differences in star formation efficiency (e.g., Tacconi et al. 2013). Barai et al. (2015) find from their MUPPI simulations that the correlation between outflow velocity and SFR is positive for $0.8 < z < 5$, but steeper at earlier times and flatter at later epochs. They assert the most important factor for this redshift evolution is the evolution of the SFR main sequence to lower SFRs at fixed mass.

While low-z galaxy winds have been well characterized through numerous different techniques, samples at high redshift are currently small, with ancillary data harder to obtain. Sugahara et al. (2017) claim to observe a redshift evolution in velocity as a function of SFR using stacked spectra from three different surveys spanning $z = 0$–2. They posit that the increase in outflow velocities at fixed SFR from $z \sim 0$ to 2 can be explained by the increase in $\Sigma_{\rm SFR}$ at fixed SFR toward high redshift. In contrast, Calabrò et al. (2022) finds lower outflow velocities at $z \sim 2$–5 than locally at fixed SFR and M_*, which they attribute to the increased role of inflows and turbulence at high redshift. This paper thus avoids samples of $z \gtrsim 1.5$, such as those studying Lyman Break Galaxies (LBGs) or lensed galaxies (e.g., Pettini et al. 2002; Shapley et al. 2003; Verhamme et al. 2008; Marques-Chaves et al. 2020). However, as our comparison sample covers redshifts of $0 < z < 1.5$, some redshift evolution may contribute to the scatter in the scaling relations.

While the concerns listed in this section should be considered when drawing conclusions from the scaling relations, we have taken steps to create a reasonably uniform sample from a large and varied literature collection: selecting for similar targets, redshifts, and ionic species, applying corrections to velocity measurements to closer align them with our definitions (noted where applicable in Appendix B), and unifying the IMFs to a Chabrier IMF by applying correction factors. In Figures 6 and 7, we see generally good agreement among different samples, highlighting the success of this approach.

ORCID iDs

Julie D. Davis https://orcid.org/0000-0002-9634-7652
Christy A. Tremonti https://orcid.org/0000-0003-3097-5178
Cameren N. Swiggum https://orcid.org/0000-0001-9201-5995
John Moustakas https://orcid.org/0000-0002-2733-4559
Alison L. Coil https://orcid.org/0000-0002-2583-5894
Ryan C. Hickox https://orcid.org/0000-0003-1468-9526
Serena Perrotta https://orcid.org/0000-0002-2451-9160
Grayson C. Petter https://orcid.org/0000-0001-6941-8411
Gregory H. Rudnick https://orcid.org/0000-0001-5851-1856
David S. N. Rupke https://orcid.org/0000-0002-1608-7564
Paul H. Sell https://orcid.org/0000-0003-1771-5531
Kelly E. Whalen https://orcid.org/0000-0002-8571-9801

References

Abazajian, K. N., Adelman-McCarthy, J. K., Agüeros, M. A., et al. 2009, ApJS, 182, 543
Agertz, O., & Kravtsov, A. V. 2015, ApJ, 804, 18
Ahumada, R., Prieto, C. A., Almeida, A., et al. 2020, ApJS, 249, 3
Aihara, H., Allende Prieto, C., An, D., et al. 2011, ApJS, 193, 29
Angel, J. R. P., Hilliard, R. L., & Weymann, R. J. 1979, The MMT and the Future of Ground-Based Astronomy, 385, 87
Astropy Collaboration, Robitaille, T. P., Tollerud, E. J., et al. 2013, A&A, 558, A33
Baldwin, J. A., Phillips, M. M., & Terlevich, R. 1981, PASP, 93, 5
Banerji, M., Chapman, S. C., Smail, I., et al. 2011, MNRAS, 418, 1071
Barai, P., Monaco, P., Murante, G., et al. 2015, MNRAS, 447, 266
Barnes, J. E., & Hernquist, L. 1996, ApJ, 471, 115
Barro, G., Faber, S. M., Pérez-González, P. G., et al. 2014, ApJ, 791, 52
Becker, R. H., White, R. L., & Helfand, D. J. 1995, ApJ, 450, 559
Bell, E. F., McIntosh, D. H., Katz, N., & Weinberg, M. D. 2003, ApJS, 149, 289
Biernacki, P., & Teyssier, R. 2018, MNRAS, 475, 5688
Blecha, L., Snyder, G. F., Satyapal, S., et al. 2018, MNRAS, 478, 3056
Bochanski, J. J., Hennawi, J. F., Simcoe, R. A., et al. 2009, PASP, 121, 1409
Bolzonella, M., Miralles, J.-M., & Pelló, R. 2000, A&A, 363, 476
Bordoloi, R., Lilly, S. J., Hardmeier, E., et al. 2014, ApJ, 794, 130
Bothwell, M. S., Kennicutt, R. C., Johnson, B. D., et al. 2011, MNRAS, 415, 1815
Bournaud, F., Chapon, D., Teyssier, R., et al. 2011, ApJ, 730, 4
Brinchmann, J., Charlot, S., White, S. D. M., et al. 2004, MNRAS, 351, 1151
Calabrò, A., Pentericci, L., Talia, M., et al. 2022, A&A, 667, A117
Cappellari, M. 2017, MNRAS, 466, 798
Cappellari, M., & Emsellem, E. 2004, PASP, 116, 138
Chabrier, G. 2003, PASP, 115, 763
Chen, H.-W., Wild, V., Tinker, J. L., et al. 2010, ApJL, 724, L176
Chevalier, R. A., & Clegg, A. W. 1985, Natur, 317, 44
Chisholm, J., Bordoloi, R., Rigby, J. R., et al. 2018, MNRAS, 474, 1688
Chisholm, J., Tremonti, C. A., Leitherer, C., et al. 2015, ApJ, 811, 149
Chisholm, J., Tremonti, C. A., Leitherer, C., et al. 2017, MNRAS, 469, 4831
Chisholm, J., Tremonti Christy, A., Leitherer, C., et al. 2016, MNRAS, 463, 541
Choi, J., Dotter, A., Conroy, C., et al. 2016, ApJ, 823, 102
Cicone, C., Maiolino, R., & Marconi, A. 2016, A&A, 588, A41
Coil, A. L., Weiner, B. J., Holz, D. E., et al. 2011, ApJ, 743, 46
Conroy, C., & Gunn, J. E. 2010, ApJ, 712, 833
Conroy, C., Gunn, J. E., & White, M. 2009, ApJ, 699, 486
Cooke, R. J., Pettini, M., & Steidel, C. C. 2018, ApJ, 855, 102
da Cunha, E., & Charlot, S. 2011, MAGPHYS: Multi-wavelength Analysis of Galaxy Physical Properties, Astrophysics Source Code Library, ascl:1106.010
Daddi, E., Renzini, A., Pirzkal, N., et al. 2005, ApJ, 626, 680
Davis, M., Faber, S. M., Newman, J., et al. 2003, Proc. SPIE, 4834, 161
de la Cruz, L. M., Schneider, E. E., & Ostriker, E. C. 2020, ApJ, 919, 112
Dekel, A., & Burkert, A. 2014, MNRAS, 438, 1870
Diamond-Stanic, A. M., Moustakas, J., Sell, P. H., et al. 2021, ApJ, 912, 11
Diamond-Stanic, A. M., Moustakas, J., Tremonti, C. A., et al. 2012, ApJL, 755, L26
Erb, D. K., Quider, A. M., Henry, A. L., et al. 2012, ApJ, 759, 26
Erb, D. K., Steidel, C. C., Shapley, A. E., et al. 2006, ApJ, 647, 128
Fabian, A. C. 2012, ARA&A, 50, 455
Fielding, D. B., & Bryan, G. L. 2022, ApJ, 924, 82
Fluetsch, A., Maiolino, R., Carniani, S., et al. 2021, MNRAS, 505, 5753
Foreman-Mackey, D., Hogg, D. W., Lang, D., et al. 2013, PASP, 125, 306
French, K. D. 2021, PASP, 133, 072001
Geach, J. E., Hickox, R. C., Diamond-Stanic, A. M., et al. 2013, ApJL, 767, L17
Geach, J. E., Hickox, R. C., Diamond-Stanic, A. M., et al. 2014, Natur, 516, 68

Geach, J. E., Tremonti, C., Diamond-Stanic, A. M., et al. 2018, ApJL, 864, L1
Grogin, N. A., Kocevski, D. D., Faber, S. M., et al. 2011, ApJS, 197, 35
Gronke, M., & Oh, S. P. 2018, MNRAS, 480, L111
Gunn, J. E., Carr, M., Rockosi, C., et al. 1998, AJ, 116, 3040
Häußler, B., Bamford, S. P., Vika, M., et al. 2013, MNRAS, 430, 330
Heckman, T. M., Alexandroff, R. M., Borthakur, S., et al. 2015, ApJ, 809, 147
Heckman, T. M., & Borthakur, S. 2016, ApJ, 822, 9
Heckman, T. M., Hoopes, C. G., Seibert, M., et al. 2005, ApJL, 619, L35
Heckman, T. M., Lehnert, M. D., Strickland, D. K., et al. 2000, ApJS, 129, 493
Heckman, T. M., & Thompson, T. A. 2017, Handbook of Supernovae (Cham: Springer), 2431
Hinshaw, G., Larson, D., Komatsu, E., et al. 2013, ApJS, 208, 19
Hogg, D. W., Blanton, M., Strateva, I., et al. 2002, AJ, 124, 646
Hopkins, P. F., Quataert, E., & Murray, N. 2012, MNRAS, 421, 3522
Hunter, J. D. 2007, CSE, 9, 90
Johnson, B. D., Leja, J., Conroy, C., et al. 2021, ApJS, 254, 22
Kauffmann, G., Heckman, T. M., White, S. D. M., et al. 2003, MNRAS, 341, 33
Kennicutt, R. C., & Evans, N. J. 2012, ARA&A, 50, 531
Kewley, L. J., Maier, C., Yabe, K., et al. 2013, ApJL, 774, L10
Kim, C.-G., Ostriker, E. C., Somerville, R. S., et al. 2020, ApJ, 900, 61
Kimble, R. A., MacKenty, J. W., O'Connell, R. W., et al. 2008, Proc. SPIE, 7010, 70101E
Kornei, K. A., Shapley, A. E., Martin, C. L., et al. 2012, ApJ, 758, 135
Kouroumpatzakis, K., Zezas, A., Maragkoudakis, A., et al. 2021, MNRAS, 506, 3079
Kroupa, P. 2001, MNRAS, 322, 231
Landsman, W. B. 1993, in ASP Conf. Ser. 52, Astronomical Data Analysis Software and Systems II, ed. R. J. Hanisch, R. J. V. Brissenden, & J. Barnes (San Francisco, CA: ASP), 246
Lang, D. 2014, AJ, 147, 108
Lawrence, A., Warren, S. J., Almaini, O., et al. 2007, MNRAS, 379, 1599
Leitherer, C., Schaerer, D., Goldader, J. D., et al. 1999, ApJS, 123, 3
Leja, J., Carnall, A. C., Johnson, B. D., et al. 2019, ApJ, 876, 3
Lilly, S. J., Le Fèvre, O., Renzini, A., et al. 2007, ApJS, 172, 70
Lochhaas, C., Thompson, T. A., Quataert, E., et al. 2018, MNRAS, 481, 1873
Lochhaas, C., Thompson, T. A., & Schneider, E. E. 2021, MNRAS, 504, 3412
Maltby, D. T., Almaini, O., McLure, R. J., et al. 2019, MNRAS, 489, 1139
Marigo, P., Girardi, L., Bressan, A., et al. 2008, A&A, 482, 883
Marques-Chaves, R., Pérez-Fournon, I., Shu, Y., et al. 2020, MNRAS, 492, 1257
Marshall, J. L., Burles, S., Thompson, I. B., et al. 2008, Proc. SPIE, 7014, 701454
Martin, C. L. 2005, ApJ, 621, 227
Martin, C. L., & Bouché, N. 2009, ApJ, 703, 1394
Martin, C. L., Shapley, A. E., Coil, A. L., et al. 2012, ApJ, 760, 127
Meurer, G. R., Heckman, T. M., Lehnert, M. D., et al. 1997, AJ, 114, 54
Morrissey, P., Conrow, T., Barlow, T. A., et al. 2007, ApJS, 173, 682
Morrissey, P., Matuszewski, M., Martin, D. C., et al. 2018, ApJ, 864, 93
Moster, B. P., Somerville, R. S., Maulbetsch, C., et al. 2010, ApJ, 710, 903
Moustakas, J., Coil, A. L., Aird, J., et al. 2013, ApJ, 767, 50
Moustakas, J., & Kennicutt, R. C. 2006, ApJ, 651, 155
Murray, N., Quataert, E., & Thompson, T. A. 2005, ApJ, 618, 569
Naab, T., & Ostriker, J. P. 2017, ARA&A, 55, 59
Nelson, D., Pillepich, A., Springel, V., et al. 2019, MNRAS, 490, 3234
Nelson, D., Springel, V., Pillepich, A., et al. 2019, ComAC, 6, 2
Newman, J. A., Cooper, M. C., Davis, M., et al. 2013, ApJS, 208, 5
Newville, M., Stensitzki, T., Allen, D. B., et al. 2014, lmfit/lmfit-py v0.9.14, Zenodo, doi:10.5281/zenodo.11813
Noeske, K. G., Weiner, B. J., Faber, S. M., et al. 2007, ApJL, 660, L43
Oke, J. B., Cohen, J. G., Carr, M., et al. 1995, PASP, 107, 375
Overzier, R. A., Heckman, T. M., Kauffmann, G., et al. 2008, ApJ, 677, 37
Peng, C. Y., Ho, L. C., Impey, C. D., et al. 2002, AJ, 124, 266
Perrotta, S., Coil, A. L., Rupke, D. S. N., et al. 2023, ApJ, 949, 9
Perrotta, S., George, E. R., Coil, A. L., et al. 2021, ApJ, 923, 275
Petter, G. C., Kepley, A. A., Hickox, R. C., et al. 2020, ApJ, 901, 138
Pettini, M., Rix, S. A., Steidel, C. C., et al. 2002, Ap&SS, 281, 461
Planck Collaboration, Ade, P. A. R., Aghanim, N., et al. 2016, A&A, 594, A13
Prochaska, J. X., Kasen, D., & Rubin, K. 2011, ApJ, 734, 24
Prusinski, N. Z., Erb, D. K., & Martin, C. L. 2021, AJ, 161, 212
Qiu, Y., Hu, H., Inayoshi, K., et al. 2021, ApJL, 917, L7
Rich, J. A., Kewley, L. J., & Dopita, M. A. 2011, ApJ, 734, 87
Rich, J. A., Kewley, L. J., & Dopita, M. A. 2014, ApJL, 781, L12
Rich, J. A., Kewley, L. J., & Dopita, M. A. 2015, ApJS, 221, 28
Richards, G. T., Fan, X., Newberg, H. J., et al. 2002, AJ, 123, 2945
Rieke, G. H., Wright, G. S., Böker, T., et al. 2015, PASP, 127, 584
Rieke, G. H., Young, E. T., Engelbracht, C. W., et al. 2004, ApJS, 154, 25
Rubin, K. H. R., Prochaska, J. X., Koo, D. C., et al. 2014, ApJ, 794, 156
Rubin, K. H. R., Prochaska, J. X., Ménard, B., et al. 2011, ApJ, 728, 55
Rubin, K. H. R., Weiner, B. J., Koo, D. C., et al. 2010, ApJ, 719, 1503
Rujopakarn, W., Eisenstein, D. J., Rieke, G. H., et al. 2010, ApJ, 718, 1171
Rupke, D. 2018, Galax, 6, 138
Rupke, D. S., Veilleux, S., & Sanders, D. B. 2005, ApJ, 632, 751
Rupke, D. S. N., Coil, A., Geach, J. E., et al. 2019, Natur, 574, 643
Rupke, D. S. N., & Veilleux, S. 2013, ApJ, 768, 75
Salim, S., Boquien, M., & Lee, J. C. 2018, ApJ, 859, 11
Salpeter, E. E. 1955, ApJ, 121, 161
Savage, B. D., & Sembach, K. R. 1991, ApJ, 379, 245
Scannapieco, E., & Brüggen, M. 2015, ApJ, 805, 158
Scarlata, C., & Panagia, N. 2015, ApJ, 801, 43
Scoville, N., Aussel, H., Brusa, M., et al. 2007, ApJS, 172, 1
Sell, P. H., Tremonti, C. A., Hickox, R. C., et al. 2014, MNRAS, 441, 3417
Shapley, A. E., Steidel, C. C., Pettini, M., et al. 2003, ApJ, 588, 65
Shen, J., & Lo, K. Y. 1995, ApJL, 445, L99
Shopbell, P. L., & Bland-Hawthorn, J. 1998, ApJ, 493, 129
Skelton, R. E., Whitaker, K. E., Momcheva, I. G., et al. 2014, ApJS, 214, 24
Somerville, R. S., & Davé, R. 2015, ARA&A, 53, 51
Soto, K. T., Martin, C. L., Prescott, M. K. M., et al. 2012, ApJ, 757, 86
Stefanon, M., Marchesini, D., Rudnick, G. H., et al. 2013, ApJ, 768, 92
Stern, D., Assef, R. J., Benford, D. J., et al. 2012, ApJ, 753, 30
Stone, J. M., Gardiner, T. A., Teuben, P., et al. 2008, ApJS, 178, 137
Strauss, M. A., Weinberg, D. H., Lupton, R. H., et al. 2002, AJ, 124, 1810
Suarez, T., Pontzen, A., Peiris, H. V., et al. 2016, MNRAS, 462, 994
Sugahara, Y., Ouchi, M., Lin, L., et al. 2017, ApJ, 850, 51
Swinbank, A. M., Smail, I., Chapman, S. C., et al. 2010, MNRAS, 405, 234
Tacconi, L. J., Neri, R., Genzel, R., et al. 2013, ApJ, 768, 74
Tanner, R., Cecil, G., & Heitsch, F. 2017, ApJ, 843, 137
Thompson, T. A., Quataert, E., Zhang, D., et al. 2016, MNRAS, 455, 1830
Tremonti, C. A., Heckman, T. M., Kauffmann, G., et al. 2004, ApJ, 613, 898
Tremonti, C. A., Moustakas, J., & Diamond-Stanic, A. M. 2007, ApJL, 663, L77
Turner, M. L., Schaye, J., Crain, R. A., et al. 2017, MNRAS, 471, 690
van der Wel, A., Franx, M., van Dokkum, P. G., et al. 2014, ApJ, 788, 28
van Dokkum, P. G., Franx, M., Kriek, M., et al. 2008, ApJL, 677, L5
van Dokkum, P. G., Nelson, E. J., Franx, M., et al. 2015, ApJ, 813, 23
Veilleux, S., Cecil, G., & Bland-Hawthorn, J. 2005, ARA&A, 43, 769
Veilleux, S., Maiolino, R., Bolatto, A. D., et al. 2020, A&ARv, 28, 2
Verhamme, A., Schaerer, D., Atek, H., et al. 2008, A&A, 491, 89
Vika, M., Bamford, S. P., Häußler, B., et al. 2013, MNRAS, 435, 623
Walter, F., Weiss, A., & Scoville, N. 2002, ApJL, 580, L21
Wang, B. 1995, ApJ, 444, 590
Weiner, B. J., Coil, A. L., Prochaska, J. X., et al. 2009, ApJ, 692, 187
Whalen, K. E., Hickox, R. C., Coil, A. L., et al. 2022, AJ, 164, 222
Wood, C. M., Tremonti, C. A., Calzetti, D., et al. 2015, MNRAS, 452, 2712
Wright, E. L., Eisenhardt, P. R. M., Mainzer, A. K., et al. 2010, AJ, 140, 1868
Xu, X., Heckman, T., Henry, A., et al. 2022, ApJ, 933, 222
York, D. G., Adelman, J., Anderson, J. E., et al. 2000, AJ, 120, 1579
Zahid, H. J., Dima, G. I., Kewley, L. J., et al. 2012, ApJ, 757, 54
Zhang, D. 2018, Galax, 6, 114
Zhang, D., Thompson, T. A., Quataert, E., et al. 2017, MNRAS, 468, 4801
Zhang, D., Thompson, T. A., Quataert, E., & Murray, N. 2015, MNRAS, 468, 4
Zhu, G. B., Comparat, J., Kneib, J.-P., et al. 2015, ApJ, 815, 48
Zirm, A. W., van der Wel, A., Franx, M., et al. 2007, ApJ, 656, 66